Towards Next Generation Heterobimetallic Complexes for Bond Activation and
Multivalent Ion Batteries

BY

Noel Joseph Leon
B.A., Northwestern University, 2013

THESIS

Submitted as partial fulfillment of the requirements
For the degree of Doctor of Philosophy in Chemistry
In the Graduate College of the
University of Illinois at Chicago, 2020.
Chicago, Illinois

Defense Committee:
        Neal Mankad, Chair and Advisor
        Jordi Cabana
        Andy Nguyen
        Donald Wink
        Chen Liao, Argonne National Laboratory

## Acknowledgments

I would like to give thanks to my advisor, Professor Neal P. Mankad, for providing the opportunity to work in a lab that encourages exploration. Without that freedom, I would not have had the chance to work on projects related to energy storage. I would also like to Dr. Cabana, Dr. Nguyen, Dr. Wink, and Dr. Liao for participating in my committee and providing helpful feedback to this thesis.

I would also like to acknowledge the fellow members of the research group. It has been a pleasure to be part of a transitioning team from the original five members to each generation after my own.  I would particularly like to acknowledge Dr. Chia-Wei Hsu for always lending a hand no matter the circumstances and for being a source of positive encouragement whenever I needed it.

In addition to the research group, I would not have had the varied research experience without the collaborators and staff with which I was fortunate enough to work. I would like to thank Dr. Dan McElheny for help with NMR spectroscopy. I would also like to thank everyone who has offered advice and help as I began to apply my skills towards battery electrolytes, including Dr. Jordi Cabana, Dr. Ka-Cheong Lau, Dr. Moncy Yang, and Dr. Kewei Liu. In particular, I would like to acknowledge Dr. Chen Liao for the opportunity to work at Argonne National Lab. I was fortunate to spend a summer doing research mentored by her. This experience provided me the chance to rejoin as a post-doctoral researcher.

I need to thank all the influential people that had extended their hand even when I did not know it was needed. Without their help and inspiration, I am not sure I would have

## Contributions of Authors

Chapter one provides an overview of transition metal chemistry's impact on chemical bond transformations and their relation to our group's work in cooperative bimetallic transformations. It also provides insight into the application of synthetic skills in multivalent ion battery research.

All work adapted and reproduced in chapters two, three, and four involve manuscripts for which N. P. Mankad has largely contributed to preparing.

Chapter two is adapted from two published manuscripts that discussed manipulations to the heterobimetallic complexes used in our group and the reactivities these changes have produced. The first manuscript discussed was Mazzacano, T. J.; Leon, N. J.; Waldhart, G. W.; Mankad, N. P. Fundamental Organometallic Chemistry under Bimetallic Influence: Driving β-Hydride Elimination and Diverting Migratory Insertion at Cu and Ni. *Dalt. Trans.* 2017, *46*, 5518–5521. DOI**:** 10.1039/C6DT04533B. Only work detailing synthesis and reactivity of (POCOP)Ni-Wp complexes, for which I am responsible, were discussed. The second manuscript discussed was Leon, N. J.; Yu, H. C.; Mazzacano, T. J.; Mankad, N. P. Pursuit of C-H Borylation Reactions with Non-Precious Heterobimetallic Catalysts: Hypothesis-Driven Variations on a Design Theme. *Synlett.* 2020, *31*, 125–132. DOI: 10.1055/s-0039-1691504. I was responsible for contributing the compounds discussed in chapter two and for compiling a draft of our group's work toward borylation chemistry with some help from H. C. Yu and T. J. Mazzacano. The final work was streamlined by N. P. Mankad.

Chapter three is reproduced from Leon, N. J.; Yu, H. C.; Mazzacano, T. J.; Mankad, N. P. Mixed Phosphine/Carbonyl Derivatives of Heterobimetallic Copper–Iron

and Copper–Tungsten Catalysts. *Polyhedron.* 2019, *157*, 116–123. Doi: 10.1016/j.poly.2018.09.062. I was co-author of this work with H. C. Yu, who was responsible for work with iron complexes. I was responsible for work with tungsten complexes.

Chapter 4 was reproduced from unpublished work, Leon, N. J.: Mankad, N. P. Detection of a ligand redistribution process for hydrocarbon-soluble Mg{Al[OC(Ph)(CF$_3$)$_2$]$_4$}$_2$: evidence of a "hidden equilibrium" in polyfluorinated alkoxyaluminate chemistry. *Inorg. Chem. Submitted.* I was responsible for all experiments and helping N. P. Mankad prepare the manuscript.

Chapter 5 was reproduced from recently submitted work, Yang, M.; Leon, N. J.; Pan, B.; Yu, Z.; Cheng, Lei; Liao, C. 5. Mechanistic Insights in Quinone-Based Zinc Batteries with Nonaqueous Electrolytes. *J. Electrochem. Submitted.* I was responsible for some experiments with Zn-DMBQ cathodes during my summer at Argonne National Lab. M. Yang, B. Pan, and C. Laio were responsible for the rest of the experiments and M. Yang and C. Liao contributed the manuscript. Z. Yu was responsible for computational work.

Chapter 6 is adapted from all the experimental procedures contained in the manuscripts mentioned above, with some unpublished reports for synthesis and characterization of isocyanide substituted [M$_{co}$] complexes.

Table of Contents

# List of Schemes

## List of Figures

## List of Tables

## Abbreviations

| | |
|---|---|
| Ar | Aryl |
| (BDI) | 2-(2,6-diisopropylphenyl)amido-4-(2,6-diisopropylimino)-2-pentene |
| Bn | Benzyl |
| nBu | n-butyl |
| *t*Bu | *tert*-butyl |
| Cat | Catecholate |
| Cat. | Catalyst |
| Cc | $Co(CO)_4$ |
| cod | Cyclooctadiene |
| Cp | Cyclopentadienyl / ($\eta^5$ -$C_5H_5$) |
| Cp* | Pentamethylcyclopentadienyl / ($\eta^5$ -$C_5Me_5$) |
| Crp | $CrCp(CO)_3$ |
| DCM | Dichloromethane |
| DMBQ | Dimethoxybenzoquinone |
| DME | Dimethoxy ethane |
| dppe | 1,2-bis(diphenylphosphino)ethane |
| E | Element |
| Et | Ethyl |
| Eq | Equivalent |
| Equiv. | Equivalent |
| FLP | Frustrated Lewis Pair |
| Fp | $Fe(\eta 5$ -$C_5H_5)(CO)_2$ |

## Abbreviations (continued)

Fp*         Fe(η 5 -C$_5$Me$_5$)(CO)$_2$

FSR         formal shortness ratio

G2          diglyme

hfip        1,1,1,3,3,3-hexafluoro-2-propoxide

hPhip       1,1,1,3,3,3-hexafluoro-2-phenyl-2-propoxide

IMes         N,N'-bis(2,4,6-trimethylphenyl)imidazole-2-ylidene

iPr         isopropyl

IPr         N,N'-bis(2,6-diisopropylphenyl)imidazol-2-ylidene

L           Ligand

M           Metal

Me          Methyl

Mc          Mn(CO)$_5$

NDI         Naphthyridine-diimine

(NHC)       N-heterocyclic Carbene

OAc         Acetate

14PAQ       poly(1,4-anthraquinone)

PAQS        pol(anthraquinonyl sulfide)

PDI         Pyridinediimine

pin         Pinacolate

Ph          Phenyl

Rp          Ru(η 5 -C$_5$H$_5$)(CO)$_2$

Rp*         Ru(η 5 -C$_5$Me$_5$)(CO)$_2$

# Abbreviations (continued)

TFSI       Trifluoromethylsulfonimide

THF       Tetrahydrofuran

TMS       Trimethylsilane

WCA       Weakly coordinating anion

Wp       $W(\eta^5\text{-}C_5H_5)(CO)_3$

Wp*       $W(\eta^5\text{-}C_5Me_5)(CO)_3$

X       Halide

6Pr       N,N'-bis(2,6-diisopropylphenyl)-3,4,5,6-tetrahydropyrimidin-2-ylidene

6Mes       N,N'-bis(2,4,6-trimethylphenyl)-3,4,5,6-tetrahydropyrimidin-2-ylidene

# Summary

Chapter one discusses the impact of transition metal chemistry on bond activation and the variety of transformations owing to progress in the field. Also discussed are the concepts of binuclear site reactivity and incorporation of base metal chemistry. Using base metals is a necessary step toward an overall greener approach but also the next step toward new bond activation and complimentary catalysis to leading single-site systems. The second half of Chapter one discusses the advantages of multivalent ion batteries as future alternatives to current lithium-ion battery technology. The utility of tunable weakly coordinating anions and redox-active organic molecules as electrolytes and cathode materials is discussed further.

Chapter two presents previous work in the Mankad group developing and using a set of (NHC)M-$M_{co}$ heterobimetallic complexes for bond activation and catalysis. Work towards modifying the established heterobimetallic motif is probed where Cu(I) systems are replaced with Ni(II), and separately, carbonyl ligands are substituted with isocyanides. We also discuss the modified complexes and their reactivity toward activating C(sp)–H, H–H, and B–H bonds. Attempts to utilize new heterobimetallic Ni/W bond reactivity towards carboxylation chemistry is reported.

Chapter three details work inspired by base metal-catalyzed photochemical C(sp$^2$)–H borylation and attempts to repeat reactivity in thermal conditions. It was determined that the inadequate acidity of $M_{co}$-H is a roadblock to thermal catalytic activity. A series of $M_{co}$-H analogs, in which a carbonyl was substituted with a phosphine, were then synthesized to attempt to circumvent previous issues with hydride acidity. The

effects of new steric and electronic properties are discussed in relation to established borylation chemistry.

Chapter four discusses electrolytes with uses toward magnesium-ion batteries. A take on manipulating the heavily reported $Mg[Al(OR^F)_4]_2$ with a phenyl group is reported and its unique ability to reveal a ligand redistribution equilibrium. The work briefly examines the electrolytes electrochemical performs and discusses more in-depth the relationships that shift the observed equilibrium.

Chapter five continues the theme of energy storage in a more applied fashion. Redox-active organic materials are compared for use in zinc-ion batteries. Performance between monomer and polymer cathode systems are discussed further.

Finally, the experimental procedures for Chapters two through five are presented in Chapter six.

## 1.  Introduction

### 1.1    Introduction to transition metal-mediated bond activation

Paraffin was first isolated from wood tar by Karl von Reichenbach as a waxy substance in 1830. The word is derived from Latin *parum* and *affinis*, or "too little" and "associated with." In other words, paraffin, or alkanes, are chemically unrelated to other substances and are relatively inert[1]. As a result, there are few direct methods for the conversion of these simple chemical feedstocks, like petroleum, to more valuable products. Alkyl C–H and C–C bond cleavage has been inadvertently used throughout human history. Under harsh conditions, like high temperatures of an engine, alkanes do combust. The resulting energy has been harnessed in standard four-stroke internal combustion engines since development in the late 1800s by Otto, Daimler, and Maybach[2]. While internal combustion engines make use of bond activation in alkanes, they do so in a chemically uncontrollable manner with products of which are less useful for upcycling or conversion.[3] Chemists seek to synthesize useful products, controllably, by way of activating those bonds.

Since its origin and revival in the 1950s, transition metal chemistry has involved the binding of substrates to a metal center, allowing for subtle changes to occur in the molecular orbital energies of a variety of substrates. In this manner, the metal centers are allowed to participate in activation of otherwise less reactive C–H, C–C, and C–X bonds for further reactivity and catalysis.

Using transition metal complexes as a method for bond breaking and bond formation in homogeneous catalysis has heavily impacted fine chemical production and

pharmaceutical synthesis.[4–6] Constructing carbon-carbon bonds by pairing nucleophiles with electrophiles and the transformation of functional groups attached to a carbon scaffold has been an overarching theme in traditional organic synthesis. The emergence of catalytic cross-coupling reactions, mainly through Pd complexes[7], is an excellent example through which transition metal reactivity has brought variety to pathways of bond formation and new products. Catalysis has followed the theme in developing a variety of reactions pairing an organometallic nucleophile with an electrophilic organohalide or pseudohalide. The field of cross-coupling has expanded to include organolithium, magnesium, zinc, silicon, boron, and alkene substrates (Scheme 1-1)[8].

$$R^1{-}R^2$$

$$R^1$$

$$R^2$$

a | $R^2{-}B(OR)_2$

$$R^1{-}R^2$$

f

b

$$R^2$$

$$R^2{-}SnR_3$$

$$R^1{-}X$$

+

cat. [Pd]

$$R^2{-}SiR_3$$

$$R^2{-}ZnR$$

e

c

d | $R^2{-}MgX$

$$R^1{-}R^2$$

$$R^1{-}R^2$$

$$R^1{-}R^2$$
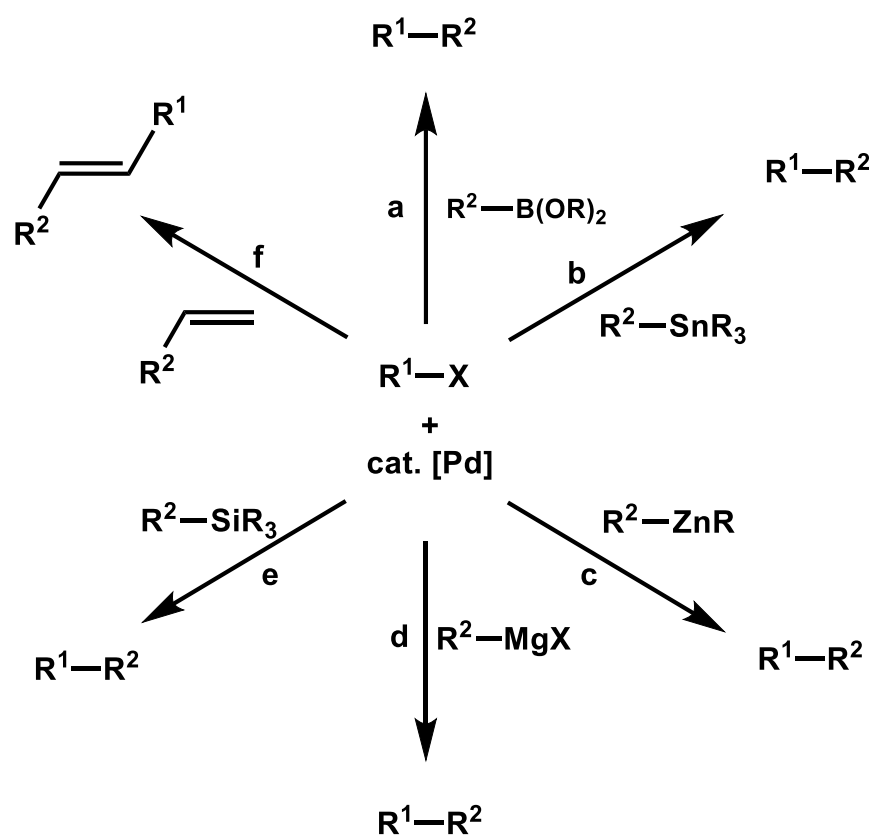
**Scheme 1-1.** Scope of organometallic reagents used in Pd-catalyzed cross-coupling reactions. (a) Suzuki-Miyaura reaction, (b) Stille reaction, (c) Negishi reaction, (d) Kumada reaction, (e) Hiyama reaction (f) Heck reaction.

Cross-coupling reactions are not limited to the formation of new C–C bonds. Synthesis of heteroatomic products, through C–N bond formation, is a prime example of transition metal chemistry that provides a new pathway for bond formation while reducing the number of synthetic steps. Traditional methods of benzene amination could call for multistep syntheses by way of harsh combinations of nitric and sulfuric acid to install a nitrate group followed by reduction under acidic conditions with tin or iron. At which point, aniline derivatives could be functionalized in a variety of ways by alkylation to produce secondary or tertiary amines (Scheme 1-2). Cross-coupling methods have helped mitigate harsh reaction conditions and provide more direct functionalization in one step while avoiding byproducts from multiple functionalizations.

In the 1990s, Buchwald and Hartwig were credited with having made the first strides toward aromatic amination through Pd-catalyzed C-N coupling of aryl halides and secondary amines (Scheme 1-2).[9]. These discoveries provided new options for single-step functionalization at lower reaction temperatures when using starting materials containing C–X bonds.
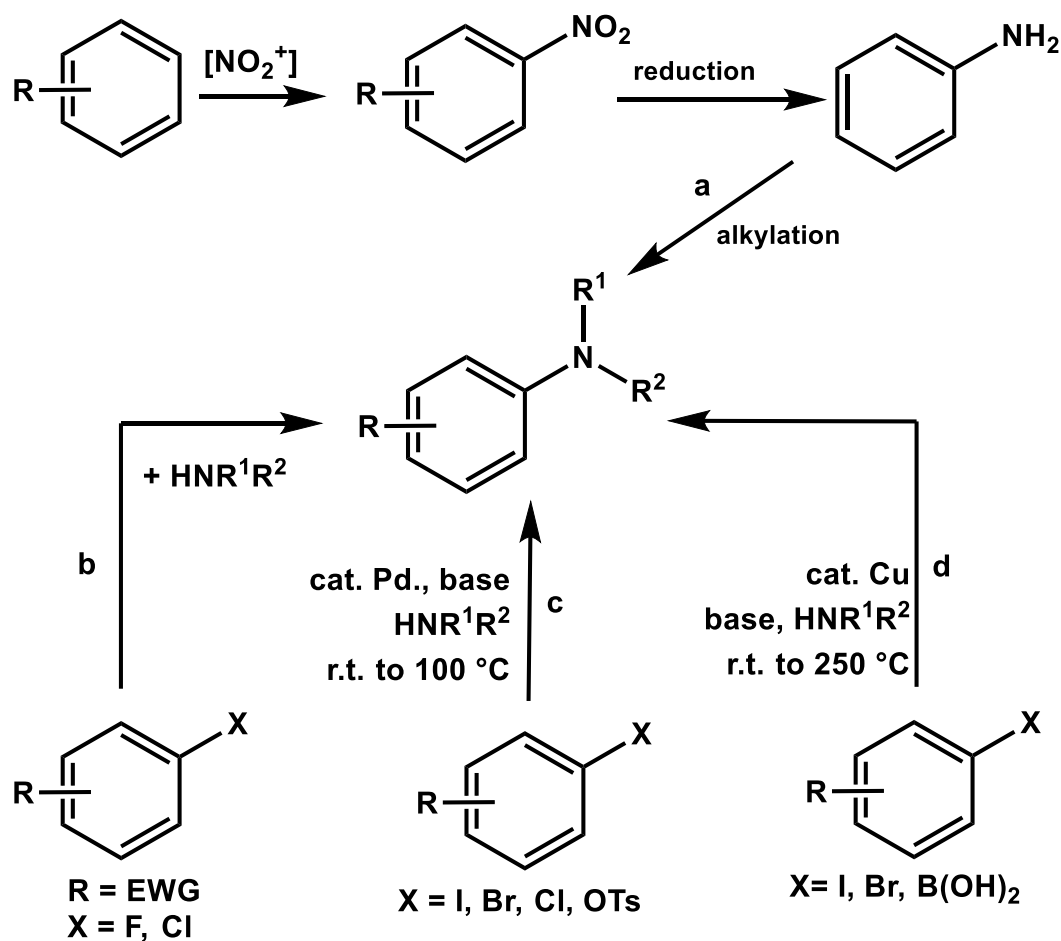
**Scheme 1-2.** Comparison of (a) multistep process, (b) nucleophilic substitution, (c) Buchwald-Hartwig amination, and (d) Cu-mediated cross-coupling

Transition metal chemistry has become an integral part of syntheses for pharmaceutical, material, catalysis, coordination, natural product, and biological chemistry.[7,10]

## 1.2    Introduction to base metal bimetallic reactivity

Across disciplines, the necessity to move technology toward environmentally less harmful and cheaper alternatives has become more evident than ever. Base-metals are

more abundant, and therefore cheaper to manufacture than their precious metal counterparts. Base metals like Cu, Ni, and Fe are found between 50-41000 ppm in the earth's crust with production values of 18.7 megatons to 3.3 gigatons in 2015. Precious metal counterparts like Pd, Pt, and Rh are found from 0.001-0.0002 ppm in the earth's crust, and their production values follow with 30-208 tons.[11] Current prices of precatalyst chemicals from Sigma Aldrich reflect their abundance and production with $Ni(OAc)_2 \cdot 4(H_2O)$ ($ 0.07/ mmol) compared to a similar precatalyst in $Pd(OAc)_2$ ($ 23.57/ mmol).

Developing systems that use more cost-effective metal catalysts can significantly affect the pharmaceutical industry. For example, a scalable method was developed using late-stage Pd-catalyzed kilogram synthesis of a potent endothelin receptor antagonist toward treatments for pulmonary hypertension and heart failure. This method displays functional group tolerance in joining the "northern half" as an arylboronic acid with a highly functionalized triflate, "southern half" (Scheme 1-3).[12] Pd catalysis is often highly efficient, with catalyst loadings under one percent at times. The price disparity between Pd and Ni precatalysts effectively demonstrates the cost-effectiveness of being able to run the previous reaction example using a Ni catalyst at 100 kg scale. New methods in cross-coupling and bond activation have been developed to further lower costs using microwave or ultrasonic energy[13,14] and Ni-catalyzed methods that give alternatives, or even compliment, Pd methods available.[15–17]
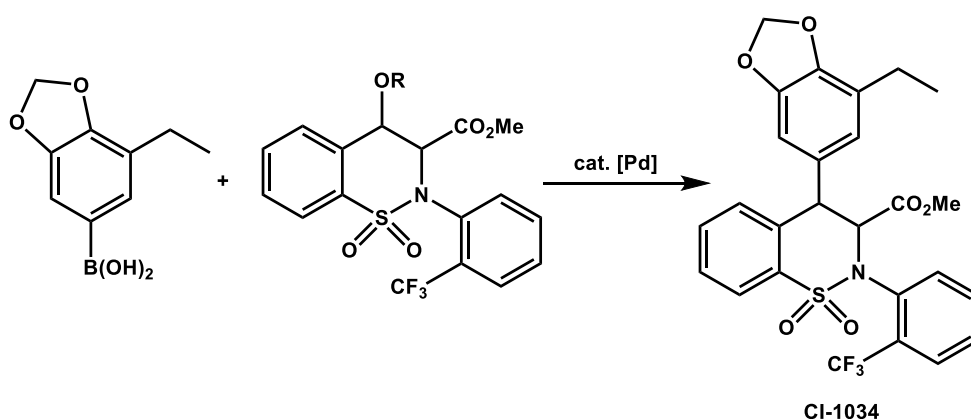
**Scheme 1-3.** Scalable process using Suzuki-Miyaura reaction to synthesize CI-1034.

Earth-abundant metals are often considered environmentally and biologically more compatible, which means they need less stringent efforts for purification in pharmaceuticals.[18] Elements like Cu, Fe, and Ni are essential trace nutrients for plants and animals, participating in biological activity.[19] It can be seen that manufacturing more abundant metal resources is not only cheaper but can be less detrimental when leached to the surrounding environment. Bioavailability of metals depends highly on oxidation state, coordination environment, and solubility of the metal complex in question. Recent literature has highlighted and further complicated the argument regarding precious metal toxicity as some forms of metals like Pd (575 mg/kg) can be lower in toxicity compared to Ni (500 mg/kg) in the context of traditional oral toxicity for rats.[11,20] It must be noted that regardless of traditional oral toxicities, precious metals are still harmful as pollutants from automotive catalytic converters or when leached into the environment. Research has linked precious metal pollution with respiratory issues as allergens and with accumulation in organs, showing evidence of mitochondrial and DNA degradation.[11,21]

Palladium-catalyzed cross-coupling reactions as a specific case for transition metal catalysis shows the movement toward using more sustainable elements for catalysis as Ni-catalyzed cross-coupling reactions become more frequent in literature.

In addition to movement towards abundant metal cat, we want to use new methods of bond activation to expand the library of substrates for new bond formation and chemical feedstocks.

The use of transition metal catalysis in organic synthesis had previously focused on the use of precious metals and single-site reactivity for bond activation.[7] Cross-coupling chemistry has been the exemplary field for displaying single-site reactivity and selectivity by control of a variety of ligands, like phosphines, coordinated to a single metal center, like Pd.[22] Critical to this system is the activation of organohalide, or pseudohalide reagents, and reductive bond formation steps managed by a single metal center (Scheme 1-4a). Conversely, many earth-abundant metal systems of the past lacked the ability to use these distinct reactivities.

As a result, new methods of mediating bond activation have been developed by sharing reactivity beyond a metal center. (Scheme1-4 b-d).[23,24] Research beyond single-site reactivity has permitted new pathways to bond activation/formation, further adding to the synthetic chemists' toolbox, while providing more examples of cost-effective earth-abundant catalysts. Delocalization of bond reactivity has brought about non-metal frustrated Lewis pairs[25], redox non-innocent ligand-metal interaction[26], and metal-metal cooperativity.[27]
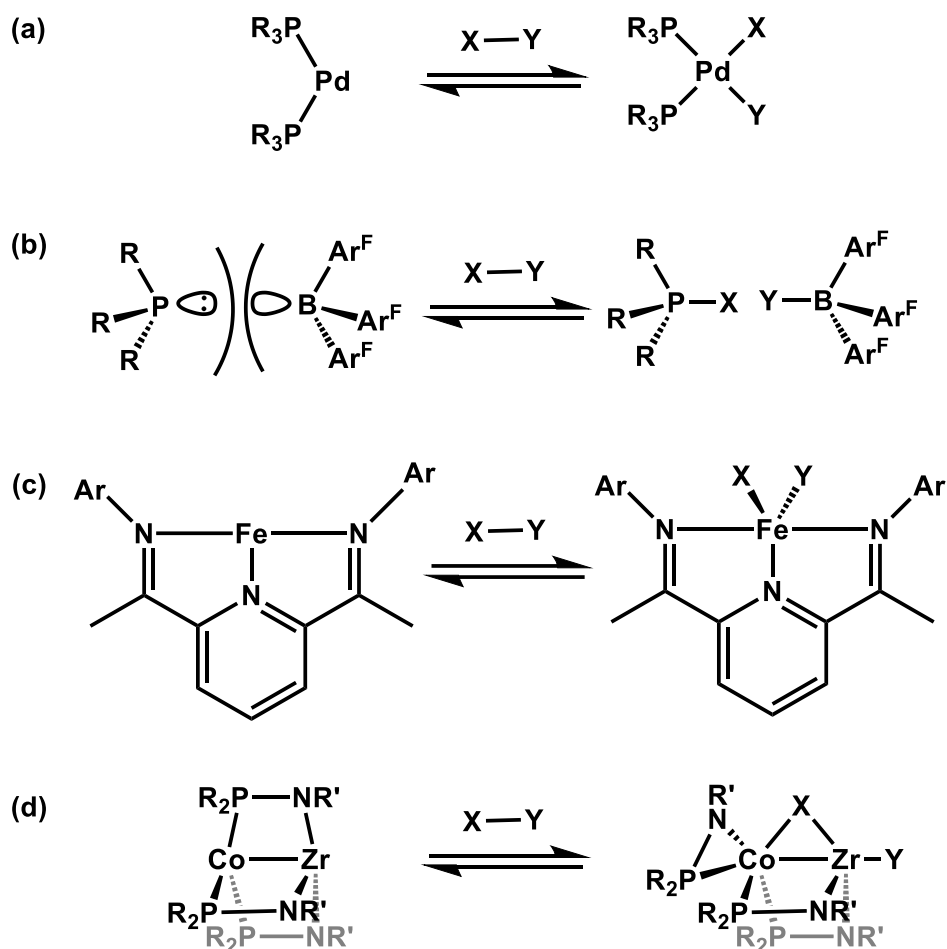
**Scheme 1-4.** Bond activation with (a) single-site and (b)-(d) delocalized reactivity.

## 1.2.1 Frustrated Lewis Pairs

The Stephan group pioneered the area of frustrated Lewis Pair (FLP) chemistry as a metal-free approach to bond activation. Using highly polar Lewis acid-base pairs, they achieved reversible activation of $H_2$ in 2006.[28] They used a unique compound containing both Lewis acid and base functionalities bound rigidly in a manner that the two entities are not in proximity to self-quench, hence "frustrated." FLPs have been observed to react in a heterolytic fashion through an "encounter complex" created by association of the pair or as a "frustrated radical pair" involving single-electron transfer from base to acid. The latter reactivity can be seen when using FLPs derived from $PMes_3$ and $B(C_6F_5)_3$ reacting

with Ph₃SnH.[29,30] (Figure 1-1) The concept has become a field of its own with broad applications in hydrogenation, small molecule activation, and polymerizations.[25]
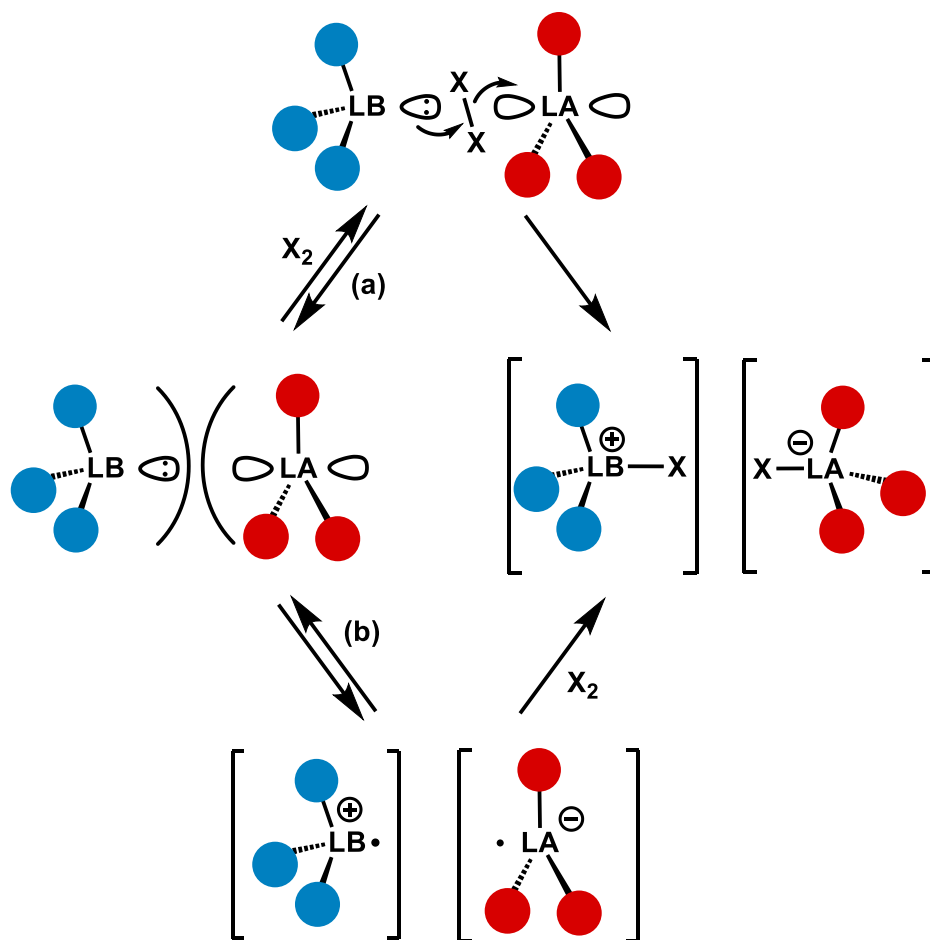


**Figure 1-1**. (a) heterolytic and (b) homolytic substrate activation with FLPs.

### 1.2.2 Non-innocent ligand-metal interaction

Another method of imitating two-electron redox properties of precious metals is to design base metal single-site complexes involving redox-active, or non-innocent, ligand structures. Organometallic complexes are often influenced by steric and electronic properties of ligands surrounding a single metal center, where the bond breaking and forming occur.[31–33] Using non-innocent redox-active ligands affords the opportunity for

delocalization or electron transfer to occur at the ligand, where normally redox-inactive ligands are not readily oxidized or reduced.[34,35]

Designing catalysts involving redox-active ligands makes it possible to use single-site base metals like Fe(II), often preferring one-electron redox activity. When supported by pincer ligands that share the burden of redox activity, these complexes undergo two-electron activity.[36] Pincer ligands have found a variety of uses for their ability to reversibly aromatize and store extra electrons. The iron systems studied by Chirik highlight this chemistry in cycloaddition reactions.[37,38] They reported the use of 2,6-diiminepyridine ligand (PDI, Ar = 2,6-diisopropylphenyl) bound to a bis-dinitrogen complex (L = $N_2$) as electron storage in a [2+2]-cycloaddition reaction. The use of PDI allows the electronically favorable Fe(II) to avoid the less energetically favorable Fe(IV) during oxidative addition and unstable Fe(0) during reductive elimination (Scheme 1-5).
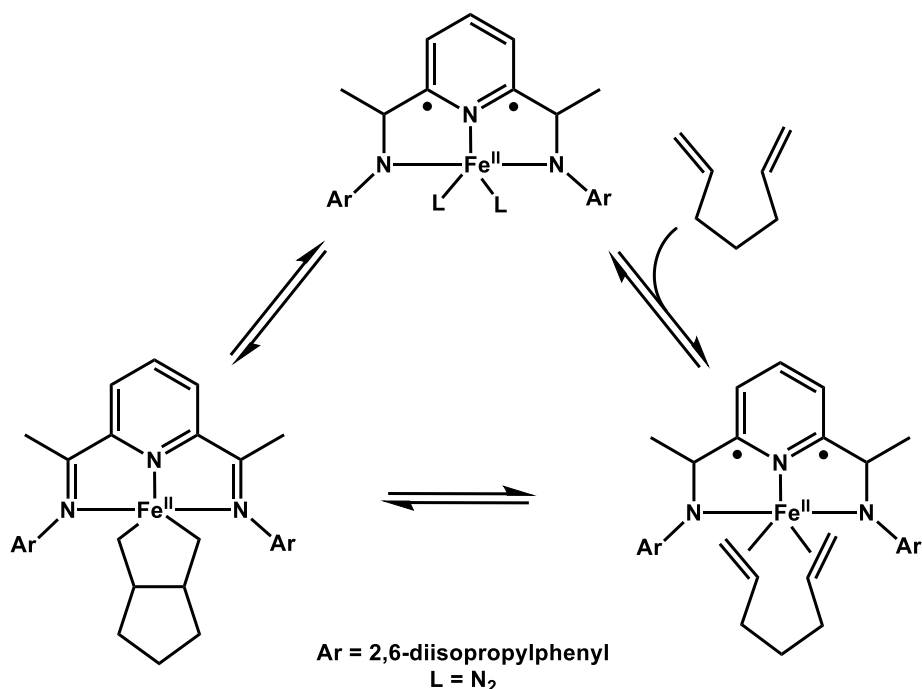


**Scheme 1-5.** Redox non-innocent 2,6-diiminepyridine electron storage in Fe(II)-catalyzed [2+2]-cycloaddition.

### 1.2.3  Metal-metal cooperativity

Another method of distribution of reactivity over multiple sites can be seen in metal-metal cooperativity, where bond activation can be shared across two metal complexes. Bimetallic reactivity can occur synergistically, in which two unbound metals undergo reactivity separately, or it can occur cooperatively, where metal-metal bonds are made and broken during bond activation. Our group has developed methods using both, but this text will mainly detail cooperative binuclear reactivity in bond activation and catalytic applications.

The critical feature for metal-metal cooperative reactivity is the pre-installed bimetallic bond or close association of the reactive organometallic complex. In this fashion, bimetallic complexes can be seen sharing the work in bond activation. Homobimetallic bond activation has been observed for some time, with examples dating back 50 years.[39–42] Recent work with bimetallic catalysts follows the general scheme of bimetallic oxidative addition, substrate transformation, and bimetallic reductive elimination. Homobimetallic systems involving Pd[43], Au[44], and Ni[45,46] have been developed using bridging ligands that create the proximately necessary for shared reaction (Figure 1-2).
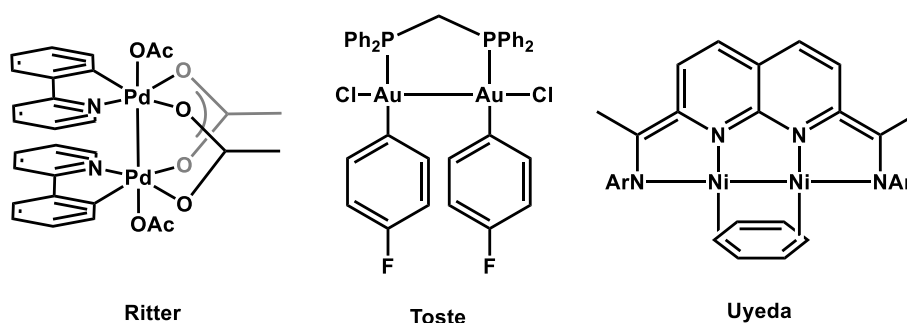
**Figure 1-2.** Various homobimetallic systems employing bridging ligands reported by Ritter, Toste, and Uyeda.

One such example in homobimetallic catalysis developed in the Uyeda group has shown hydrosilation, cyclotrimerization, and carbonylation capability based on a rigid napthyridine-diimine (NDI) ligand that providing steric and redox-active stability to the dinickel metal centers.[47] This system employs a labile benzene ligand that can reversibly occupy the Ni(II)-Ni(II) coordination environment, and binuclear substrate binding products have been isolated to confirm cooperative participation (Scheme 1-6). In this case, the Ni-Ni bond is unchanged throughout. It is hypothesized that the use of redox-active diamine ligand provides extra delocalization. As a result, the Ni-Ni bond stays intact while cooperatively participating in bond activation of organosilanes in catalytic silylation of C=C and C=O multiple bonds.[45]
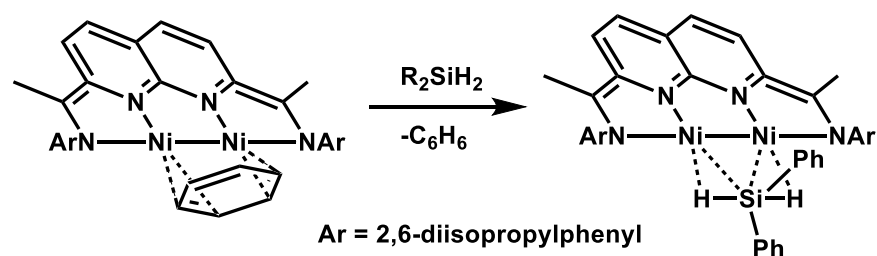


Scheme 1-6. Organosilane binding to Uyeda-style dinickel complex.

### 1.2.4 Heterobimetallic reactivity

Many examples of homobimetallic complexes have been observed to participate in bond activation and redox activity across both sites. These systems are often highly covalent in metal-metal bonding. Heterobimetallic systems have also been developed using pre-installed bound/associated binuclear complexes, exhibiting a less covalent interaction. Similar to the frustrated Lewis pair, heterobimetallic complexes harness bifunctional reactivity across a polar metal-metal interaction. A great example of Lewis acid and base reactive approach is the work done by Coates and coworkers.[48] A heterobimetallic ion pair ($[LCr(THF)_2]^+[Co(CO)_4]^-$, where L = octaethylporphyrinate) was shown to catalyze formation of β-lactones from epoxides. Both metals are proposed to participate in ring-opening and closing steps, whereas only cobalt is involved in carbonylation (Scheme 1-7)
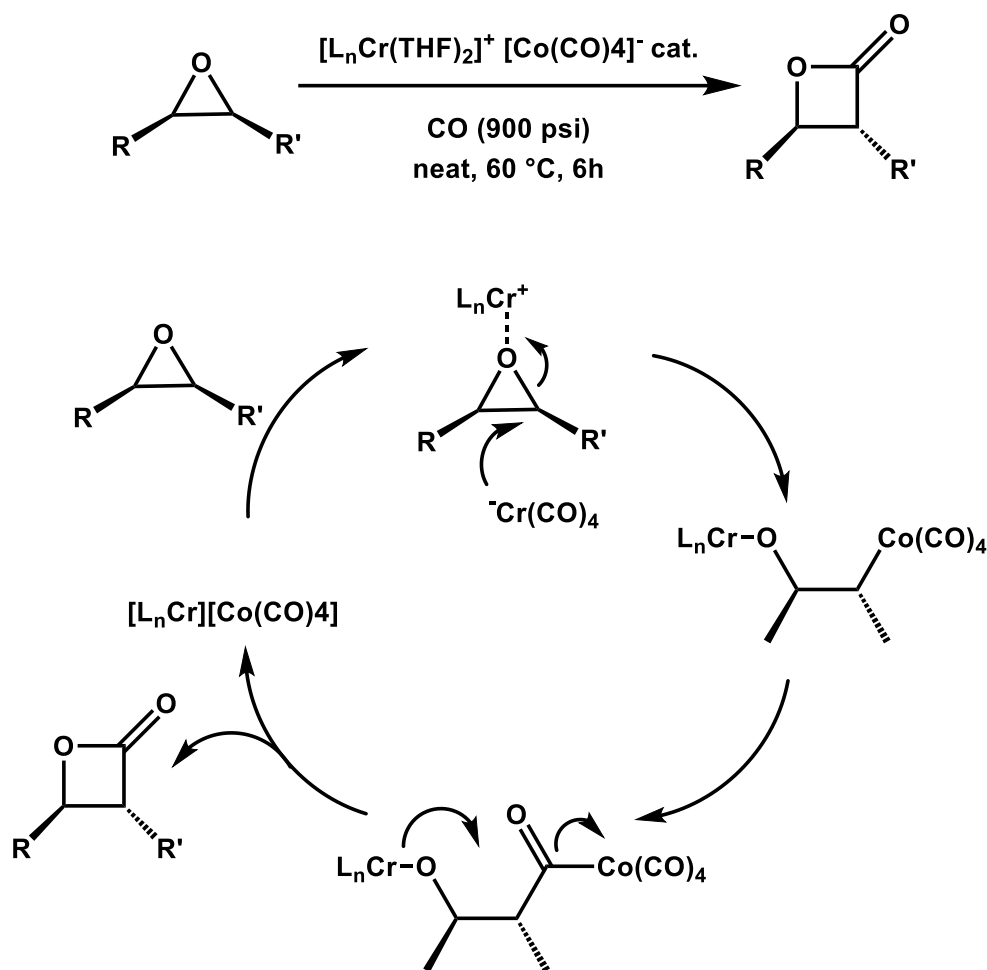
**Scheme 1-7.** Proposed mechanism of epoxide carbonylation by [LnCr(THF)2][Co(CO)4] ( L = octaethylporphyrinate).

Other heterobimetallic systems display persistent interaction between tethered metal centers. In an example reported by Nagashima, Pd-catalyzed C–N coupling was observed to be more efficient than the monometallic counterparts. The dative Pd–Ti association was proposed to stabilize a Pd(0) transition state and enhance electrophilicity of coordinated allyl moieties to allow more facile reductive elimination of the allylic amine (Scheme 1-8).[49,50]
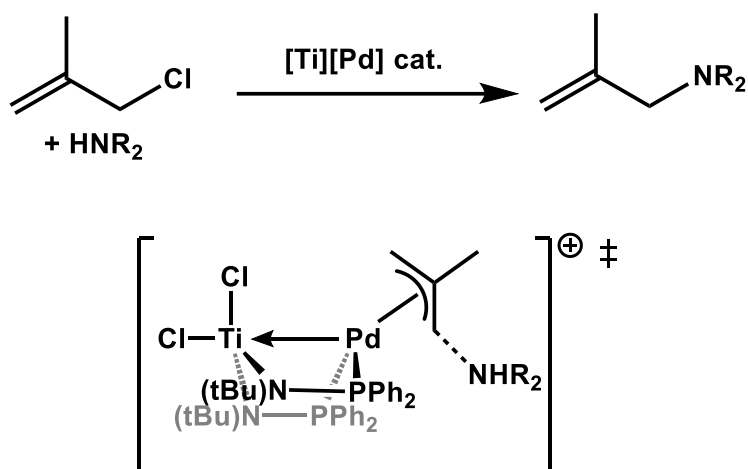
Scheme 1-8. Ti/Pd catalyzed allylic amination

The Lu group reported Ni-Ga heterobimetallic complexes with a metal-metal bond ligated by a rigid scorpionate-like structure encompassing both metal centers. The gallium center has a trigonal bipyramidal coordination sphere with Ni bound in the axial position. Nickel shares similar coordination, leaving one open coordination site at the terminal axial position. This elaborate structure displays dihydrogen coordination at the open Ni site and hydride transfer in the presence of $CO_2$ to form the formate (Scheme 1-9). This unique system retains the dative Ni-Ga bond throughout with reactivity occurring only at the Ni center.[51]
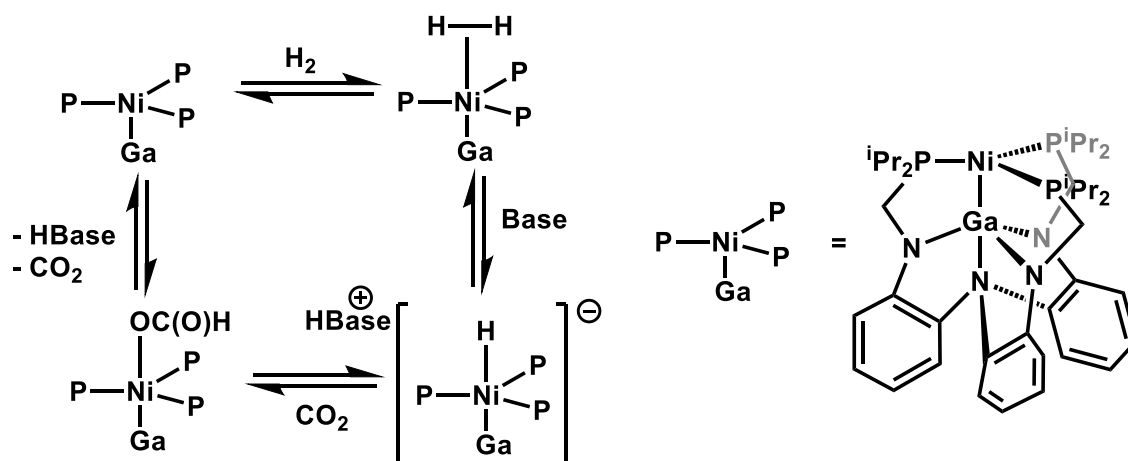
Scheme 1-9. Bimetallic Nickel–Gallium hydrogenation of CO2

## 1.2.5 Cooperative heterobimetallic transformations with the Mankad motif

The Mankad group has produced a variety of heterobimetallic transformations, including hydrogenation and borylation reactions. In these systems, preassembled binuclear complexes are constructed by salt metathesis, providing two closely associated metals tethered only by a polar metal–metal bond.[52] Unlike other systems with rigid ligand structures, the Mankad variety involves metal-metal bond breakage and formation in reversible activation of dihydrogen or boranes. The general design pairs a Lewis acidic [(NHC)Cu]$^+$ (or [(NHC)Ag]$^+$) fragment with a Lewis basic [$M_{co}$]- fragment (NHC = N-heterocyclic carbene; [$M_{co}$] = metal carbonyl complex).

A fine example of this system's analogy to FLP chemistry is the catalytic semi-hydrogenation of alkynes. Like FLP hydrogenation reactions, the [$M_{co}$]$^-$ fragment serves the purpose of proton delivery, and (NHC)AgH analogs are seen to insert alkynes readily.[53,54] The most unique finding from this system is the unusual selective formation

16

of *E*-alkenes (Scheme 1-10).[55] In this system, it was found that both metal complexes must be present for H$_2$ activation and alkene elimination.[56]
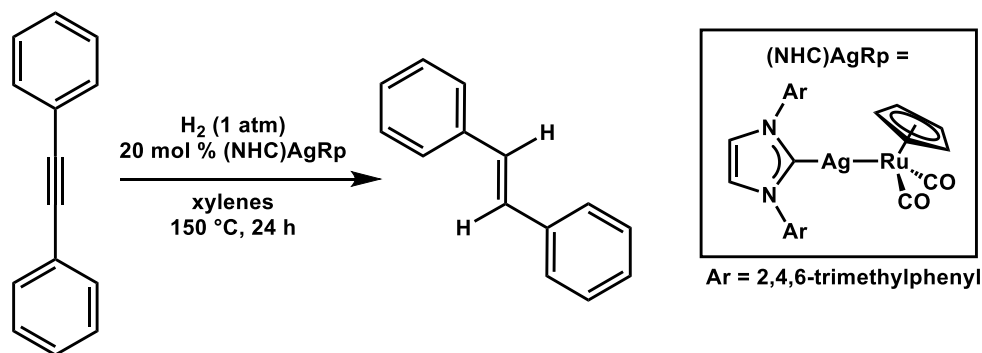


**Scheme 1-10.** Cooperative bimetallic *E*-selective hydrogenation of alkynes.

The focus of this introduction thus far has praised the work toward transition metal-mediated bond activation, with a particular interest in cooperative binuclear reactivity. With the influence that borylation chemistry and utility of their products have had in synthetic chemistry, it is imperative that we mention the first application to catalysis presented by the Mankad motif. Mazzacano and coworkers first presented the photochemical dehydrogenative borylation of C(sp$^2$)–H bonds (Scheme 1-11).[57]
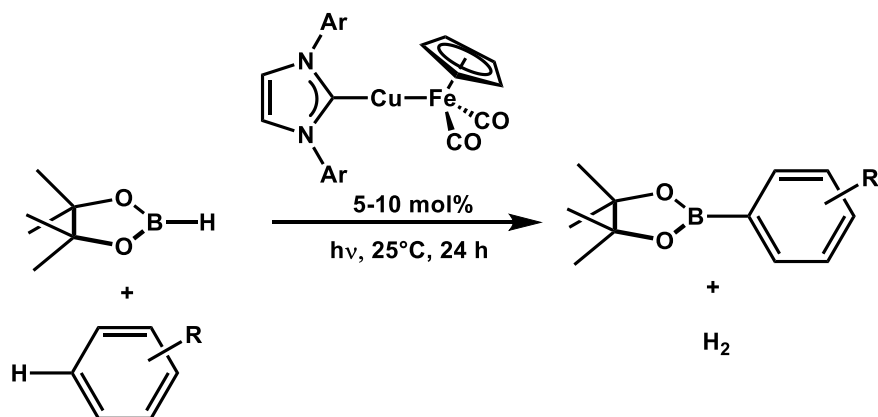
**Scheme 1-11.** Cooperative bimetallic dehydrogenative $C(sp^2)$–H borylation.

The Hartwig group established a group of $[M_{Co}]B(OR)_2$ complexes known to undergo photochemical borylation of $C(sp^2)$–H and $C(sp^3)$–H bonds.[58–60] The Mankad group paired this chemistry with that of the aforementioned (NHC)CuH system to cooperatively activate B-H bonds and create the photochemically active $[M_{Co}]B(OR)_2$. After formation of the borylated product, they were able to use (NHC)CuH to trap the resulting $[M_{Co}]H$ and reductively eliminate $H_2$ to form the bimetallic catalyst. At the time, this system was the first non-precious metal catalyst for direct C-H bond borylation.

### 1.2.6 Conclusion

To date, the field of heterobimetallic chemistry, among other methods of delocalized reactivity, has diversified methods for synthesis that complement the standard methods of single-site catalysis.  The concept of heterobimetallic chemistry has provided new platforms for rational design of new bond activation and catalysis. This introduction has provided some examples of the impact that homogeneous catalysis has had on synthetic chemistry and the utility of introducing new methods beyond single-site catalysis. The Mankad motif has utilized the general (NHC)M-[$M_{Co}$]

design and has been able to show new examples of bond activation applied in catalysis while showing some cases with earth-abundant metals.

Previously studied catalysts in this motif suffered from high catalytic loading and/or harsh reaction conditions, including high temperatures or ultraviolet light conditions. The advantage of the current system is the variety of options for tunability in the general (NHC)M-[$M_{CO}$] scheme. Various NHC ligands lend different options for steric hindrance at the electrophilic metal center, and nucleophilicity can be tuned with the choice of metal in the metal carbonyl fragment.

There remains an immense potential for further modulation beyond [(NHC)M]$^+$ fragments with more electrophilic nature, and with it new bond activation or increased reactivity. On the other hand, there is work to be done fine-tuning current catalytic systems for more favorable reaction conditions. A goal of the Mankad group is to modify the nucleophilic fragment with more labile alternatives to carbonyl ligands. Doing so could help convert catalytic photochemical borylation to thermal conditions. Attempts towards modifications of the electrophilic and nucleophilic fragments in the Mankad motif will be detailed in the first half of this thesis, and their effects on reactivity were studied in detail. These experiments are crucial toward further exploration of the heterobimetallic motif by providing new methods for synthesizing novel bimetallic complexes. Understanding their impact on future rational heterobimetallic design will give the tools to inform developments for targeted catalysis.

## 1.3 Forays into multivalent ion batteries: application of synthetic tunability

In transition metal-mediated transformations, chemists often seek to develop a highly reactive complex while remaining controllable and tolerant of functional groups. Conversely, organometallic compounds have found applications beyond bond transformation as advantageously tunable species with targeted characteristics of robustness and non-reactivity as battery components. As chemistry becomes increasingly more interdisciplinary, battery chemists have summoned skills of synthetic chemists as collaborators to create new battery components.[61] The second half of this introduction will detail the influence of tunable synthetic chemistry on the synthesis and application of weakly coordinating anions (WCAs) and redox-active organic species in electrolytes and as cathode materials.

### 1.3.1 Energy storage

With the continued rise in the global population comes the increased use and demand for energy. Society has become more aware of its impact on the environment, spurring the development of new technologies for electric vehicles and renewable energy sources. Electric transportation has made leaps in the efficiency of energy transfer of up to 80% of battery power being converted to movement at the wheels. Internal combustion engines in cars only transfer about 20% of energy toward movement at the wheels. Still, they remain superior for the travel range capabilities afforded by the high energy density of gasoline.[62] Renewable energy sources, on the other hand, face issues with intermittency and the need for storage when overproduction of energy occurs during low times of use.[63] The 2019 Nobel prize-winning chemistry of lithium-ion batteries is the

leading technology for energy storage and delivery but are projected to plateau in the near future.[64]

Current lithium-ion energy storage technology operates on the principles of $Li^+$ transportation to compensate for electron storage and expenditure. Metal ion batteries are generally made of a cathode, anode, and a separator material to keep the two ends from coming in physical contact. Lithium-ion batteries charge by the migration of lithium ions ($Li^+$) and electrons from the positive cathode, often lithium cobalt oxide, to the negative anode, where it is intercalated in graphite as $Li^0$. $LiPF_6$ or $Li(TFSI)$ (TFSI = trifluorosulfonimide) are used to provide effortless movement of ions between electrodes. The reverse process happens during discharge with ions ideally in free movement through conductive electrolytes (Figure 1-3).[65]
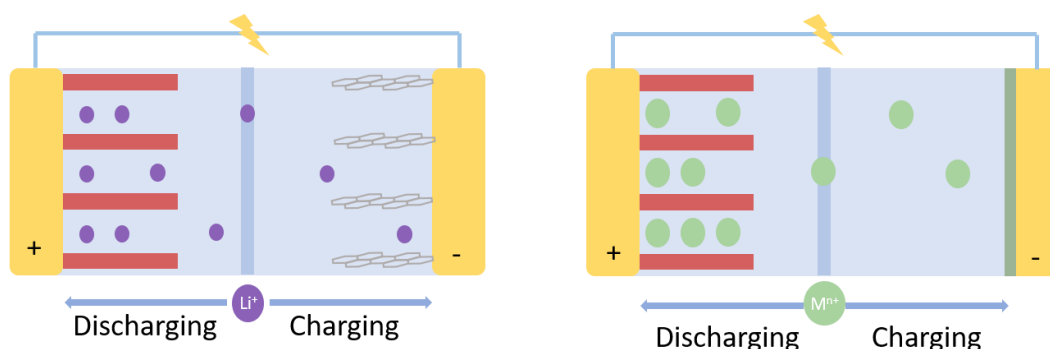


**Figure 1-3.** General battery operation comparing lithium-ion batteries (left) and multivalent ion batteries (right).

### 1.3.2 Multivalent ion batteries

Research in multivalent ion battery electrolytes and cathodes have surged recently with Al, Mg, Ca, and Zn ion batteries. Mg, Ca, and Al are more earth-abundant

and cost-effective elements than Li. Unlike lithium-ion technology, these metals are much less hazardous to moist atmospheric conditions and do not readily form dendrites, which can rupture battery separator material.[65] These properties make it possible to avoid the use of graphite as a negative electrode for storing $M^0$ atoms by using electrodeposition and dissolution chemistry of $M^{n+}/M^0$ atoms (Figure 1-3). Electrolyte solubility and the extent of ion-pairing are fundamental properties as the shuttling of multivalent cations need to be free of contact ion pairs for ease of deposition and dissolution.[66] As a result, $PF_6^-$ and $TFSI^-$ anions are less useful with multivalent counterions. The higher the concentration of active cation in solution lends to more available species for plating and deposition. Also, the use of a solid metal anode allows for more active electron carriers to be contained in a smaller package, which makes multivalent ion battery technology attractive for their high theoretic energy densities being at least double that of lithium.[67]

Previously, binuclear site reactivity was discussed for its unique ability to delocalize reactivity across multiple entities. Inversely, metal ion batteries function by shuttle electrons, and all other species for ion storage and movement are required to participate innocently. Further review of new electrolyte systems as they relate to magnesium-ion batteries and cathode systems for zinc-ion batteries will follow in the coming chapters. Understanding e

### 1.3.3 Weakly coordinating anions

Weakly coordinating ions are employed for their ability to delocalize a negative charge over the entire robust structure. Ideally, this is done over a large area without sites of nucleophilicity to minimize ion-pairing interactions and degradation. Rather than developing new methods for catalysis or bond activation, WCAs have been particularly

useful in improving highly active catalysts. Asymmetric hydrogenation of olefins with Ir(I) cationic complexes are heavily dependent on the counter anion. Reaction rates were determined to decrease with the size of the anion (Figure 1-4).[68]
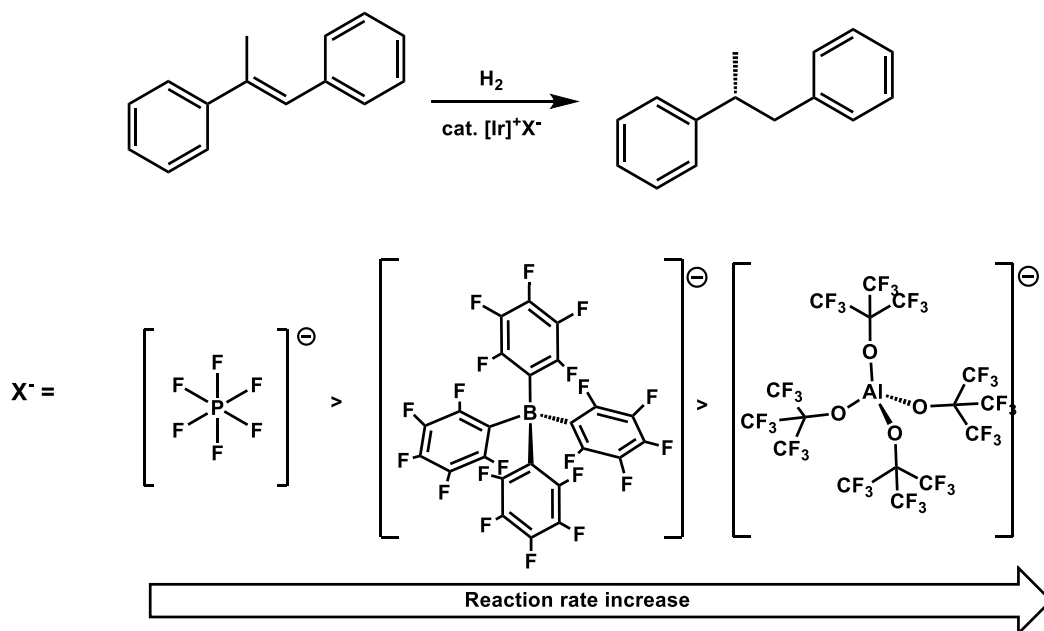


**Figure 1-4.** Influence of WCA on Ir-catalyzed asymmetric hydrogenation.

Trifluoromethylsulfonyl type WCAs are a well-known example because they possess characteristics of being unreactive, poorly nucleophilic, and highly soluble with the ability to delocalize negative charge through resonance (Figure 1-5a).[66] The presence of nitrogen or oxygen donors can make these anions poor candidates for applications with hard counterparts, like alkali metals.[69] Ideal attributes of a weakly coordinating anion can be tuned around the concepts of coordination ability, electrophilic stability, and oxidation stability.
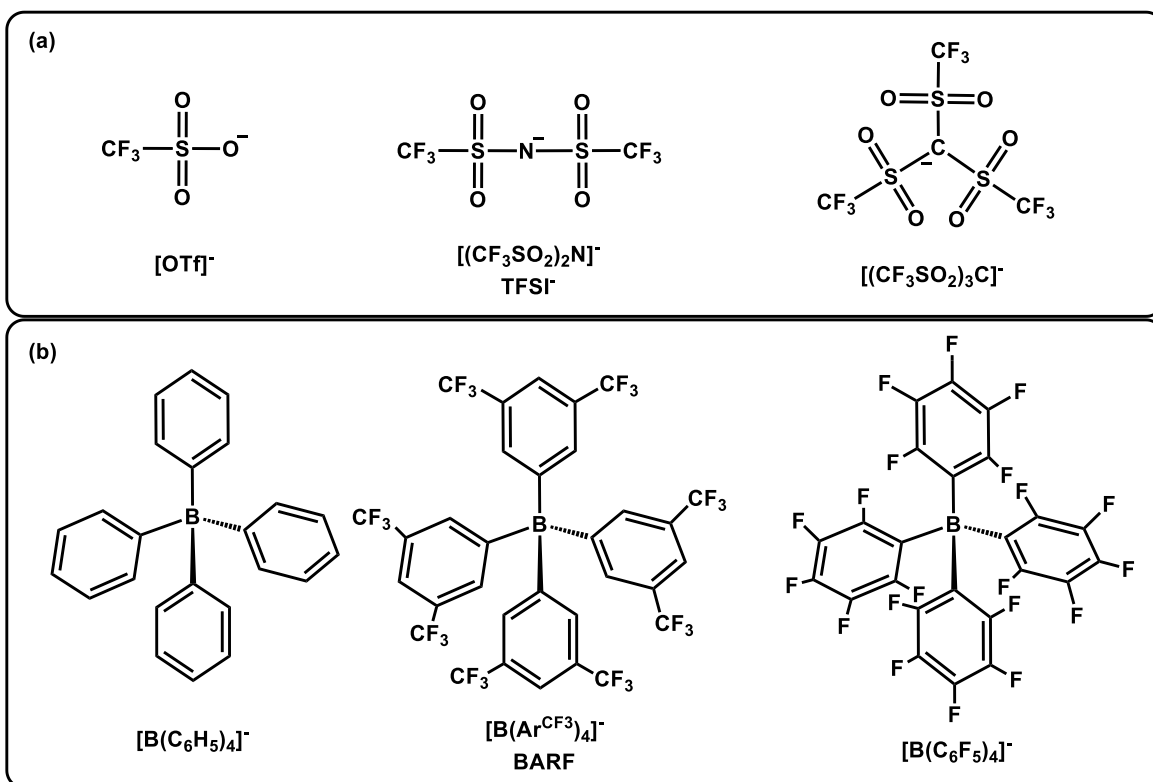
**Figure 1-5.** (a) trifluoromethylsulfonyl based and (b) tetraarylborate weakly coordinating anions.

Ubiquitous in literature is the tetraarylborate and its halogenated analogs that use aromaticity to delocalize charge (Figure 1-5b).[66,70,71] Partially or fully halogenating the aryl functional groups helps mitigate coordination complexes that may arise with arene association to cations. Additionally, halogenation has expanded solubility properties to various hydrocarbon solvents and fluorous solvents, which has allowed recyclable cationic metal catalysis in biphasic systems.[72]

In the 1960s, alkali metal salts of a particular type were reported to pass through organisms with the toxicity of sodium chloride, exhibiting excellent stability. This compound was found to be a candidate for use as weakly coordinating anion. The exotic carborane anion was advertised as the "least coordinating anion" in 1986.[73] Despite

lacking lone pairs or π systems, polyhedral (car)boranes display delocalization across the cluster through σ-bonds in an aromatic-like fashion (Figure 1-6).[74] These uniquely bulky and stable molecules have found extensive interdisciplinary use as ligands in metal complexes,[75] boron neutron capture therapy for cancer,[76] and in cross-linked polymers.[77] As WCAs, carboranes can be modified to increase solubilities by methylation with the caveat of increased reactivity. On the other hand, a compromise between solubility and stability is evident as halogenation of the carborane increases inertness and reduces coordination ability while reducing solubility.[66]



$CB_{11}H_{11}{}^{-}$
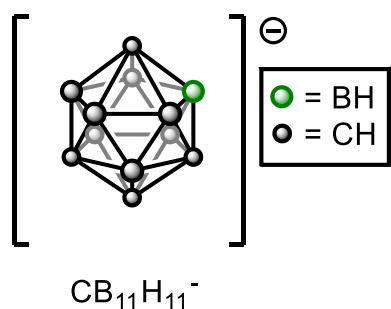
**Figure 1-6.** Monocarba-closo-dodecaborate anion

The final WCA of note, and particularly relevant to this text, is the tetracoordinate aluminate anion, which contains four alkoxide ligands surrounding a central Al(III) metal center. As early as the 1980s, $[P_9]^+$ was the first polyatomic phosphorous cation reported in the condensed phase by mass spectrometry.[78] It was finally observed to be stabilized by an alkoxyaluminate ($[Al(OR^F)_4]^-$; $OR^F=[(OC(CF_3)_3]^-$, 1,1,1,2,2,2,3,3,3-hexafluoro-2-propanol) in 2012 (Figure 1-7). $[NO][Al(OR^F)_4]$ was used to oxidize $P_4$ to $[P_9]^+$. Homopolyatomic cations are very rare, as most are anionic. The structure was determined by NMR spectroscopy, to reveal two $P_5$ cages linked and sharing the fifth

vertex in the form of a phosphonium atom.[79] $[Al(OR^F)_4]^-$ exhibit excellent stability towards Bronsted acids and highly electrophilic cations like $[CX_3]^+$ (X = Cl, Br, or I).[66]
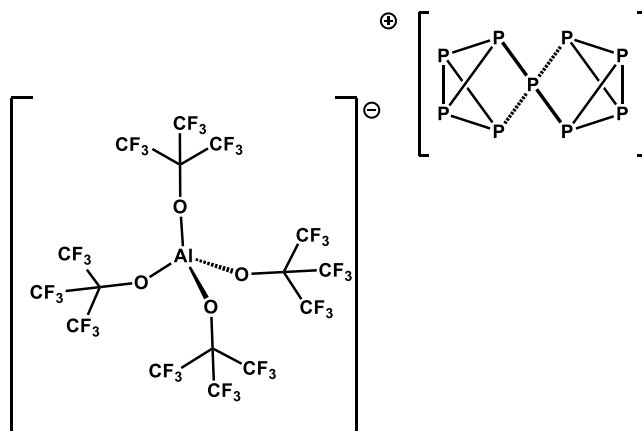


**Figure 1-7.** Structure of [P9]$^+$ stabilized by a [Al(ORF)$_4$]$^-$.

### 1.3.4 Alkoxyaluminates as multivalent ion electrolytes

The combination of Al–O bond strength and accessible aluminum hydride starting materials make these anions attractive and straightforward to synthesize. A wide variety of manipulation has been reported throughout literature due to the commercial availability of alkyl and aryloxide reagents.[66]

The choice of alkoxide ligand supporting the Al(III) center is reported to affect stability to oxidation and coordination properties.[80–82] As such, alkoxyaluminates are versatile and easily tunable compounds as multivalent ion electrolytes for batteries. Electrolytes incorporating alkoxyaluminates are reported to have high ionic conductivities or free-flowing environment for metal cations.[83] Alkoxyaluminates, of the anions mentioned so far, are promising electrolytes as they provide the most versatility and accessible synthetic tunability regardless of synthetic experience. Although they have

been extensively studied as WCA, their behavior and synthesis as multivalent ion electrolytes are still in its infancy. As you will encounter in Chapter 4, understanding synthetic anomalies and behavior of new ligands will better inform future research in alkoxyaluminate electrolytes to be further tailors for the target battery system.

### 1.3.5 Organic Cathodes toward multivalent-ion batteries

One of the main hurdles to the commercialization of multivalent ion battery technology is the availability of fully compatible battery components. As research in the synthetic applications of WCAs as electrolyte materials has begun to flourish, so has the area of new cathode materials for storing multivalent ions in batteries. Electrolyte work has shown a variety of efficient systems for reversible metal deposition, but there still remains the work to find cathodes and electrolytes that work well together. In addition to compatibility, the introduction of multivalent ions and their higher electropositive charge make reversible insertion chemistries sluggish as they relate to conventional inorganic cathode materials used in lithium-ion technology. Mono- and polymeric quinone based cathode materials exhibit highly reversible redox activity.[84] These types of materials undergo enolization to form $C-O^-$ from $C=O$ bonds reversibly. In a similar vein to WCAs, they owe stability to the delocalization of charge through an aromatic system (Figure 1-8). When incorporated as amorphous organic cathode systems, quinone analogs provide a possible solution exhibiting relatively facile intercalation-like activity and compatibility with common sulfonimide electrolytes.[85,86]
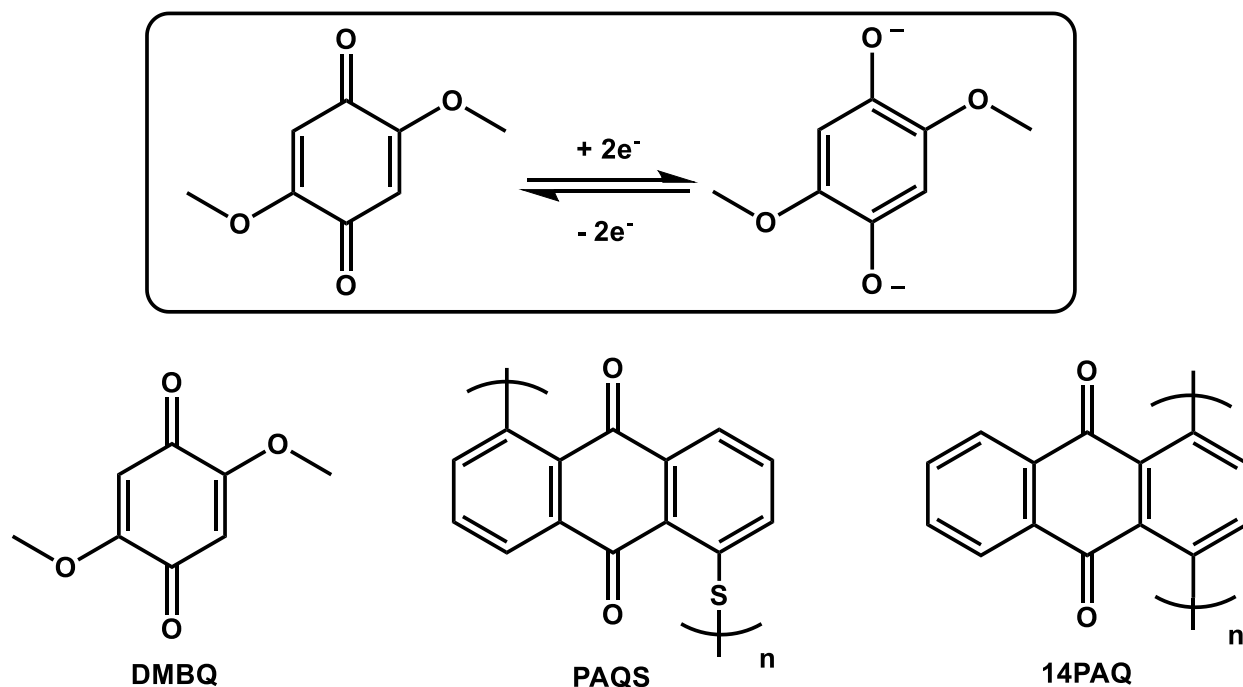
**Figure 1-8.** DMBQ (dimethoxybenzoquinone) redox activity and the analogous polymers, PAQS (poly(anthraquinonyl sulfide)) and 14PAQ (poly(1,4-anthraquinone)) used in organic cathode systems.

As cathode materials, organic molecules can be seen as more sustainable and environmentally friendly.[87,88] The potential for selective tunability and flexibility to the application at hand has been made apparent with transition metal transformations discussed above. The favorable intercalation environment is hypothesized to be in part due to the amorphous structure.

Electrolyte choice is vital as the cathode-electrolyte interaction should be void of nucleophilic interactions, and redox-active cathode should be poorly soluble to the electrolyte conditions. Pan et al. observed contrasting performance between $Mg(TFSI)_2$ electrolytes and $Mg(TFSI)_2$-$2MgCl_2$ with a Mg-DMBQ cathdode[86]. The latter displayed lower charge over-potentials and higher reversibility. Due to the presumed dissolution of DMBQ, rapid capacity fade was observed.

28

## 1.4   Conclusion

Work toward more sustainable science has been a motivating factor in this text. The application of synthetic organometallic skills toward multivalent rechargeable battery chemistry provides a unique point of view and the ability to make small modifications to a system and study its effects on battery performance. Additionally, as electrochemical windows are continually expanded, the skills to study chemical transformations or decomposition pathways can be very useful. Studying tunable platforms for electrolytes and cathode materials will provide a better understanding of the unique problems posed by multivalent ion batteries. Continued progress in research of safer, more earth-abundant energy storage systems is imperative as we search for more efficient, scalable, and cheap energy storage.

## 2 Synthesis and reactivity of next generation base metal heterobimetallic complexes

### 2.1  Introduction to polar binuclear reactivity

Progress in transition metal chemistry for catalysis has changed synthetic chemistry by enabling new bond formations. Of the variations discussed in the introduction, binuclear reactivity, like that of Frustrated Lewis Pairs (FLP) and heterobimetallic complexes has gained popularity in recent literature.[25,89] Every system possesses unique features like metals and ligands through which reactivity can be tuned.[5,22,90–92] The parallels with FLPs can be seen in early Mankad group developments.[28] [53,93] FLPs radically changed the way researchers design hydrogenation catalysts by using binuclear reactivity to share H–H bond activation across two main group centers, like a bulky phosphine and borane (Figure 2-1a). This motif changes direction from the typical single-site oxidative addition characteristic of precious metal catalysts. Binuclear cooperative bond activation expands beyond FLPs with transition metal analogs.[56,94] Transition metal systems using Lewis acid-based paired metal systems has its own history of study. More attention was previously paid toward structure characterization and stoichiometric activity,[95–102] with the exception of a few systems highlighting catalysis with these Lewis acid/base bimetallic complexes (Figure 2-1b).[48]

To date, the Mankad group has developed a library of reactive bimetallic complexes with applications in borylation and hydrogenation chemistry. While initially developed with hopes of activating inert substrates like $CO_2$ or C-H bonds, these bimetallic complexes have proved to be highly tunable species with applications in other useful transformations (Figure 2-1c).
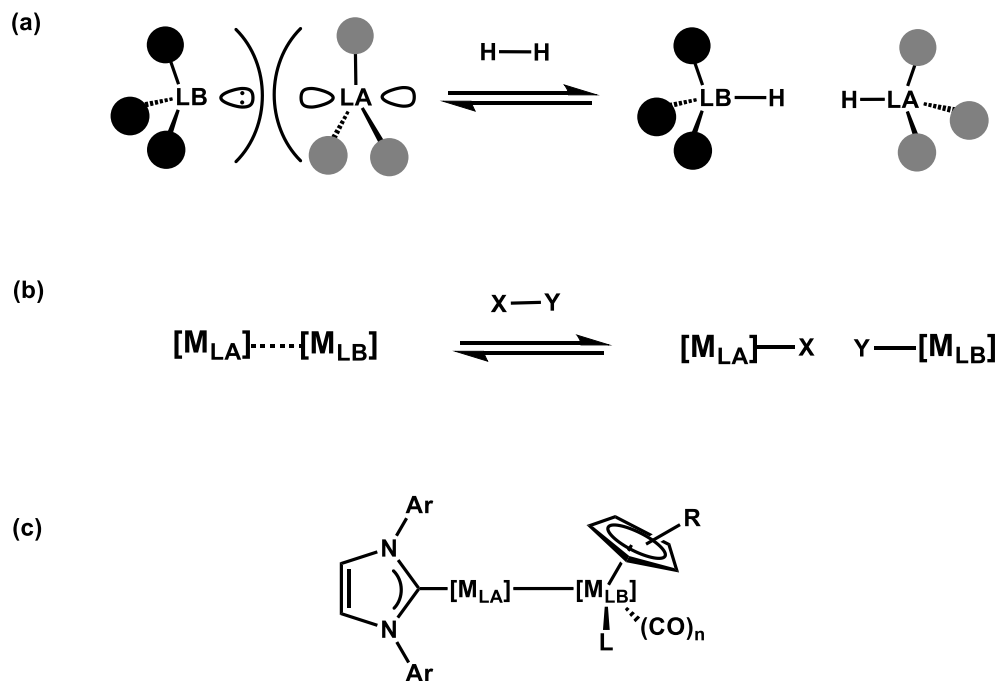


**Figure 2-1.** (a) $H_2$ activation by FLP, (b) cooperative X-Y activation by bimetallic complex, (C) general catalyst design in the Mankad motif

## 2.2 History of synthesis of heterobimetallic complexes in the Mankad group

The initial synthesis of heterobimetallic complexes in the Mankad group occurred through salt metathesis between a Lewis base, or nucleophilic metal carbonyl anion and a Lewis acid, or electrophilic metal halide. The resulting complex often provided a new $L_nM–[M_{co}]$ bond through which a whole research program has been developed.

One of the first examples of heterobimetallic synthesis in this group involved the reaction with the highly reported $[CpFe(CO)_2]^-$ $(Fp^-)$[103–105] with one equivalent of the N-heterocyclic carbene copper chloride (NHC), (NHC)CuCl,[106] to afford the new (NHC)CuFp complex (Figure 2-2). [107]

The next development involved the introduction of $L_nZnCl$ (Ln = (NHC) or β-diketiminate) to the library of Lewis acidic precursors and an alternative to (NHC)CuCl. This was the first instance of tunability of our heterobimetallic systems with the capability for changing the electrophilic fragment.[107,108]

Further developments in showing the success of tuning the Lewis acid partner, we could also demonstrate a tunability with different metal-carbonyl partners (Figure 2-2)..[52] At this point, methods available for modifying steric properties were primarily based on the choice of (NHC) ligand in the (NHC)Cu- fragment, with examples of electronic changes limited to full $d^{10}$ metal center variation. Further examples of electronic variation were based on the metal choice of the –[Mco] fragment. Electronic tunability by metal carbonyl selection alone has been supported by reported physical properties relating to nucleophilicity (Figure 2-2)[109] of the metal complex and $pK_a$[110]. Literature based on [$M_{co}$] fragments has afforded further expansion to tunability by using Cp*[111] or substituting CO ligands with less strongly coordinating ligands. [112]
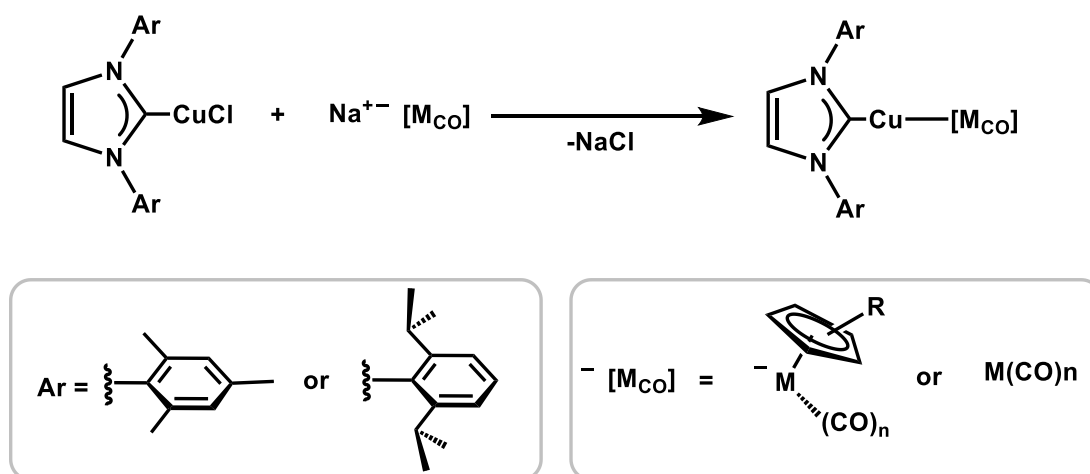
**Figure 2-2.** Synthesis of (NHC)Cu[$M_{co}$] by salt metathesis and relative nucleophilicity data.

Similar to FLPs, a dative [$M_{co}$]→Cu(NHC) bond was observed to fragment reversibly in solution through labeled crossover experiments.[52,113] While the neutral bimetallic complex is observed in solution and solid-state, there exists an equilibrium of species that will be explored further toward reactivity later in this chapter.

## 2.3 Heterobimetallic reactivity and catalysis

With the extensive literature surrounding copper carbene catalysis[106] and the stoichiometric reactivity of the Fp⁻ anion,[103,104] (NHC)CuFp was the initial target to study. Early forays to analyze reactivity of these novel bimetallic complexes found success with

C–H borylation chemistry. As covered in Chapter 1, the Hartwig group extensively detailed stoichiometric reactivity of the $[M_{co}]B(OR)_2$ complexes (where $[M_{co}]$ = Fp, Wp, Mn(CO)$_5$, or Re(CO)$_5$ and Wp*= Cp*W(CO)$_3$), Solutions of $[M_{co}]B(OR)_2$ in neat aromatic or saturated hydrocarbon solvent under UV light would borylate unactivated $C(sp^2)$–H or $C(sp^3)$–H bonds (Scheme 2-1 a, b).[58,114] These systems were unable to achieve catalytic turnover as $[M_{co}]$–H produced eventually dimerizes under UV light conditions. This system could not convert the resulting [Mco]–H back to $[M_{co}]B(OR)_2$ to undergo catalytic borylation.

**Scheme 2-1.** Stoichiometric (a) $C(sp^2)$-H and (b) $C(sp^3)$-H borylation reported by Hartwig, (c) catalytic photochemical $C(sp^2)$-H borylation reported by Mankad.

Inspired by the Hartwig group's work, the Mankad group hypothesized the use of cooperative bimetallic chemistry to trap the resulting $[M_{co}]$–H, FpH in this case, from borylation with (NHC)Cu-H. The products of this reaction were $H_2$ and (NHC)CuFp. In practice, Mankad and coworkers observed Cu/Fe-facilitated catalysis of $C(sp^2)$-H

borylation in which H-B activation produced FpBpin as expected. After borylation of benzene, $H_2$ elimination affords the starting catalyst (Scheme 2-1c).

Mimicking the evolution of the Hartwig group's stoichiometric work[59,60], attempts to provide a pentane soluble catalyst through trimethylsilylation of the NHC backbone[115] were successful but only afforded stoichiometric conversion of HBpin to (*n*-pentyl)Bpin.

The final progression of the IPrCuFp system was modification by substitution of carbonyl ligands for phosphines(Scheme 2-2) This change was inspired by the history of catalyzed borylation chemistry in which Cp*Re(CO)$_3$[116] reacted under photochemical conditions later to be surpassed by thermal conditions used by CO-free Rh catalysts like Cp*Rh($\eta^4$-C$_6$Me$_6$).[117–119] Photochemical CO dissociation of FpBpin to a 16 electron reactive intermediate is a crucial step in stoichiometric borylation reactions. Various CpFe(PR$_3$)$_2$Bpin derivatives were synthesized to provide labile ligands under thermal conditions, mimicking the photochemical pathway. CpFe(PEt$_3$)$_2$Bpin was determined to be the only complex able to undergo thermal borylation of benzene at 70 °C.[120] The byproduct, CpFe(PEt$_3$)$_2$H, proved to be unreactive with the (NHC)CuH counterpart (Scheme 2.2), and hence unable to undergo catalytic reactivity.
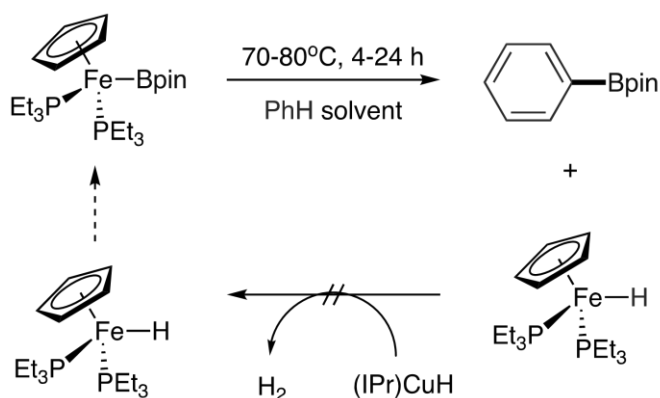


**Scheme 2-2.** Stoichiometric thermal C(sp$^2$)-H borylation with CpFe(PEt$_3$)$_2$Bpin.

Another significant catalytic achievement is the bimetallic *E*-selective hydrogenation of alkynes.[56,121,122] (NHC)M–[M$_{co}$] (M= Cu, Ag) complexes were observed to undergo *E*-selective hydrogenation chemoselectively for alkynes under H$_2$ atmosphere. This discovery led to the development of a system finding cooperative bimetallic activation of H$_2$ and reductive elimination of various semi- and fully hydrogenated alkynes (Scheme 2-3).
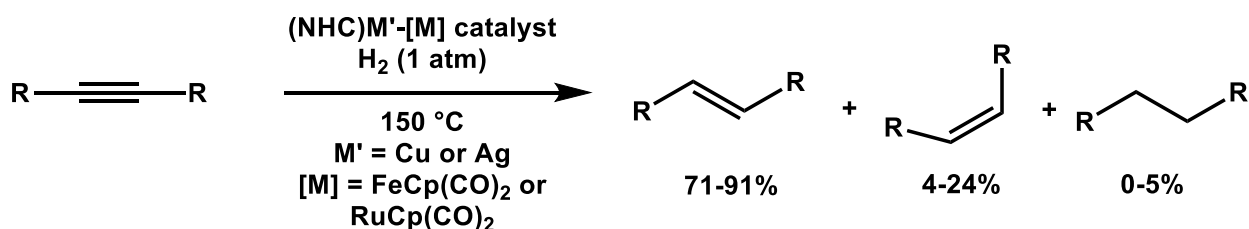


**Scheme 2-3.** Cooperative bimetallic E-selective semi-hydrogenation of alkynes.

## 2.4 Modifications toward next-generation heterobimetallic complexes

Numerous impactful findings have been reported around the reactivity of the heterobimetallic (NHC)M–[M$_{co}$] metal motif. One of the main advantages is the library of bimetallic fragments available to tune borylation[123], hydrogenation[122], and even stannylation chemistry[124]. Some of the drawbacks to these systems are the high catalyst loading and harsh reaction conditions needed to undergo catalysis. This chapter will detail some of the modifications made toward next-generation heterobimetallic complexes and their reactivity related to some of the older systems mentioned above. Providing new methods toward modification of bimetallic complexes used by the Mankad group will help inform future work towards building heterobimetallic scaffolds applied to their target

catalysis. The introduction of less electron-rich Lewis acidic fragments has shown to provide new metal–metal interaction and bond activations not seen previously, while substitution of carbonyl ligands in the standard Lewis basic fragments has lent new understanding of bimetallic borylation chemistry.

### 2.4.1  Modifying electrophilic fragment: moving from $d^{10}$ to $d^8$

To this point, significant modifications to the (NHC)Cu-[$M_{co}$] motif were applied toward the nucleophilic metal-carbonyl fragment. Efforts to manipulate the Lewis acidic fragment had seen only small modifications to the NHC structure while maintaining a $d^{10}$ metal center.[121,125,126] For the first attempt at modification away from full $d^{10}$ transition metal centers, we opted for group 10 Ni(II)-pincer complexes that would provide a more electron-poor Lewis acidic metal center and more polar, reactive bimetallic complex.[127] Ni(II)-pincers have an extensive history of their own detailing a variety of chemistry around Ni(II)-H insertion.[128–131] Incorporating Ni(II) into our bimetallic motif would provide a very stable Ni(II)-H in events that the decomposition (NHC)Cu-H hindered reactivity.[132]  The standard salt metathesis method to which our group had become accustomed resulted in no reaction between the (POCOP)NiCl and NaWp (POCOP = resorcinolbisphosphinite). The last step in catalytic borylation is the bimetallic elimination of hydrogen. A combination of the (POCOP)NiH and HWp fragments in aromatic solvent or pentane provided slow conversion to the bimetallic (POCOP)NiWp complex. The relatively slow conversion differs from the immediate $H_2$ elimination observed with the (NHC)CuFp system, likely due to the extra steric hindrance from the (POCOP) pincer ligand. The solid-state structure displays a close association between the two metals by an end to end bound isocarbonyl ligand rather than the typical metal-metal bond present in the group

11 complexes (Figure 2-3). Further characterization with FT-IR spectroscopy reveals the highly redshifted carbonyl signal from 1784 $cm^{-1}$ to 1650 $cm^{-1}$ consistent with the effect of the bridging carbonyl.
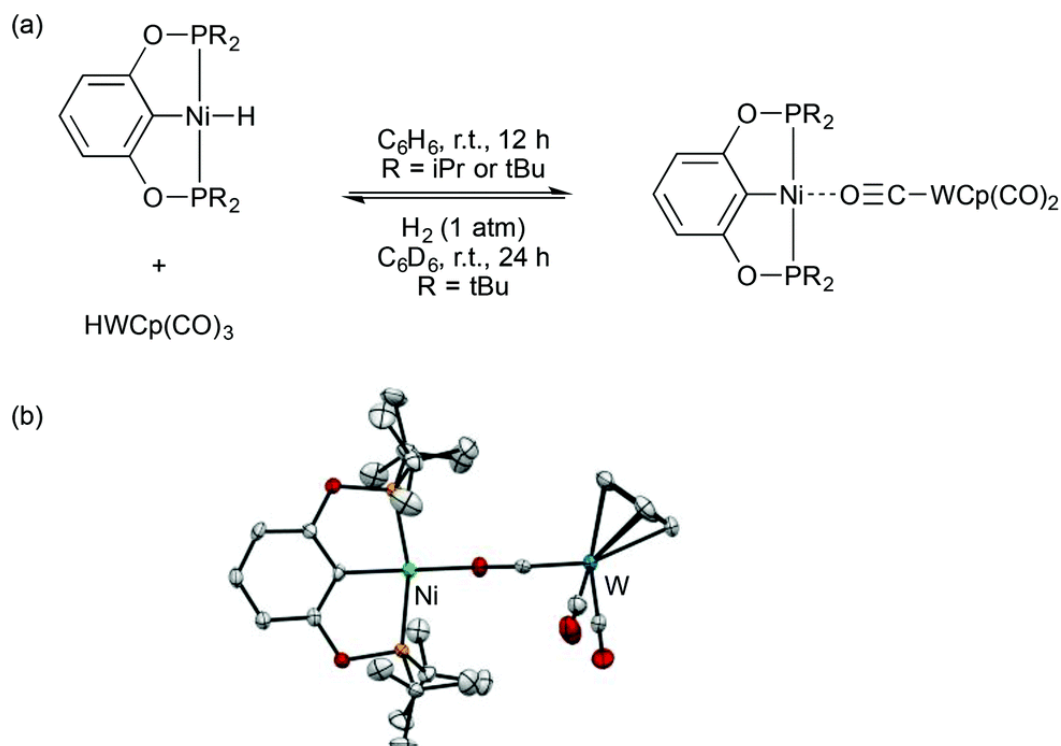


**Figure 2-3.** (a) Synthesis of ($^{tBu}$POCOP)NiWCp(CO)$_3$ by bimetallic H$_2$ elimination and (b) its solid-state structure determined by single-crystal X-ray diffraction.

### 2.4.2 Reactivity of (POCOP)NiWp complexes

Exposure of (POCOP)NiWp in C$_6$D$_6$ to H$_2$ proved the bimetallic elimination to be reversible with the observed corresponding bimetallic activation of H$_2$ (Scheme 2-4). Levina et al. published similar work with the (PCP)NiWp analog exhibiting reversible H$_2$ reactivity proceeding through an end to end bound [Ni]-H···H-[W] intermediate.[133] Single-crystal X-ray diffraction information shows the [Ni/W] system to be a closer analog to the FLP systems by which our group was inspired.

In an attempt to compare the reactivity of the (POCOP)NiWp complexes to (NHC)Cu[$M_{CO}$], experiments incorporating hydroboranes were run. Previous systems prove activation of H-B and H-H bimetallic bond activation due to their success in catalytic systems and mechanistic analysis, but stoichiometric activated counterparts were never isolated.[108,122,126,134] Having observed direct activation of $H_2$ to (POCOP)NiH and WpH, we expected to see the WpB(OR)$_2$ compounds when introducing (POCOP)NiWp to HBcat or HBpin. Unfortunately, only the presence of (POCOP)NiH complexes were ever observed, and the state of the resulting borane was never determined. ^{11}B NMR resonances (21ppm) corresponded to that of a major product containing a B-O bond. These resonances were similar to those of (OR)$_2$B-O-B(OR)$_2$ observed in previous studies.[135] The tungsten borane was presumably unstable to these conditions, but no isolable compounds were analyzed further from the reaction mixture.
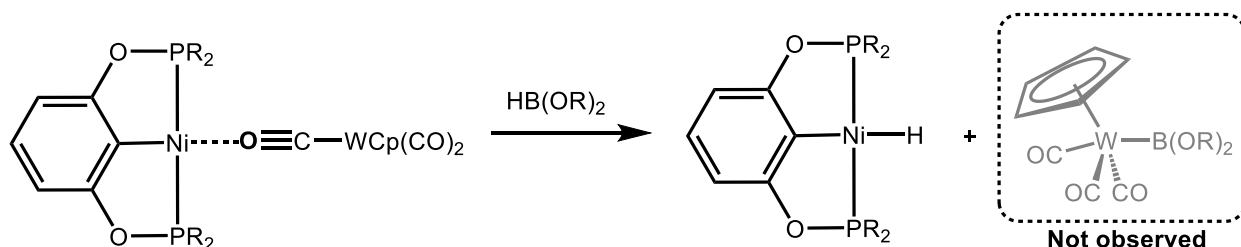


Scheme 2-4. Attempted H-B bond activation of HB(OR)$_2$ (pinacolborane).

With stable H-H bond activity observed, we attempted to extend the comparison to alkyne hydrogenation previously established by our first-generation bimetallic complexes. Despite numerous variations to reaction conditions, (POCOP)NiWp variants under $H_2$ only displayed H-H activation products and no hydrogenation products with

diphenylacetylene. To test whether sterics were to blame, the less hindered terminal alkyne, phenylacetylene, was determined to react unexpectedly.

Guan recently reported chemistry of (POCOP)MH (M = Ni or Pd) complexes with phenylacetylene.[136] The reaction between phenylacetylene and (POCOP)PdH favored dehydrogenation of the terminal C-H to form the acetylenic [Pd] counterpart (Scheme 2-5a). The analogous (POCOP)NiH, when reacted with phenylacetylene, favored migratory insertion into the C-C triple bond. (Scheme 2-5a).
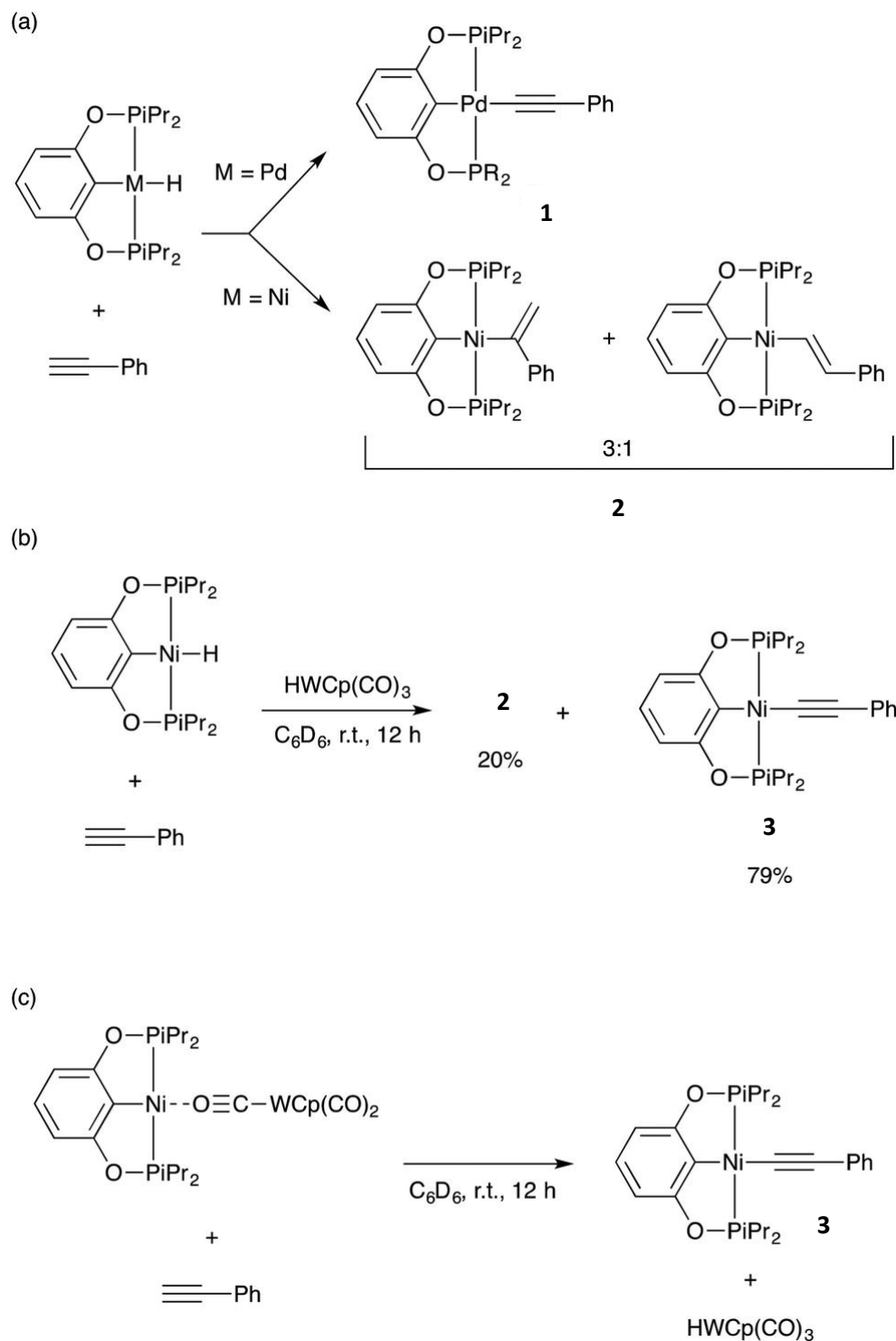
**Scheme 2-5.** (a) Metal-dependent selectivity observed by Guan. (b) Bimetallic switch in selectivity. (c) Bimetallic C–H activation of diphenylacetylene.

We found that in the presence of a [Mco] metal site, the reaction with phenylacetylene acts like a switch to favor Pd-like reactivity. ($^{iPr}$POCOP)NiH and WpH exposed to phenylacetylene resulted in the majority acetylide complex with only small quantities of the 1,2- and 2,1-insertion products (Scheme 2-5b). The selectivity between C–H activation and migratory insertion can be switched by toggling the presence of the WpH complex. Presumably, minor insertion products are formed from (POCOP)NiH reacting with phenylacetylene. In contrast, the direct C-H activation occurs by the initial elimination of H$_2$, followed by bimetallic activation of phenylacetylene (Scheme 2-6). To corroborate our findings, exposing [($^{iPr}$POCOP)Ni][Wp] to phenylacetylene produced the acetylenic Ni(II) complex (3) and WpH with no evidence of the 1,2- or 2,1-insertion products(Scheme 2-6)
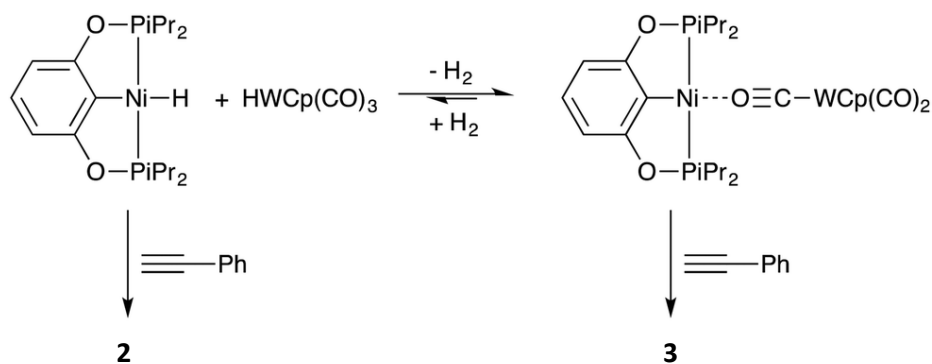


**Scheme 2-6.** Proposed scheme for observed selectivity between mono- and bimetallic complexes.

The Ozerov group has shown the utility of activating terminal alkynes by reporting ($^{iPr}$POCOP)PdH mediated catalytic dehydrogenative borylation of terminal alkynes.[137] The bimetallic C(sp)-H activation reported here ideally could provide similar catalytic conditions, but numerous efforts to find those conditions failed. Efforts to

stoichiometrically produce a borylated product showed no reaction between hydroboranes and any combination of (POCOP)NiWp and phenylacetylene or Ni(II)-acetylide complex with WpH. Without a route toward borane activation and the uncertain stability of (POCOP)NiWp with boranes, we found no other directions for this reaction motif.

Believing we have found a unique mode of bimetallic reactivity, we sought to investigate further transformation of the N(II)-acetylide. Various [(POCOP)Ni] analogs and their reactivities have been studied[136,138,139], and recent work has highlighted the utility of atom economic formation of carboxylates and transformation of the acetylenate type precursors for synthesis. [140–142] Particularly notable is the reactivity of (POCOP)Ni-R (R = H, Me) with $CO_2$ to form analogous formate and acetate compounds.

Similar reactivity was observed with (POCOP)NiH and (POCOP)Ni-CCPh (CCPh = phenylacetylide). We hypothesized a catalytic cycle shown in Scheme 2-7 could be achieved. The barrier to $CO_2$ insertion proves to be lower in energy in Ni(II)-H under $CO_2$ (1 atm, 25 °C) compared to Ni(II)-acetylides. Various conditions were tested to find that higher pressures (3 atm $CO_2$, 70 °C) are needed to completely convert Ni(II)-acetylides to the $CO_2$ inserted counterparts.
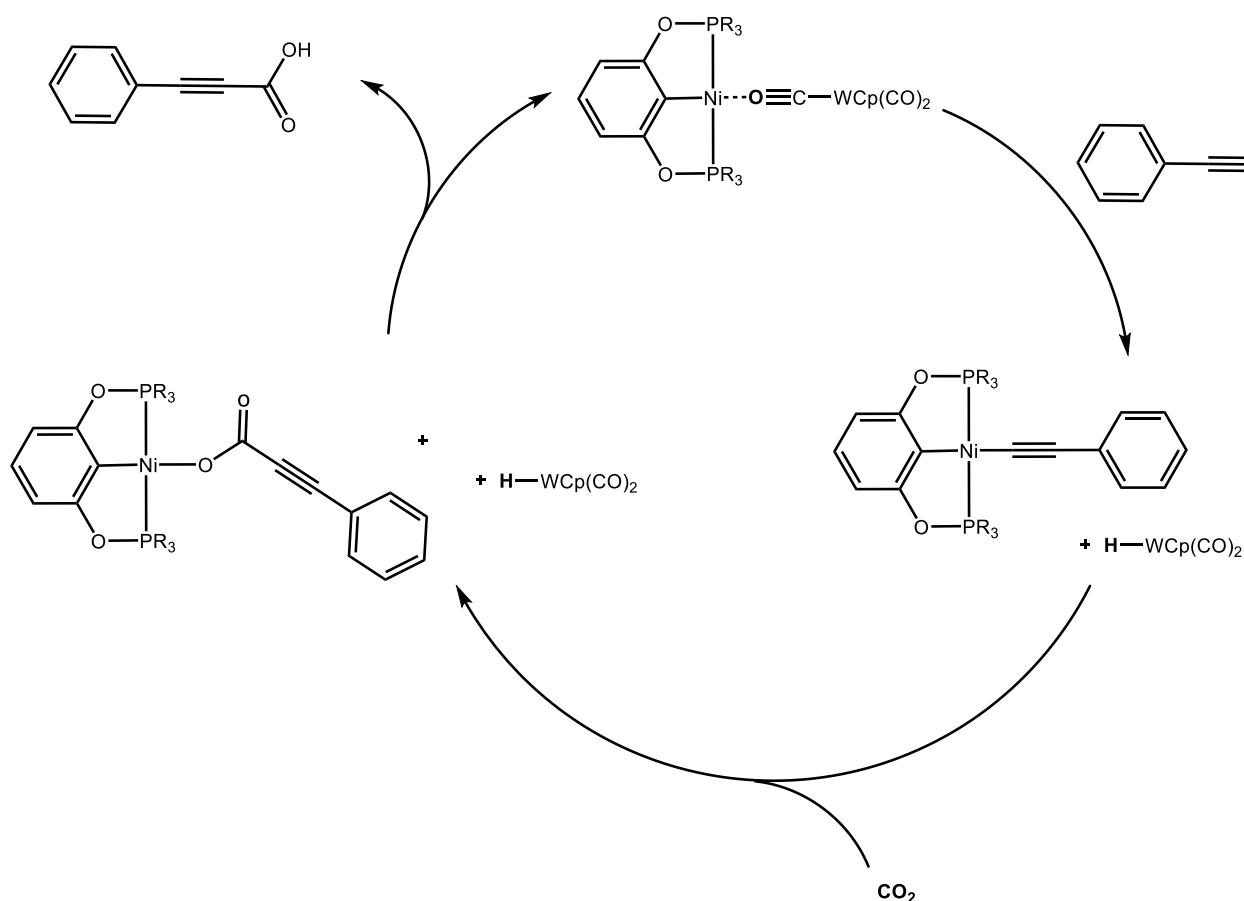
**Scheme 2-7.** Proposed cycle for attempted (POCOP)NiWCp(CO)₃ catalyzed carboxylation of alkynes.

The resulting Ni(II)-acetylenate was confirmed by a direct synthesis between (ⁱᵖʳPOCOP)NiCl and the lithiated phenylacetylenate. Producing a carboxylic acid proved unfeasible due to the acidity of the acid and the tendency for the bimetallic complex to deprotonate acidic hydrogens, similar to that of the phenylacetylene. With established conditions to provide Ni(II)-acetylenate, we attempted to turn over the cycle by introducing various additives and drive reformation of the bimetallic (POCOP)NiWp complex. Boranes, silanes, sodium *tert*-butoxide, and hydrogen chloride in diethyl ether in stoichiometric amounts provided no discernable new products. Slight reactivity amounted

to minor mixtures that were not characterized successfully. Boranes and silanes were introduced with the idea of producing a (POCOP)Ni-H to drive reformation of the bimetallic by $H_2$ elimination. Acid and base additives only served to convolute NMR spectra with minor unknown side products. In all cases, no bimetallic products were observed stoichiometrically, and no new carboxylates were observed under catalytic conditions. With numerous attempts to turn over the cycle, we observed the unreacted Ni(II)-acetylenate as the major component in NMR spectra. It seemed as though the Ni-O bond formation was favored over any other hydride source, despite evidence of Ni(II)-formate reactivity with hydroboranes.[143]

Incorporation of a relatively electron-poor Ni(II) metal center in the heterobimetallic scheme amounted to a new heterobimetallic complex showing a more "frustrated" metal–metal interaction. Compared with the original full $d^{10}$ electrophiles, more immediate bond activation character was displayed with H-H, H-B, and acidic C-H bonds not readily visible in previous catalytic systems. Further work toward bond formation, and bimetallic formation in particular, would have a high impact on new routes for bimetallic synthesis. By expanding the toolbox of methods for bond formation, decisions in catalyst design can be impacted by pinpointing undesired stable intermediates and unwanted side reactions.

## 2.5 Synthesis and reactivity of LCuWp*(R) analogs beyond phosphines

Previous work toward modification of the Lewis basic fragment in the heterobimetallic motif had been primarily based on the introduction of mono- and bidentate phosphine ligands in place of carbonyls. Previous work with iron boryl complexes supported by bulky phosphine ligands have exhibited thermal lability in stoichiometric borylation.[144]

Rather than utilizing steric bulk to force ligand dissociation, we sought to develop a system with closer relations to [$M_{co}$] complexes but still targeting the thermal lability of ligands to apply to previously studied bimetallic borylation chemistry. We chose the isoelectronic isocyanide, in particular *t*-butylisocyanide, for its ease of identification by ^{1}H NMR and the added solubility afforded by the butyl group. Isocyanides can be useful ligands to replace CO as they are good σ-donors but poorer π-acceptors. (Figure 2-4). Incorporating isocyanide ligands in place of carbonyl ligands could potentially provide a less strongly chelating ligand and thus demonstrate thermal lability necessary for borylation chemistry.
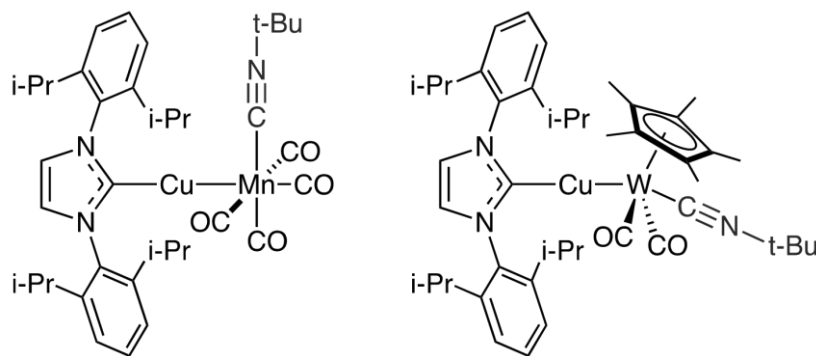


**Figure 2-4.** Monosubstituted t-butylisocyanide analogs of [$M_{co}$] complexes

IPrCuMn(CO)$_4$(*t*BuNC) and IPrCuWCp*(CO)$_2$(*t*BuNC) were synthesized from salt metathesis of their (NHC)CuCl and Na[$M_{co}$] counterparts. When introduced to HBpin in aromatic solvents at temperatures up to 120 °C, neither complex afforded evidence of

C(sp$^2$)-H borylation products when analyzed by $^{11}$B NMR. The only evidence to note were instances of a small unknown resonance at 24 ppm.

Although isocyanides did not prove to be more labile under thermal conditions, IPrCuWCp*(CO)$_2$(tBuNC) did show high solubility in pentane. Recalling the previous stoichiometric work toward C(sp$^3$)-H borylation by Hartwig[116], we decided to expose the t-butylisocyano substituted analog to HBpin in pentane under UV light conditions. Previous catalysts designed by our group did not display sufficient solubility in pentane for catalytic borylation. Evidence of n-pentylBpin was present in yields as high as 30% at 20% catalyst loading, signifying a catalytic process with just over one turnover. Similar to experiments under thermal conditions, a resonance of 24 ppm was present in $^{11}$B NMR spectra. The unknown resonance was likely the insertion of HBpin into the C-N bond of the ligated isocyanide. The same outcome was confirmed by an independent synthesis between the NaWCp*(CO)$_2$(tBuNC) and ClBpin or ClBcat separately, displaying the same $^{11}$B NMR signal and a new singlet present in proton NMR. We hypothesized that based on the photochemical activity that activation of B-H bond occurred, forming an unstable byproduct, through which the reaction was shut down (Scheme 2-8). Intramolecular borylation of the isocyanide ligand was highly favored over intermolecular C(sp$^3$)-H borylation of pentane. The decomposition of the active tungsten species explains the low catalytic activity by self-poisoning from the isocyanide ligand. Similar reactivity in metal carbonyls has been reported by the Figueroa group.[145]
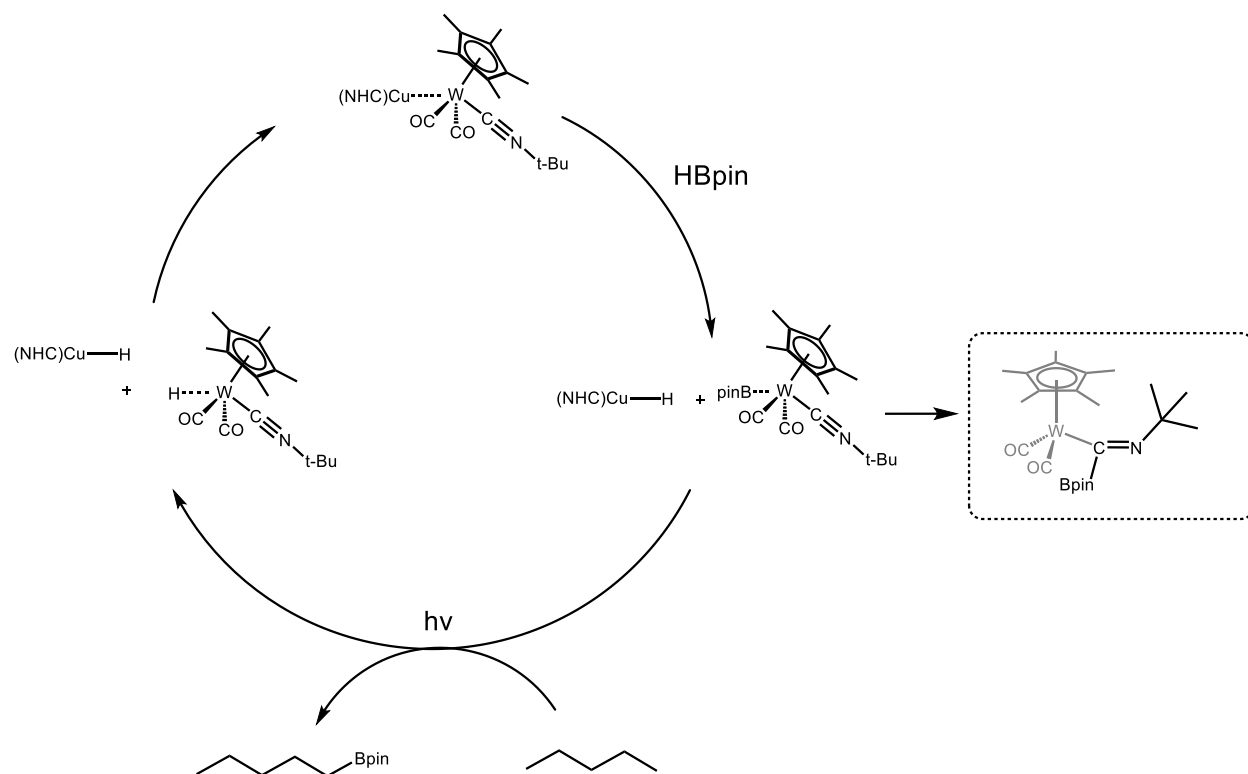
**Scheme 2-8.** Proposed catalytic cycle for $C(sp^3)$-H borylation of pentane and self-poisoning of $(NHC)Cu-WCp(CO)_2(tBuNC)$.

## 2.6 Conclusion

Further work regarding labile ligands toward borylation chemistry of metal-carbonyl systems should be focused on providing highly steric encumbering ligands without functional groups susceptible to borylation or insertion chemistry. In addition to self-poisoning catalytic conditions, future work should focus on expanding methods for heterobimetallic complex formation to aid decision making in catalytic turnover.

Chapter two has highlighted some of the early work towards modifying the (NHC)M–[$M_{co}$] motif for next-generation heterobimetallic systems in the Mankad group. It serves

as a reservoir of a variety of concepts that have contributed to the toolbox of methods for synthesizing new bimetallic complexes and the effects of modifications to the Lewis acidic and basic fragments in the heterobimetallic scheme. These findings will serve a purpose to inform further research toward tailoring heterobimetallic systems for new bond activation, desired catalytic activity, and targeted reaction conditions.

## 3 Mixed Phosphine/Carbonyl Derivatives of Heterobimetallic Copper-Iron and Copper-Tungsten Catalysts

### 3.1 Introduction

Construction of complex organic scaffolds from simpler building blocks generally relies on the presence of reactive heteroatom functional groups or unsaturated bonds. Using ubiquitous C-H positions directly in coupling reactions is comparatively desirable because it greatly reduces the number of synthetic steps by circumventing the need for pre-installed functionalities.[146–151] However, the thermodynamic stability and kinetic inertness of C-H bonds present great challenges to be overcome, as does the problem of site selectivity in organic substrates containing multiple distinct C-H sites. In this regard, transition metal-catalyzed C-H borylation is one of the most promising technologies to emerge recently.[152,153] In this transformation, C-H bonds are converted directly to organoboronic esters that, in turn, can be used in the Suzuki-Miyaura reaction or translated into a plethora of other functional groups.[154] Crucially, the C-H borylation reaction obeys well-defined site-selectivity rules guided primarily by C-H acidity or steric accessibility, and catalysts have been developed that facilitate mild reaction conditions. These qualities are best displayed with C-H borylation catalysts based on the precious metal, Ir, ligated by bisphosphine, bipyridine, and pincer systems. Recent advances have been made with catalytic C-H borylation using non-precious metals such as Fe,[155–157] Ni,[158] and Co,[159–163] as well as with a metal-free strategy employing frustrated Lewis pairs.[164] While promising, these non-precious metal systems typically exhibit efficient reactivity only for highly activated and/or acidic C-H bonds and require solvent quantities

of substrate in order for borylation of unactivated C-H bonds to occur. Thus, more work is required to access non-precious metal catalysts for efficient borylation of unactivated C-H bonds in stoichiometric quantities.



(a)    NHC = N-heterocyclic carbene

(i) B-H activation
(ii) C-H borylation
    L = L' = CO: UV light
    L = L' = PEt$_3$: thermal
(iii) H-H elimination
    L = L' = CO: rapid
    L = L' = PR$_3$: no reaction
    L = CO, L' = PR$_3$: rapid (this work)

(b)

p$K_a{}^{THF}$ estimate:    30        39        48
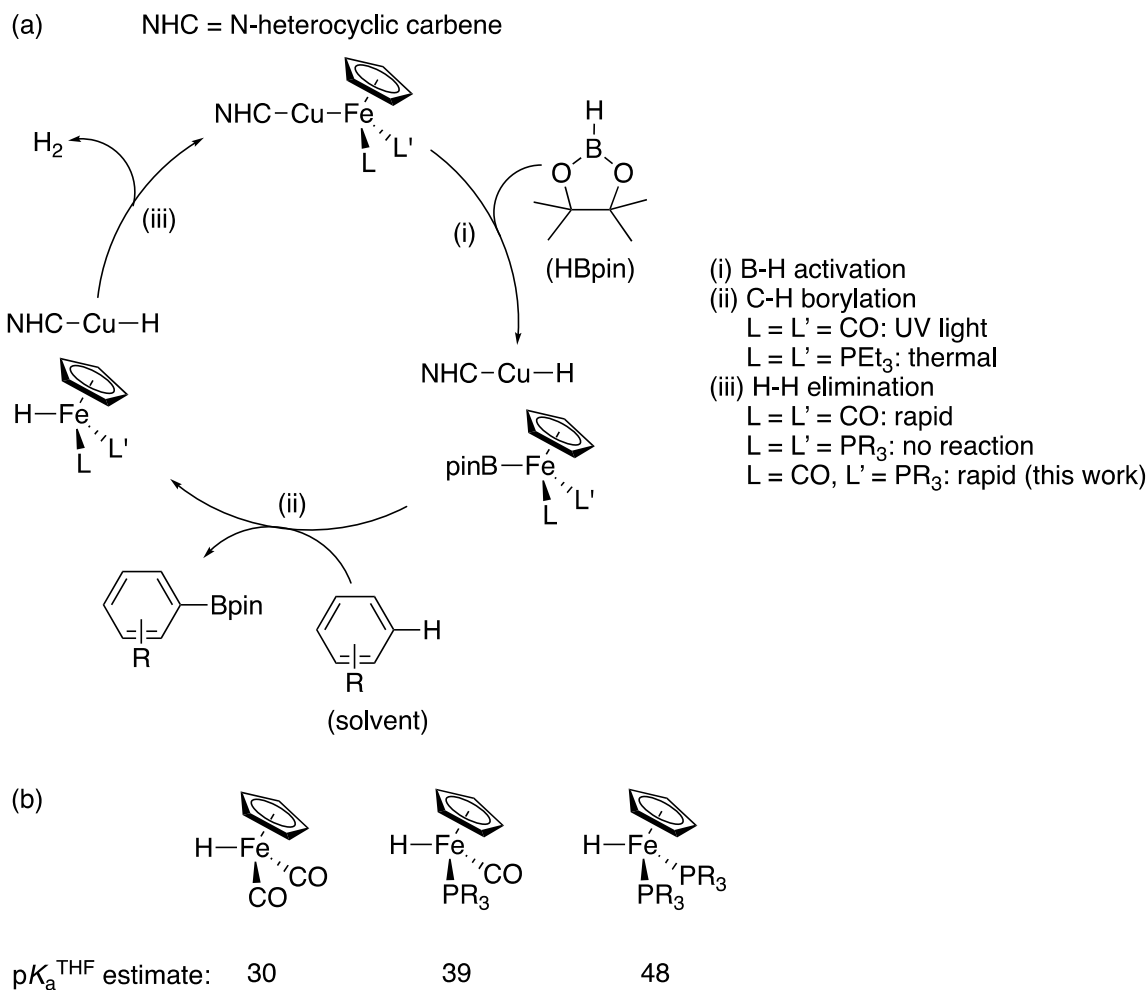
**Scheme 3-1.** (a) Summary of heterobimetallic C-H borylation catalysis; (b) Estimates of [Fe]-H p$K_a$ values in THF based on ligand acidity constants.[110]  A similar scheme is operative for (NHC)Cu-WCp*(CO)$_2$L analogs (L = CO or PR$_3$).

A long term goal of our research group is to use the cooperative behavior of heterobimetallic catalysts to uncover catalytic transformations with non-precious metals that complement single-site precious metal systems.[89,121,135] One of our first forays into

this area involved the discovery that $(IPr)Cu-FeCp(CO)_2$,[108] and later $(IPr)Cu-WCp^*(CO)_3$,[165] are active catalysts for borylation of arene solvents upon exposure to UV light with a 450-W Hg lamp over 24h (IPr = $N,N'$-bis(2,6-diisopropylphenyl)imidazol-2-ylidene). These systems rely on the known stoichiometric borylation activity of $FeCp(CO)_2B(OR)_2$ and $WCp^*(CO)_3B(OR)_2$ intermediates under UV irradiation conditions that were studied in detail by Hartwig many years ago (Scheme 3-1a, step ii).[58,60,114] In our heterobimetallic system, the copper-carbene unit acts as a hydride shuttle that allows for the active Fe- or W-based borylating agents to be continuously regenerated catalytically via cooperative heterobimetallic B-H activation and H-H elimination reactions that occur thermally (Scheme 3-1a, steps i and iii).[113] Because the C-H borylation step (Scheme 3-1a, step ii) is known to involve photochemical CO dissociation,[166] we have been targeting a thermal C-H borylation catalyst by replacing one or more CO ligands with labile phosphines.[23] We were able to demonstrate that $FeCp(PEt_3)_2Bpin$ mediates stoichiometric, UV-free borylation of arene solvents at 70-80°C due to thermal $PEt_3$ lability from this sterically crowded complex, but catalysis was precluded because heterobimetallic H-H elimination from $(IPr)CuH + FeCp(PEt_3)_2H$ (Scheme 3-1a, step iii) did not occur readily.[120] Our hypothesis is that this H-H elimination step requires a highly polarized system where a hydridic [Cu]-H species reacts with a protic [Fe]-H species.[122] Indeed, while $FeCp(CO)_2H$ is known to be significantly protic in character, the $FeCp(PEt_3)_2H$ analog is less acidic by ~19 p$K_a$ units (Scheme 3-1b).[110] This has led us to target mixed phosphine/carbonyl catalysts of the type $(NHC)Cu-FeCp(CO)(PR_3)$, which we hope will mediate thermal C-H borylation while facilitating catalytic turnover via $FeCp(CO)(PR_3)H$ intermediates with more protic character (Scheme 3-1b). Synthesis and

characterization of such mixed phosphine/carbonyl catalysts are reported in this manuscript, as is the demonstration that heterobimetallic H-H elimination does indeed proceed as expected when at least one carbonyl ligand is present in the system.

## 3.2 Results and discussion

The iron hydride complexes $FeCp(CO)(PR_3)H$ were observed to react rapidly within 5 minutes with *in situ*-generated $(IPr)CuH$ to release $H_2$ and provide $(IPr)Cu$-$FeCp(CO)(PR_3)$ complexes (**1a-d**, Scheme 3-2). In typical reactions, the crude product mixtures contained a minor side-product tentatively identified as $CpFe(IPr)(CO)H$ (hydride signal: -17.35 ppm) by comparison to the Ru analog,[122] and complexes **1a-d** could be isolated in 21-44% recrystallized yield. Not only does this dehydrogenation reaction provide a synthetic method for these new mixed phosphine/carbonyl heterobimetallic complexes, but it provides further indication that the catalytically relevant $H_2$ elimination step (Scheme 3-1, step iii) is viable if the [Fe]-H $pK_a$ is low enough. Complexes **1a-d** were characterized by multinuclear NMR spectroscopy and FT-IR spectroscopy. X-ray crystallography data was obtained for complexes **1b** and **1d**. Vibrational data for the carbonyl ligands and selected bond metrics are shown in Table I for comparison to $(IPr)Cu$-$FeCp(CO)_2$,[52,107], and solid-state structures are depicted in Figure 3-1. Unlike the thermally stable $(IPr)Cu$-$FeCp(CO)_2$ derivative, the mixed phosphine/carbonyl derivatives **1a-d** decompose at a measurable rate (2-12 hours at room temperature, see Supplementary Material), which we expect will limit their utility as catalysts.

(IPr)CuO$^t$Bu + HSi(OEt)$_3$

"(IPr)CuH"

benzene, -35°C—>r.t., 5 min

(IPr)CuFeCp(CO)(PR$_3$), 21-44%
**1a**: PR$_3$ = P$^n$Bu$_3$
**1b**: PR$_3$ = PEt$_3$
**1c**: PR$_3$ = PPhMe$_2$
**1d**: PR$_3$ = PPh$_2$Me
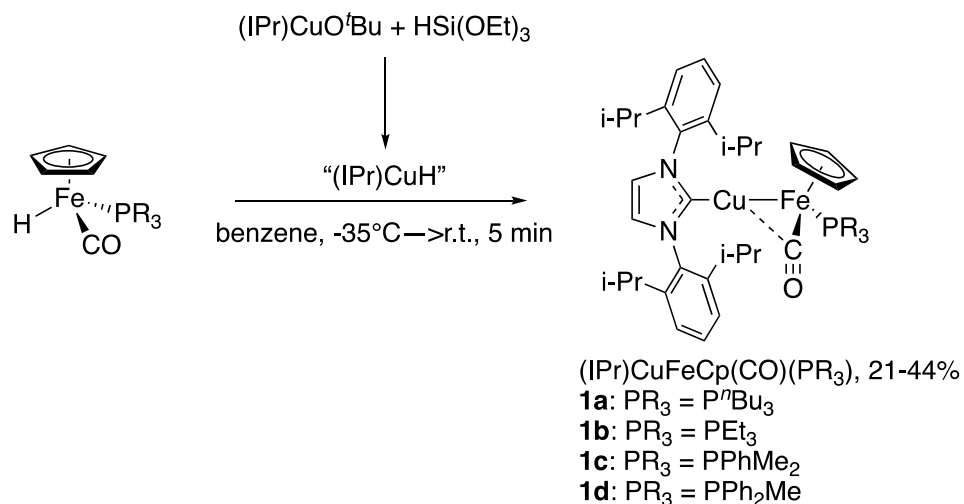
**Scheme 3-2.** Synthesis of mixed phosphine/carbonyl Cu-Fe heterobimetallic complexes.
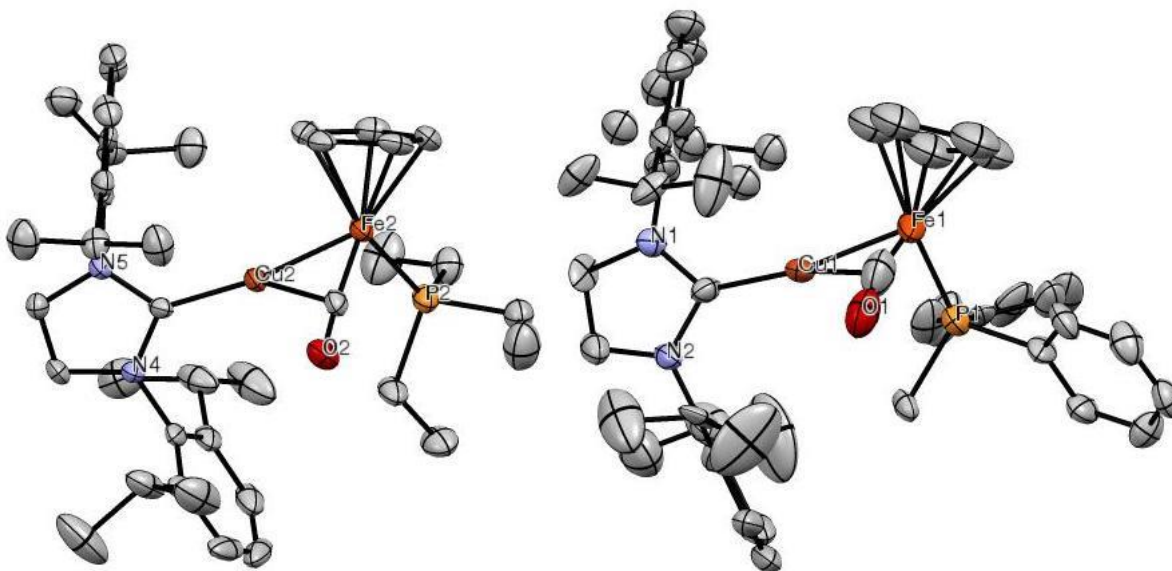


**Figure 3-1.** X-ray crystal structures of **1b** and **1d**, with ellipsoids shown at the 50% probability level. Hydrogen atoms and co-crystallized solvent molecules have been omitted, and only one of two independent molecules in the asymmetric unit of **1b** is shown. Selected bond metrics are given in Table I.

**Table I.** Selected data comparisons for Cu-Fe heterobimetallic complexes

| Complex | $\nu_{CO}$ (cm$^{-1}$) | $d$(Cu-Fe) (Å) / FSR[a] | $d$(Cu⋯CO) (Å) | $d$(C-O) (Å) | ∠C$_{NHC}$-Cu-Fe (°) | ∠Fe-C-O (°) |
|---|---|---|---|---|---|---|
| (IPr)Cu-FeCp(CO)$_2$[b] | 1914, 1849 | 2.3462(5) / 1.004 | 2.423(3), 2.749(3) | 1.169(3) | 170.16(7) | 177.2(2) |
| (IPr)Cu-FeCp(CO)(P$^n$Bu$_3$) (**1a**) | 1795 | n.d.[c] | n.d.[c] | n.d.[c] | n.d.[c] | n.d.[c] |
| (IPr)Cu-FeCp(CO)(PEt$_3$) (**1b**)[d] | 1791 | 2.3331(9) / 0.998 | 2.378(5) | 1.186(6) | 169.21(14) | 176.5(4) |
| (IPr)Cu-FeCp(CO)(PPhMe$_2$) (**1c**) | 1794 | n.d.[c] | n.d.[c] | n.d.[c] | n.d.[c] | n.d.[c] |
| (IPr)Cu-FeCp(CO)(PPh$_2$Me) (**1d**)[e] | 1813 | 2.299(2) / 0.983 | 2.440(18) | 1.13(2) | 170.2(15) | 170.2(15) |

[a]FSR = formal shortness ratio.[167] [b]Data from literature references.[52,107] [c]n.d. = not determined. [d]Structural data is given for one of two independent molecules in the asymmetric unit of **1b**. [e]R value is 0.34, so the reader should take caution in interpreting metrical parameters.

The accumulated data indicate, as expected, that phosphine ligation renders the Fe centers more electron-rich than in the parent (IPr)Cu-FeCp(CO)$_2$ derivative. This is

particularly evident by examination of the carbonyl stretching frequencies for complexes **1a-d**, which are in the 1791-1813 cm$^{-1}$ range and shifted to significantly lower energy than those of (IPr)Cu-FeCp(CO)$_2$ (Table I). Both **1b** and **1d** feature semibridging carbonyl ligands,[168] which is indicated by van der Waals Cu···C$_{CO}$ contact and confirmed by tabulation of Curtis's $\alpha$ parameter being 0.39 in both cases and thus in between the bridging CO ($\alpha \leq 0.1$) and terminal CO ($\alpha \geq 0.6$) regimes.[169] The impact on metal-metal bonding of the increased electron density at Fe is a slight contraction of the Cu-Fe distance. Based on our model from previous spectroscopic and computational studies,[170] we propose that the modestly shortened Cu-Fe distances in **1b** and **1d** result from enhanced donation in the Fe$\rightarrow$Cu dative bond. No significant deviations in C$_{NHC}$–Cu–Fe angle were observed, indicating that a single phosphine ligand does not provide sufficient steric pressure to strain the metal-metal bond.
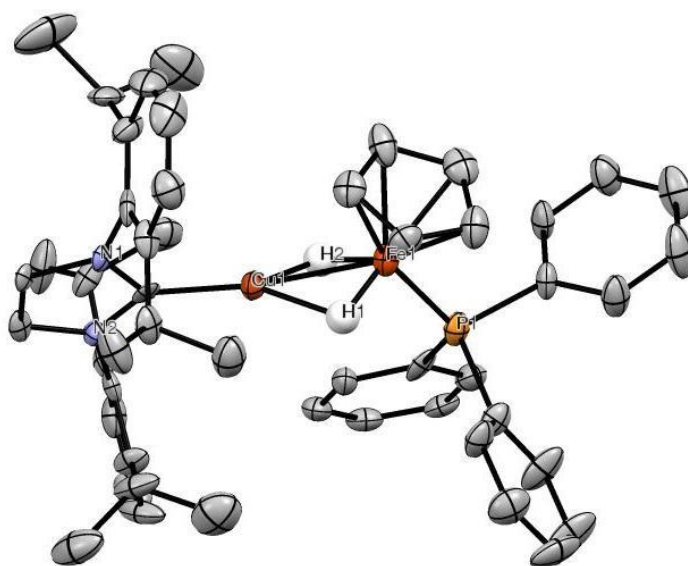


**Figure 3-2.** X-ray crystal structure of **2** with ellipsoids shown at the 50% probability level. C-H hydrogens are omitted. H1 and H2 were located in the Fourier difference map and

refined isotropically. Selected distances (Å): Cu1-Fe1, 2.3652(16); Cu1-H1, 1.76(5); Cu1-H2, 1.68(4); Fe1-H1, 1.39(6); Fe1-H2, 1.70(6); H1-H2, 2.0(1).

When our synthetic method was used to target (IPr)Cu-FeCp(CO)(PPh$_3$) (**1e**), we did observe a ^{31}P NMR resonance at 89.6 ppm, consistent with initial formation of **1e** by comparison to analogs **1a-d**. However, **1e** appears to be unstable. When we tried to recrystallize **1e**, we only obtained a small amount of crystals of a decomposition product, whose ^{31}P NMR signal was shifted to 94.7 ppm and which was identified as (IPr)Cu(μ-H)$_2$FeCp(PPh$_3$) (**2**, Figure 3-2) by X-ray crystallography. We have been unable to synthesize **2** independently or isolate it in large enough quantities for full characterization and reactivity studies. We assume that source of hydrogen during decomposition is the side-product contaminant CpFe(IPr)(CO)H, which was observed in the crude mixture by ^{1}H NMR. A related complex LCu(μ$_2$-H)$_2$WCp$_2$ (L = β-diketiminate) was reported recently by Crimmin, who formulated its bonding as consisting of a σ-adduct of H$_2$WCp$_2$ bound to [LCu] through $\eta^2$:$\eta^2$-binding of two W-H σ-bonds to Cu(I).[171] By analogy, one view of **2** is as a $\eta^2$:$\eta^2$-adduct of anionic [H$_2$FeCp(PPh$_3$)]$^-$ to cationic [(IPr)Cu]$^+$. However, we cannot rule out an alternative representation of heterodinuclear **2** as the $\eta^2$-adduct of neutral [HFeCp(PPh$_3$)] bound to neutral [(IPr)CuH]. The H···H distance in **2** of 2.0(1) Å is clearly too long to invoke any dihydrogen interaction.[172][173]

Related chemistry is available for the tungsten analogs. Slow dihydrogen evolution occurred from the reaction of WCp*(CO)$_2$(PR$_3$)H complexes with either (IPr)CuH or (6Pr)CuH (6Pr = *N,N'*-bis(2,6-diisopropylphenyl)-4,5,6,7-tetrahydro-1,3-diazepin-2-ylidene), providing heterobimetallic (NHC)Cu-WCp*(CO)$_2$(PR$_3$) complexes in 15-66%

yield (**3a-d**, Scheme 3-3). The observed reactivity is consistent with the estimated p$K_a^{THF}$

values of 14 for WCp*(CO)$_2$(PR$_3$)H.[174] These complexes were characterized by

multinuclear NMR spectroscopy and FT-IR spectroscopy, and derivatives **3b-d** were

characterized by X-ray crystallography. Relevant data is shown in Table II for comparison

to (IPr)Cu-WCp(CO)$_3$, and solid-state structures for **3b-c** are depicted in Figure 3-3.

Unlike iron analogs **1a-d**, the tungsten complexes **3a-d** are quite robust thermally and do

not decompose upon prolonged heating at 67°C.
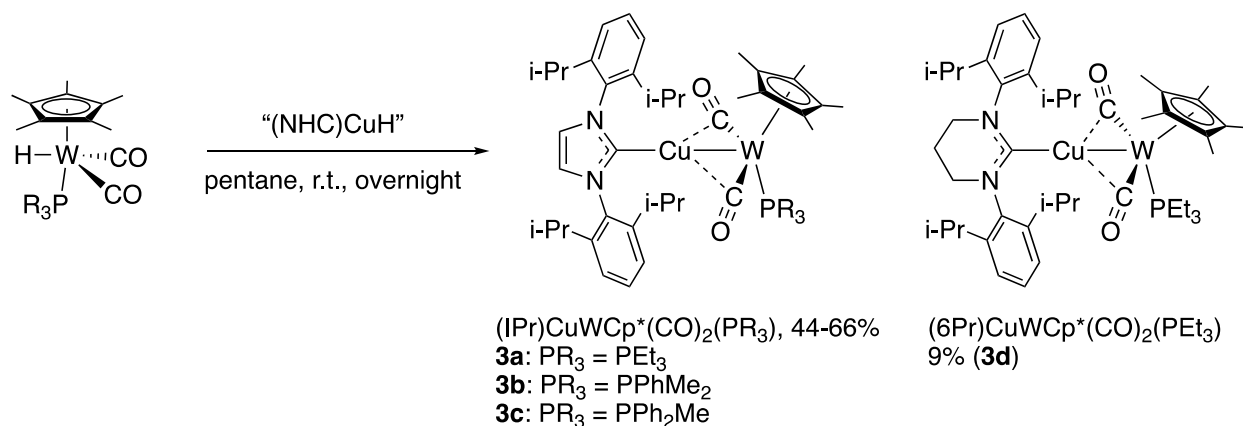


**Scheme 3-3.** Synthesis of mixed phosphine/carbonyl Cu-W heterobimetallic complexes.
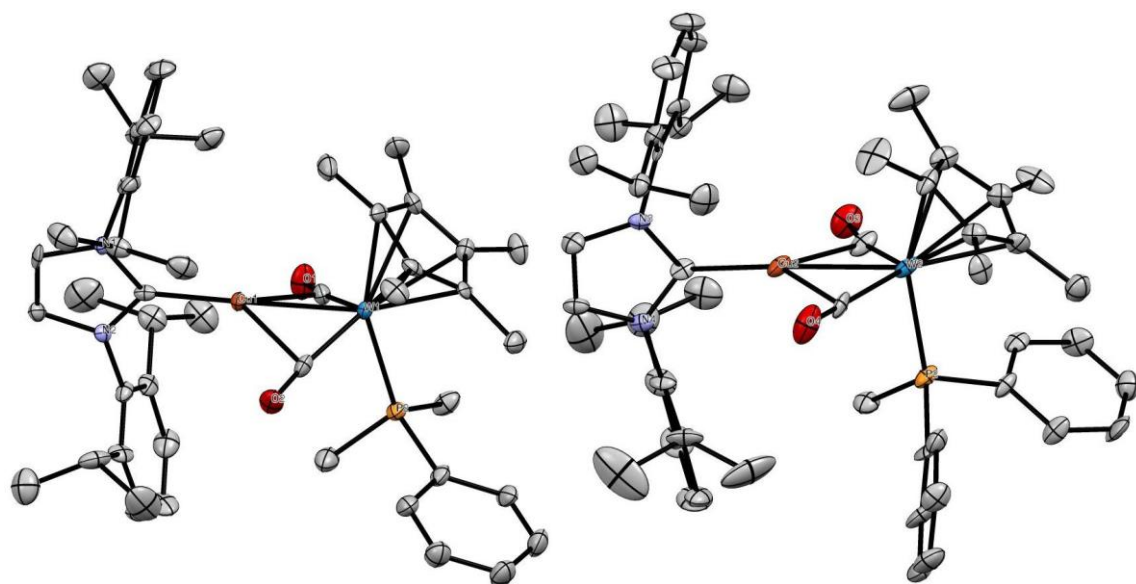
**Figure 3-3.** X-ray crystal structures of **3b** and **3c**, with ellipsoids shown at the 50% probability level. Hydrogen atoms have been omitted, and only one of two independent molecules in the asymmetric unit of **3c** is shown. Selected bond metrics are given in Table II.

**Table II.** Selected data comparisons for Cu-W heterobimetallic complexes

| Complex | $\nu_{CO}$ (cm$^{-1}$) | $d$(Cu-W) (Å) / FSR$^a$ | $d$(Cu$\cdots$CO) (Å) | $d$(C-O) (Å) | $\angle$C$_{NHC}$-Cu-W (°) | $\angle$W-C-O (°) |
|---|---|---|---|---|---|---|
| (IPr)Cu-WCp(CO)$_3$$^{b,c}$ | 1920, 1818, 1784 | 2.5599(6) / 1.035 | 2.294(7), 2.280(5), 3.858(6) | 1.174(8), 1.16(1), 1.159(7) | 165.7(1) | 173.5(5) |
| (IPr)Cu-WCp*(CO)$_2$(PEt$_3$) (**3a**) | 1750, 1691 | n.d.$^d$ | n.d.$^d$ | n.d.$^d$ | n.d.$^d$ | n.d.$^d$ |

| | | | | | | |
|---|---|---|---|---|---|---|
| (IPr)Cu-WCp*(CO)$_2$(PPhMe$_2$) (3b) | 1778, 1702 | 2.5490(8) / 1.031 | 2.205(2), 2.227(2) | 1.197(2), 1.204(2) | 178.02(5) | 171.6(1), 172.1(1) |
| (IPr)Cu-WCp*(CO)$_2$(PPh$_2$Me) (3c)[c] | 1762, 1693 | 2.579(1) / 1.043 | 2.15(1), 2.18(1) | 1.17(2), 1.19(2) | 178.8(3) | 167.6(9), 168(1) |
| (6Pr)Cu-WCp*(CO)$_2$(PEt$_3$) (3d) | 1753, 1688 | 2.6137(5) / 1.057 | 2.2022(7), 2.2143(7) | 1.1801(7), 1.1849(8) | 177.37(3) | 168.58(5), 170.60(5) |

[a]FSR = formal shortness ratio.[167] [b]Data from literature references.[52] [c]Structural data is given for one of two independent molecules in the asymmetric units of (IPr)CuWCp(CO)$_3$ and 3c. [d]n.d. = not determined.

The overall trends for the Cu-W series are similar to those noted above for the Cu-Fe series. The W center is, as expected, more electron-rich upon phosphine ligation in 3a-d, whose carbonyl stretching frequencies are shifted to lower energies from the corresponding features in (IPr)Cu-WCp(CO)$_3$ (Table II). Both 3b and 3d feature a pair of semibridging carbonyl ligands according to their α parameters of ~0.13-0.15. Complex 3c has one semibridging carbonyl ligand (α = 0.14) and one carbonyl ligand that borders on fully bridging (α = 0.10). The metal-metal bonding appears not to be impacted significantly by phosphine ligation, as the Cu-W distances in 3b-d are all very similar to that of (IPr)Cu-WCp(CO)$_3$, with no clear trend emerging. This observation is consistent with greater delocalization of extra electron density at W into *two* carbonyls rather than one for Fe, thus providing very little available electron density for increased donation in the W→Cu

dative bond. Once again, no evidence for steric pressure is observed structurally, as the $C_{NHC}$-Cu-W angles remain linear regardless of the ligands bound to W.

Due to their higher thermal stability the copper-tungsten complexes were pursued for C-H borylation catalysis in favor of the copper-iron analogs. Under UV irradiation conditions, complexes **3b-d** exhibited some activity for catalyzing borylation of benzene-$d_6$ solvent with pinacolborane (HBpin). However, the photochemical activity for **3b-d** was very poor (e.g., 27% conversion to $C_6D_5Bpin$ with 20 mol% **3c** under UV irradiation with 450-W Hg lamp over 24 h at room temperature) compared to that observed for the parent (IPr)CuWCp*$(CO)_3$ (80% conversion to $C_6D_5Bpin$ under identical conditions with 10 mol% (IPr)CuWCp*).[165] Even the modest photochemical C-H borylation activity with the mixed phosphine/carbonyl catalysts indicates that they are capable of performing the thermal B-H cleavage and H-H elimination reactions required for catalysis (Scheme 3-1, steps i and iii), and also that they furnish WCp*$(CO)_2(PR_3)$Bpin intermediates that are active for arene borylation when provided enough energy to induce ligand dissociation. Unfortunately, under UV-free conditions, no evidence for any catalytic activity was observed for borylation of arene solvents at temperatures up to 110°C. While disappointing, this lack of thermally-induced catalytic activity is consistent with the structural data discussed above. Specifically, the putative WCp*$(CO)_2(PR_3)$Bpin intermediates accessed from catalysts **3b-d** are presumably not sterically crowded enough for the phosphine ligand to be labile, and so the C-H functionalization step (Scheme 3-1, step ii) is inhibited. Attempts at synthesizing bulkier catalysts such as (IPr)Cu-WCp*$(CO)_2(PPh_3)$ and (IPr)Cu-WCp*$(CO)_2(PCy_3)$ failed, possibly due to instability imparted by overcrowding.

## 3.3 Conclusions

In conclusion, complexes with mixed phosphine/carbonyl ligation provide metal-hydride intermediates with sufficiently low $pK_a$ values that they are capable of engaging in heterobimetallic $H_2$ evolution with a hydridic (NHC)CuH partner. Using this $H_2$ evolution reaction as a synthetic method, several (NHC)Cu-FeCp(CO)(PR$_3$) and (NHC)Cu-WCp*(CO)$_2$(PR$_3$) complexes were synthesized and thoroughly characterized. In one case, a (NHC)Cu-FeCp(PPh$_3$) complex was found to decay to yield an interesting (NHC)Cu($\mu_2$-H)$_2$FeCp(PPh$_3$) decomposition product. While the new copper-tungsten heterobimetallic complexes are active for photochemical C-H borylation, further work is needed to identify complexes with the right steric/electronic balance for thermally-induced catalysis.

# 4 Detection of a ligand redistribution process for hydrocarbon-soluble Mg{Al[OC(Ph)(CF$_3$)$_2$]$_4$}$_2$: evidence of a "hidden equilibrium" in polyfluorinated alkoxyaluminate chemistry

## 4.1 Introduction

The current state of energy delivery has made leaps in recent decades toward emission-free transportation due to increasingly portable, renewable, and cost-effective energy storage technologies. As population rises, so does the movement toward electric vehicle use and wind or solar energy production. Renewable energy technologies such as solar and wind face issues with intermittency: times of peak production do not align with times of peak demand[63]. This creates a challenge that can be met by advancing energy storage technologies. In particular, the prospect of meeting these challenges efficiently lies in technology beyond current lithium-ion batteries. Theoretic capacities of lithium-ion batteries are projected to plateau soon, and other alkali earth metals are the focus of research efforts towards the storage technologies of tomorrow[64].

Obstacles facing lithium-ion batteries (LIB) include dependence on limited resources. Lithium is mainly mined from salt flats in a few areas of the world. Over four years up to 2014, lithium has seen an increase of 73% in consumption and 28% growth of production[175]. Cobalt, used in LIB cathodes, saw its price rise 120% in 2017. It is also mainly sourced from DRC, where ethical concerns are raised since "artisanal mining" is used[176,177]. Commercial lithium-ion batteries often cannot make use of a solid anode as the propensity of lithium to form dendrites can contribute to battery short-circuits or

separator material rupture[178]. Short circuits or exposure of internal components to the atmosphere poses risks of gas produced in a closed system or uncontrollable fires.

Magnesium has gained research popularity for its combination of earth-abundance, multivalent nature, and safety advantages. Its high theoretical volumetric energy density of 3832 mAh cm$^{-3}$, low redox potential (-2.356 vs. SHE), and similar ionic radius provide an alternative to lithium intercalation technology[179–181]. Although sensitive to small amounts of water, magnesium rarely forms dendrites and is safe to handle in open air[178,182].

Unfortunately, LIB technology has not transferred well to magnesium analogs. Commonly used carbonate solvents are unstable, forming insulating solid electrolyte interfaces (SEI)[183–185]. Previously studied cathode systems for LIBs are also not compatible due to poor intercalation of highly electrostatic Mg$^{2+}$ and the possibility for other MgX$^+$ species that could be present [186,187]. What is lacking is the key to technology that pairs high performing intercalation technology and electrolyte components effectively.

To contend with or complement lithium-ion batteries in the future, work needs to be done to expand the toolbox of battery components compatible with the unique challenges of magnesium-ion technology. The available electrolytes fall within two main groups: magnesium halides[188], non-chloride weakly-coordinating anions (WCAs, e.g., alkoxyborates/-aluminates[189,190] and carboranes[191]) and strongly coordinating anions (sulfonimides[192]). Inspired by the Krossing group's WCA work[193,194], alkoxyborates and -aluminates have found recent admiration and marketability in battery research for their

stability, tunability, and steric bulk. Alkoxyaluminates constructed with 1,1,1,3,3,3-hexafluoroisopropanol have been reported to be stable to 4 V vs. Mg, and steric protection at the tertiary $C(sp^3)$-H by trifluoromethylation extends electrochemical windows by 1 V[80].

Highlighting pitfalls and understanding how to manipulate aluminate synthesis is important for the electrolyte community. This work reveals the presence of a previously undetected equilibrium between 4-coordinate alkoxyaluminate species and the neutral three-coordinate analogs used to synthesize them (Scheme 4-1). The ligand rearrangements facilitating this equilibrium have been characterized by nuclear magnetic resonance (NMR) spectroscopy, infrared (IR) spectroscopy, and single-crystal X-ray diffraction (XRD). These observations allow us to conclude that introducing too much steric bulk can impede the synthesis of alkoxyaluminates, but due to the natural equilibrium speciation of the electrolyte itself rather than to the nature of the synthesis. This equilibration is likely to be operative in other alkoxyaluminate systems, as well, but has not been documented to our knowledge. Taking this behavior into consideration will be crucial in guiding future electrolyte synthesis and optimization.



**Scheme 4-1.** Equilibrium in ligand rearrangement for Mg[Al(hPhip)₄] synthesis.

66

## 4.2   Results and Discussion

## 4.3   Synthesis and NMR analysis of Mg[Al(hPhip)₄]₂

The initial aim of our study entailed the development of an electrolyte system with abnormal solubilities. We were interested in modulating the coordination environment around the magnesium center between solvent and a weakly coordinating anion to understand and possibly optimize electrolyte behavior. We chose to use the popular and well-known magnesium alkoxyaluminate electrolyte system[83]. Based on the commonly-used hexafluoroisopropoxide ligand motif, we targeted an analog functionalized with a phenyl group at the tertiary carbon (hPhip = 1,1,1,3,3,3-hexafluoro-2-phenyl-2-propanol) to provide solubility in apolar and poorly coordinating solvents. The candidate electrolyte was synthesized by adapting a published synthesis using a rearrangement of ligands, i.e., Lewis acidic abstraction of alkoxide ligands by Al(III) from $Mg^{2+}$(Scheme 4-1)[83]. Previously, this synthetic route has provided the cleanest pathway to alkoxyaluminates while avoiding metal halide salt impurities prevalent in other methods[83].



Scheme 4-2. Initial synthetic method for Mg[Al(hPhip)₄]₂

Tricoordinate aluminum can exist as a mixture of four, five, and six-coordinate aluminum species in solution, which coalesce to a four-coordinate magnesium alkoxyaluminate when introduced to bis(alkoxy)magnesium[83]. Changes in the aluminum coordination environment are easily probed by $^{27}$Al NMR due to the characteristic peak shapes and chemical shifts associated with different geometries. Contrasting to previous work, to which all comparisons will be made unless noted[83], the modified Al(hPhip)$_3$ **(2)** shows only one $^{27}$Al NMR resonance at 31 ppm in C$_6$D$_6$, indicating speciation of only one form in benzene solution. The chemical shift at 31 ppm also indicates that the present species is likely a 3- or 4-coordinate neutral species. Higher coordinate aluminum species often show further upfield as mixtures of charged Al(III) species or accompanied by charge balancing cationic species[83,195]. When Mg(hPhip)$_2$ **(1)**, was stirred with **2** at room temperature for four days, two resonances were present at 31 and 45 ppm in C$_6$D$_6$ (Figure 4-1). This observation led us to believe one of the new signals must be the desired four-coordinate aluminum species. The presence of two resonances rather than one could have various causes. The lack of a single, narrow peak could be due to the low symmetry and steric bulk of the hexafluorophenyl isopropoxide ligands. Alternatively, the increase in steric bulk could hinder the complete conversion of the reaction to the four-coordinate aluminate, **3**.

**Figure 4-1.** $^{27}$Al NMR in C$_6$D$_6$ of **2** (blue), **3** (red), and **3** synthesized by an orthogonal method (green).

At this point, the chief aim of our study was redirected to understanding the synthesis of alkoxyaluminates with our modified ligand system. The new alkoxyaluminate reaction mixture exhibited drastically different physical properties than other metal alkoxyaluminate analogs. Tricoordinate **2**, although generally highly viscous to start, solidified to a cloudy semi-solid over time. The subsequent mixture of **3** never solidified and remained a viscous liquid at room temperature even under vacuum for 1 d. Upon heating a toluene solution of **3** to 100 °C to remove any coordinating ethereal solvents and excess H-hPhip, the mixture remained liquid and formed an amber glass-like solid when cooled. Nonetheless, the $^1$H NMR spectrum in C$_6$D$_6$ always featured signals for coordinated DME solvent.

The presence of multiple species present was corroborated by observing highly complex $^1$H and $^{19}$F NMR spectra. $^1$H and $^{19}$F NMR spectra showed small variations between **2** and **3** and a high degree of spectral overlap in chemical shift region of the ligand. Alkoxyaluminate species are known to form a variety of oligomeric complexes which can give intricate NMR spectra[83]. $^{25}$Mg NMR proved to be the least useful mode of probing ionic and solvent coordination environments. $^{25}$Mg NMR suffers from low sensitivity, taking up to 48 hours to record signal[80]. Final electrolyte mixtures were never successfully characterized by $^{25}$Mg NMR due to poor signal-to-noise ratio.

### 4.3.1  Orthogonal Synthesis of Mg[Al(hPhip)$_4$]$_2$

To verify that a four-coordinate aluminum anion was formed, an orthogonal synthesis was used to produce the same product (Scheme 4-3). Using lithium aluminum hydride as a starting point, we were able to begin with a previously installed four-coordinate aluminum center followed by the addition of the functionalized alcohol (H-hPhip) to form the LiAl(hPhip)$_4$ **(4)** by protonolysis. Unlike previous attempts, the resulting aluminate anion predominantly showed one resonance at 48 ppm in $^{27}$Al NMR, similar to **3**, which showed at 45 ppm. To rule out the presence of metal halide impurities during Li/Mg exchange, an adapted synthesis was used in which LiAl(hPhip)$_4$ was protonated to form H(OEt$_2$)$_2$Al(hPhip)$_4$ **(5)** first, and subsequently dibutyl magnesium was employed to deprotonate the intermediate and form the magnesium alkoxyaluminate **(3)** (Scheme 4-3). Yet again, the resulting $^{27}$Al NMR spectrum of **3** revealed two resonances indicating a mixture of **2** and **3,** at slightly different chemical shifts of 33 and 41 ppm in C$_6$D$_6$ (Figure 4-1) despite the fact that **2** was never involved in this synthetic route.

$$LiAlH_4 + 4\ hPhip \xrightarrow[-\ 4H_2]{pentane,\ -20^oC,\ 1d} Li\ Al(hPhip)_4$$

**4**

$$Li\ Al(hPhip)_4 + HCl:OEt2 \xrightarrow[-\ LiCl]{DCM,\ RT,\ 8h} H(OEt_2)_2 : Al(hPhip)_4$$

**5**

$$2\ H(OEt_2)_2 : Al(hPhip)_4 + Mg(Bu)_2 \xrightarrow[-\ 2\ butane]{toluene,\ RT,\ 18h} Mg[Al(hPhip)_4]_2$$

**3**
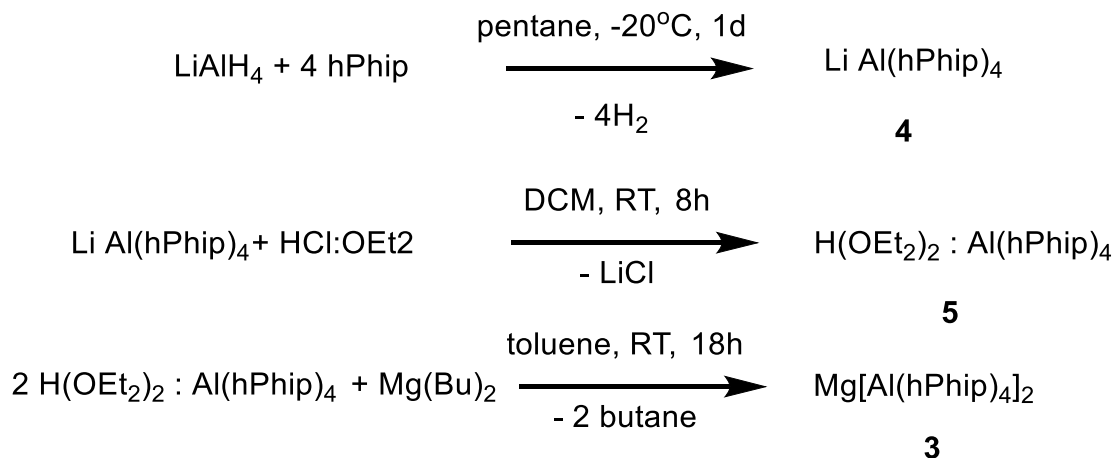
**Scheme 4-3.** Orthogonal synthetic method for $Mg[Al(hPhip)_4]_2$ with $LiAlH_4$ as a starting point

### 4.3.2 Electrolyte characteristics

While we were able to establish formation of a new magnesium alkoxyaluminate complex **3** that displays some slow equilibrium speciation of three -coordinate **2**, we were curious to compare its characteristics as an electrolyte to established magnesium alkoxyaluminate electrolytes. Conductivity of a 0.125 M solution of **3** in DME averaged 0.15 mS·cm$^{-1}$ at 25 °C, compared to the 0.25 M $Mg[Al(hfip)_4]_2$ in DME reported at 6.50 mS·cm$^{-1}$ at 25 °C[83]. This decrease in conductivity is likely due to the incomplete formation of a free divalent magnesium ion in solution due to the newly discovered equilibrium.

Simple cyclic voltammetry experiments are essential for evaluating electrolyte characteristics, like metal plating and stripping, or onset of oxidation. Despite the finding that an equilibrium exists in solutions of **3**, cyclic voltammetry revealed an electrolyte capable of magnesium deposition and dissolution regardless of its incomplete ionization

71

and poor conductivity. Onset of oxidation occurred at an approximate potential of 1.2 V vs Mg, compared to $Mg[Al(hfip)_4]_2$ (hfip = 1,1,1,3,3,3-hexafluoroisopropanol) having anodic stability of up to 3.5 V vs Mg[83]. Cyclic voltammetry indicated overpotentials of 400 mV to deposition and diminishing dissolution current with repeated cycling (Figure 4-2). Generally, the first few cycles of reversible plating and stripping may be compromised by surface passivation or the need to prime the surface to be plated, but a model electrolyte will stabilize over many cycles[196]. In this case, the diminishing current could be due to decomposition of **1** or **2** (formed from equilibrium of **3**) on the platinum working electrode, followed by formation of an insulating SEI. Even more conspicuous was the visible formation of a crystalline solid at the bottom of the electrochemical cell after cyclic voltammetry.
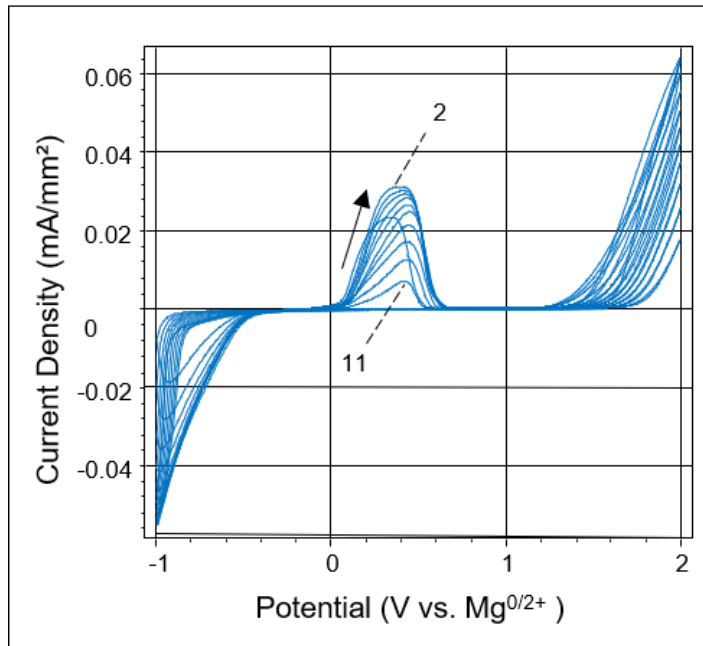
**Figure 4-2.** Voltammetric response of 0.25 M Mg[Al(hPhip)$_4$]$_2$ (**3**) in DME (scan rate = 50 mV/s, for 11 cycles). Cycles 2 and 11 are numbered to show direction of diminishing current.

### 4.3.3 X-ray Diffraction Analysis

Faced with the first crystalline solid in this system, we sought to confirm the NMR data by characterizing the various components of the electrolyte mixture that had formed during cyclic voltammetry experiments. Singe crystal X-ray diffraction of this solid showed it to be Mg(hPhip)$_2$(DME)$_2$, corresponding to **1**. (Figure 4-3a). The neutral magnesium complex possessed a standard octahedral coordination sphere in which alkoxide ligands were bound in a *cis* configuration. This information provided further evidence supporting the loss of current during deposition and dissolution in CV.

Attempts to recrystallize **1** from the reaction mixture in THF with pentane, rather than DME, provided yet another piece of the puzzle, **2**. Single-crystal XRD data showed

**2** not as a three-coordinate aluminum, or short oligomer, but as a neutral four-coordinate aluminum complex containing three alkoxide ligands and the fourth coordination site occupied by THF solvent. (Figure 4-3b)



(a)                                              (b)
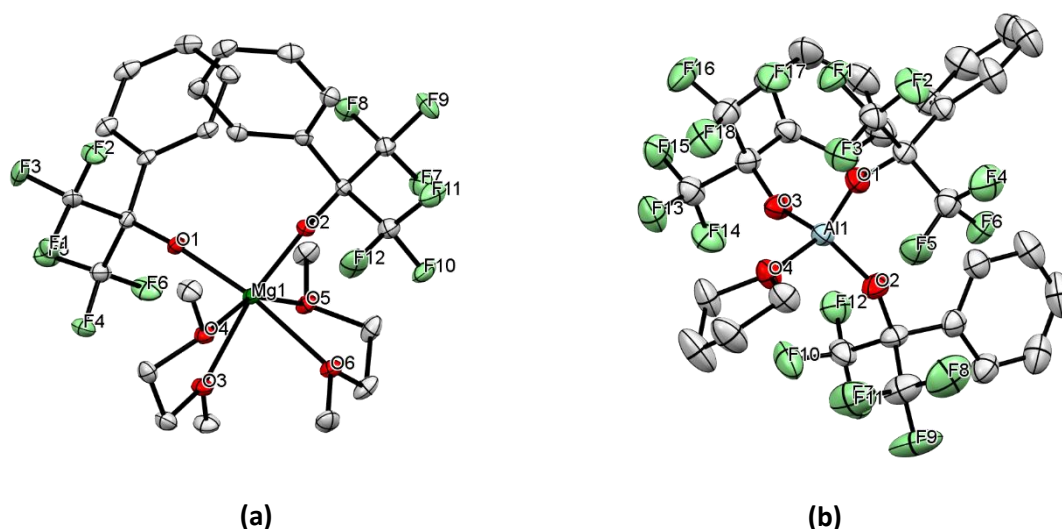
**Figure 4-3.** Molecular structures of Mg(hPhip)$_2$(DME)$_2$ (**1**) and Al(hPhip)$_3$(THF) (**2**) as ORTEP drawings with 50% probability ellipsoids. Hydrogens and non-coordinated solvent molecules were omitted for clarity.

### 4.3.4  Analysis of Equilibrium

The elusive structure of **3** led us to study the dynamics of the equilibrium between **1**, **2**, and **3**. FT-IR spectra of the mixture at various concentrations in DME showed a red shifting of corresponding C-C and C-F stretches with increasing concentration. This indicates a higher association between free magnesium cations and aluminate anions, a phenomenon described in the analogous perfluorinated system[80]. Differing from these trends was the absence of change when the electrolyte mixture was dissolved in toluene (Figure 4-4). Regardless of concentration, the spectra remained the same. Although less telling of the relationship in equilibrium, the information details the poor interaction between free Mg$^{2+}$ and aromatic solvents, preferring interaction with the aluminate anions at all concentrations in toluene.
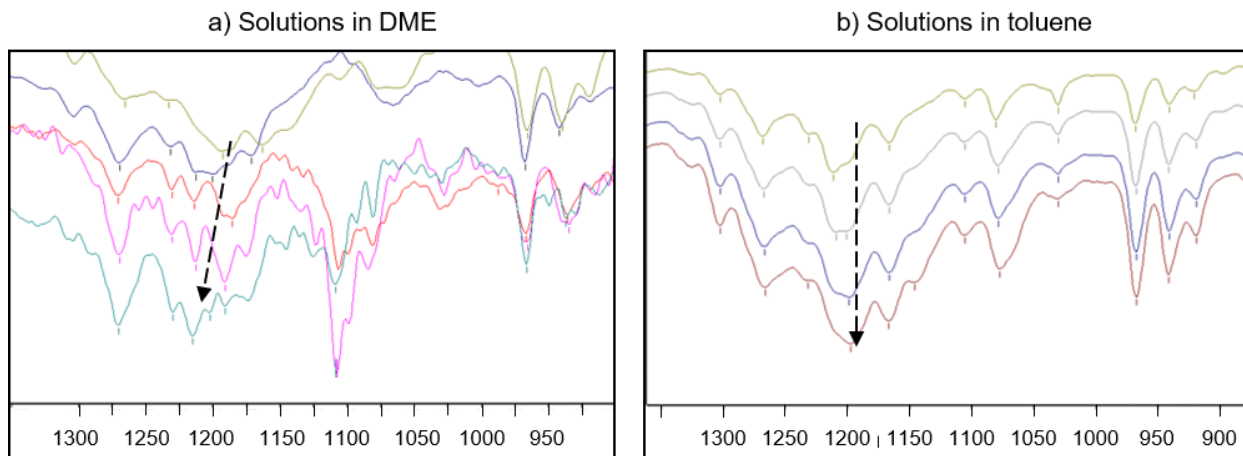
**Figure 4-4.** FT-IR spectra of Mg[Al(hPhip)$_4$]$_2$ at approximately 100, 200, 300, and 400 mM in (a) DME (spectrum of concentrated **3** in yellow added for comparison) and (b) toluene

$^{27}$Al NMR data of increasingly dilute solutions in DME and C$_6$D$_6$ revealed a minute trend toward an increase in **3** with increasing concentration. Due to the poor signal-to-noise ratios and background signals at different concentrations, we sought to provide further evidence of this relationship by other means. Variable temperature NMR (VT-NMR) is commonly used to study shifts in dynamic equilibria as a result of temperature. $^{27}$Al NMR spectra at different temperatures of the electrolyte mixture in diglyme provided no trend in the ratio of peak integration from **2** to **3**. With an increase in temperature, only peak widths and spectral baselines changed, which can be explained by the added energy for rotation of ligands that provides higher symmetry around Al(III).

Since the initial synthetic rearrangement requires four days (Scheme 4-2), if an equilibrium is present, it must be slow to establish itself. The next logical step was to analyze several samples of 0.2 M electrolyte mixture in diglyme held at temperatures of 80, 100, and 120°C, allowing the shift in equilibrium to occur over longer periods of time

(Figure 4-5, Table III). From room temperature (23°C) to 100 °C, an increase in **3:2** was observed after 2 d, with a significant drop in ratio at 120 °C. After four days, an increase in **3:2** was observed only for the sample at 80 °C, and a decrease was observed at 100 °C and 120 °C. After a week of heating, the samples were left to cool to room temperature for four days. The ratio for the sample at 80°C returned roughly to that of the two-day mark, proving that the interconversion of **2** and **3** is reversible but slow. The observed decrease in **3:2** at 100 °C over 4 days and 120 °C only after two days was accompanied by a color change of yellow to cloudy dark brown. This indicates decomposition of a component in the equilibrium, likely **3**, at higher temperatures.
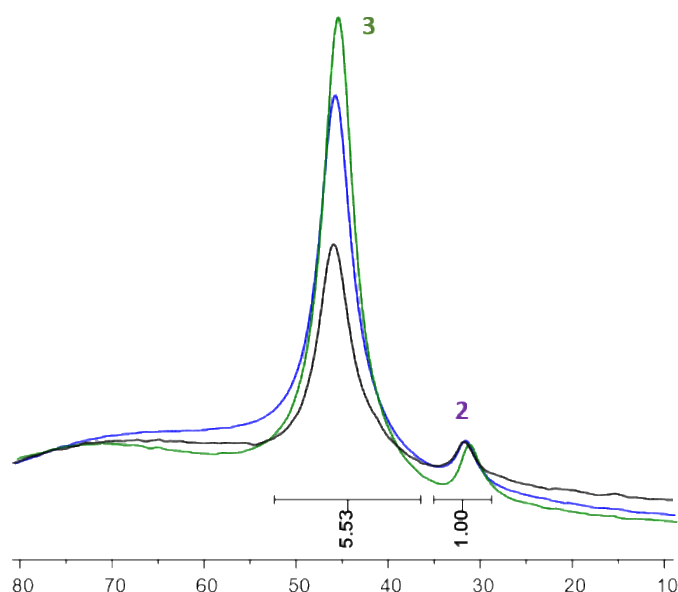


**Figure 4-5.** Example spectrum ($^{27}$Al NMR in G2): Electrolyte mixture at 80 °C for 2 days (blue), 4 days (red), 1 week (green), and then cooled to room temperature 4 days after heating (black)

**Table III.** Temperature dependence of **3:2** ratio[a]

| Temperature | Ratio at 2 d | Ratio at 4 d | Ratio at 7 d | Ratio after cooling[b] |
|---|---|---|---|---|
| r.t. | 5.1 | 5.1 | 5.1 | 5.1 |
| 80 °C | 5.8 | 7.9 | 9.7 | 5.5 |
| 100 °C | 6.5 | 4.4 | 3.2 | 2.8 |
| 120 °C | 1.2 | 0.9 | 0.7 | 0.5 |

[a]Ratios determined by $^{27}$Al NMR integration of 0.2 M solutions in diglyme. [b]Samples were allowed to equilibrate at room temperature for 4 d after being heated to the indicated temperature for 7 d.

## 4.4 Conclusions

Herein, we have synthesized an analog of the widely used magnesium alkoxyaluminate electrolyte system, replacing 1,1,1,3,3,3-hexafluoroisopropanol with 1,1,1,3,3,3-hexafluorophenylisopropanol. Despite its underwhelming electrochemical performance, the new derivative served as a platform to better understand some intricacies of magnesium alkoxyaluminates. Common issues with electrolyte syntheses are the minute salt impurities that may greatly affect performance[197,198]. Using a ligand rearrangement synthesis remains a good solution to avoid salt impurities and reveals the opportunity to observe the effects of ligand sterics on aluminate formation. According to our studies, the weakly coordinating alkoxyaluminates on which so many electrolytes are based exhibit a hidden equilibrium that may present issues for divalent battery systems moving forward by facilitating decomposition during battery cycling. It has been known that the electron-withdrawing nature of the ligand used plays an important role in anodic stabilities of electrolytes[82]. Previously, increased steric bulk and evading β-hydride elimination by functionalization were hypothesized to improve anodic stability. This work shows a limit to sterics that may inadvertently work against the production of aluminate

anions and create an equilibrium between neutral Al(III) species and aluminate salt. The implications for future work could help play a part in understanding other multivalent systems and ligand affinity for bisalkoxy-metal starting material, like **1**, or the free cationic metal aluminate species favored for electrolytes (**3**). Understanding these processes may also provide insight into possible decomposition pathways for these alkoxyaluminate based electrolytes in practice. Future efforts can then be directed toward characterizing products of less stable species during electrochemical experiments to better inform syntheses toward tailoring electrolytes for multivalent ion batteries.

## 5   Mechanistic Insights in Quinone-Based Zinc Batteries with Nonaqueous Electrolytes

### 5.1   Introduction

Nonaqueous multivalent batteries have emerged as promising "beyond Li-ion battery" technologies owing to their higher theoretical volumetric capacity and minimal dendrite formation compared to lithium metal anodes. Out of the available multivalent systems, those based on earth-abundant elements such as $Mg^{2+}$, $Ca^{2+}$, $Zn^{2+}$, and $Al^{3+}$ attract most of the interest. Particularly, $Zn^{2+}$ systems display high efficiency of deposition, safety, and nontoxicity. For instance, a recent account by Zheng *et al.* reported a reversible epitaxial electrodeposition of zinc with a Coulombic efficiency of 99.9% for over 10000 cycles in a nonaqueous electrolyte.[199] However, several challenges remain in the advancement of multivalent ion batteries, including the development of both a cathode and an electrolyte that each show fast/facile intercalation and electrochemical stability while being stable toward the anode. With the high atomic mass and strong positive polarity, $Zn^{2+}$ tends to show sluggish intercalation kinetics of ion transport in the traditional transition metal oxide cathodes.[200]

Regarding the history of Zn batteries development, some research efforts, including the nascent work on nonaqueous rechargeable Zn batteries, were summarized in Table IV. Notably, the non-rechargeable Leclanché cells (Zinc-carbon cells with $MnO_2$) were successfully commercialized and were prevalent in the early 20<sup>th</sup> century.[201] The research on rechargeable Zn air batteries took off in the last few years.[202–210] Cathode materials that are compatible with $Zn^{2+}$ mostly consist of transition metal oxides with

layered structures such as manganese oxides and vanadium oxides,[211–215] with additional examples of graphite,[216] Prussian blue analogs,[217] Chevrel phase materials,[218] and organic and polyorganic compounds.[219] The Nazar group noticed a dramatic difference in both capacity retention and battery cycle life between aqueous electrolyte (zinc sulfate) and nonaqueous electrolyte (zinc triflate in acetonitrile), using the same layered structured materials $V_3O_7.H_2O$ (an intermediate phase between $VO_2$ and $V_2O_5$) as cathodes. The $Zn-V_3O_7$ battery can cycle with a fast rate (up to 8 C) and a high specific capacity in an aqueous zinc sulfate solution. In contrast, in the nonaqueous zinc triflate acetonitrile solutions, the capacity plummeted even under a slow rate of C/75.[212] These previous studies concluded that, despite the small radius of $Zn^{2+}$(0.75Å), difficult intercalation is observed originating from strong electrostatic interaction between the crystal lattice of the inorganic host and the divalent zinc ions. Further expansion to current intercalation cathode materials is needed with sufficient compatibility for multivalent systems.

**Table IV.** A comparison of the Zn ion batteries (primary and secondary) in aqueous and nonaqueous electrolytes. ([a]Type = battery type where P = primary cell, F = flow cell, R = rechargeable)

| Cathode | Electrolyte | Average charge Voltage (V) | Discharge Capacity (mAh/g) | Discharge Rate | Type[a] | Capacity Retention | Ref |
|---|---|---|---|---|---|---|---|
| $MnO_2$<br><br>(2 $MnO_2$ + 2 $NH_4Cl$ + $H_2O$ + 2e- → $Mn_2O_3$ + 2 $NH_4OH$ + 2 $Cl^-$) | $ZnCl_2$/$NH_4Cl$ /$H_2O$ | 1.4 | 616 | N/A | P | N/A | 3 |
| $Br_2$ | $ZnBr_2$/$H^+$ | 1.8 | 430 Wh/kg | N/A | F | N/A | 43 |
| $O_2$ | KOH/$NH_4Cl$ | 1.5 | 1084 Wh/kg | N/A | P | N/A | 4 |
| $O_2$ | RTIL | 1.65 | 1166-1431 Wh/kg | N/A | R | N/A | 5-7 |
| $Mo_6S_8$ (nanocube) | 1.0 M $ZnSO_4$ | 0.4, 0.6 | 90 for 1st Cycle | 0.1 - 1 C | R | 65 at 150 cycles | 20 |
| | 1.0 M $Zn(ClO_4)_2$ in MeCN | 0.4, 0.6 | 90 for 1st Cycle | | R | 65 at 150 cycles | |
| $Zn_xMo_{2.5+y}VO_{9+z}$ | 0.2 M $Zn(CF_3SO_3)_2$ in PC/DMSO | ~ 0.8 | 200-220 | | R | 30 cycles | 44 |
| | 0.5 $Zn(CH_3COO)_2$ | | 180 | | R | 30 cycles | |
| Bilayer-$V_2O_5$ | 0.5 M $Zn(TFSI)_2$ in MeCN | 1.0 | 200 | 0.1 C - 20 C | R | 120 cycles | 45 |
| $V_3O_7$•$H_2O$ | 1M $ZnSO_4$/$H_2O$ 0.25 M $Zn(CF_3SO_3)_2$ in MeCN | | 275-375<br><br>65 | 1 C - 8 C<br><br>C/75 | R | 200 cycles | 14 |
| $ZnNi_xMn_xCo_{2–2x}O_4$ | 0.3 M $Zn(CF_3SO_3)_2$ in MeCN | ~ 1.2 | ~ 174 | 0.1 C - 10 C | R | 200 cycles | 46 |
| $Zn_3[Fe(CN)_6]_2$ | 1 M $ZnSO_4$ | 1.7 | ~ 60 | 1 C - 20 C | R | | 19 |
| α-$MnO_2$ | 0.1 M $Zn(NO_3)_2$ in $H_2O$ | 1.5 | 150 | 2 C | R | 50 cycles | 47 |
| PANI | 0.3 M $Zn(TFSI)_2$ in PC | 0.8 | 148 | 0.5 C | R | 2000 cycles | 48 |

Herein, we provide mechanistic insight into quinone-based zinc ion batteries with nonaqueous electrolytes. Instead of the previously used inorganic cathodes listed in

Table IV, we adopted an organic and polymeric cathode platform with the advantageous characteristic of synthetic tunability.[86,220] By employing 2,5-dimethoxybenzoquinone (DMBQ), a small redox-active molecule, and its polymeric derivatives polyanthraquinone sulfide (PAQS) and 1-4-polyanthraquinone (14PAQ) as the organic cathodes, facile reversible Zn intercalation was observed in nonaqueous Zn batteries. We refined the electrolyte and electrode choices by a series of electrochemical tests and post-mortem analyses such as X-ray diffraction (XRD) and SEM/Energy Dispersive Spectroscopy (EDS). The relationship between the electrochemical performance and its operating mechanisms is also discussed.

## 5.2 Results and Discussion

Commonly used organic electrodes for rechargeable batteries include quinones, imides, TEMPO ((2,2,6,6-tetramethylpiperidin-1-yl)oxidanyl), and polysulfide materials.[221] Quinone type cathodes have two carbonyl groups that can undergo one or two reversible electron transfers during intercalation and deintercalation. Depending on the composition and molecular weight, different specific capacities can be obtained. We chose the simple DMBQ, 14PAQ, and PAQS as molecules to test Zn ion batteries. A quinone motif such as DMBQ can sequentially accept 2 electrons to form $[DMBQ]^{2-}$ with a theoretical capacity at cells with an average discharge voltage of 2.0 V vs. $Mg/Mg^{2+}$, which is translated to a voltage of 0.4 V vs. $Zn/Zn^{2+}$. (Figure 5-1) [86,220] In terms of zinc batteries, the loss of the energy density by changing the anode from Mg to Zn is compensated when paired with organic electrodes characterized by high volumetric density (5854 $mAh/cm^3$), low cost of the Zn metal ($0.9/lb), and crustal abundance.

Judging from previous examples, the average voltage of Zn ion batteries is generally low, at ~ 1.0 V.
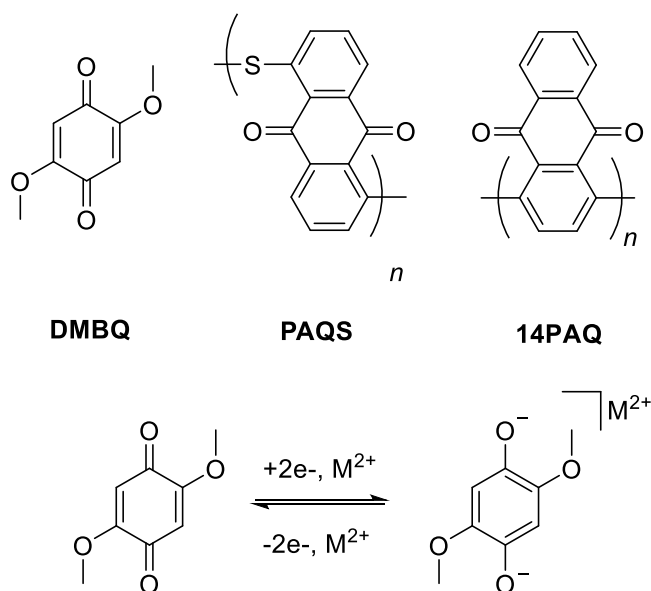


**Figure 5-1.** Molecular structures of the organic cathodes in Zn ion batteries and their acronyms, and redox reactions of DMBQ.

## 5.2.1 Effect of solvents

The electrochemical and transport properties of nonaqueous Zn electrolytes have been extensively studied through a combination of molecular dynamics simulations and electrochemical measurements using the Cottrell Equation.[197] Zn(TFSI)$_2$ was selected as the salt testing vehicle because it can be obtained commercially with high purity, precluding the artifacts that are caused by 1-5 wt% impurity that commonly exist in salts. The Zn(TFSI)$_2$ salt also has a high electrochemical stability at up to 3.8 V vs. Zn/Zn$^{2+}$ in both polar and nonpolar solvents. The O-containing and electron-donating solvents tested were dimethylformamide (DMF), propylene carbonate (PC), and diglyme (G2), as well as the N-containing electron-donating acetonitrile (MeCN). (Figure 5-2) Zn(TFSI)$_2$ in these solvents displayed a reversible Zn deposition/dissolution with a >3.4 V electrochemical

stability. Among the solvents tested, MeCN showed the best performance in regard to Coulombic efficiency (99%) and stability (3.8 V vs. $Zn/Zn^{2+}$). It is interesting to note that MeCN has been computationally demonstrated to easily form aggregates due to its weakly coordinating ability and low viscosity. The weaker coordination of MeCN with $Zn^{2+}$ and $TFSI^-$ ions would result in faster dynamics of both cation and anion.[197] The low partial charge of $TFSI^-$ also renders the exceptional ionic conductivity of $Zn(TFSI)_2$ in MeCN. On the other hand, the O-containing solvent G2 is a chelating solvent, and has a relatively high viscosity. In terms of their diffusion coefficient, the $Zn(TFSI)_2$/MeCN exhibited superior transport properties (D = 8.6 x 10 $^{-5}$ $cm^2/s$ ) than G2 (D = 2 x 10 $^{-5}$ $cm^2/s$).[197] Therefore, we picked the comparison between the two solvents MeCN and G2 to delegate the effect of solvent on the organic Zn cells in this study.



**DMF**          **PC**          **G2**          **MeCN**
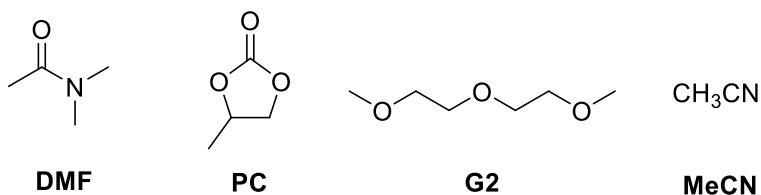
**Figure 5-2.** Molecular Structures of dimethylformamide (DMF), propylene carbonate (PC) and diglyme (G2) and acetonitrile (MeCN).

A previous study reported that two nonaqueous Zn electrolytes, namely 0.5 M $Zn(TFSI)_2$ in acetonitrile (0.5 M $Zn(TFSI)_2$/MeCN) and 0.5 M $Zn(TFSI)_2$ in diglyme (0.5 M $Zn(TFSI)_2$/G2), exhibited a highly reversible Zn plating/stripping behavior with a high Coulombic efficiency of > 99% towards an inert Pt surface. It also suggested that the surface chemistry and morphology of a working electrode changed the stability of the electrolyte.[197] Graphite foil was shown to possess extensive stability towards multivalent ion electrolytes in previous tests,[222] so it was adopted as the current collector for the

DMBQ cathode in this work. The electrochemical window of the Zn ion electrolyte is determined by both the anion species and the solvent. Presumably, the low anodic stability of electron-rich diglyme in 0.5 M $Zn(TFSI)_2$/G2 renders the anodic stability of ~ 2.5 V vs. $Zn/Zn^{2+}$, while 0.5 M $Zn(TFSI)_2$/MeCN exhibit an anodic stability window of 3.6 V vs. $Zn/Zn^{2+}$).[197] As the general discharge potential of a Zn ion battery is lower than 1.5 V, even taking an overpotential of 1 V into account, both electrolytes of 0.5 M $Zn(TFSI)_2$ in acetonitrile and 0.5 M $Zn(TFSI)_2$ in diglyme should exceed the stability window required to carry out the galvanostatic test in a DMBQ-Zn cell.

The cycling performance of DMBQ-Zn cells showed a tremendous dependence on the nature of the electrolytes: a significantly higher specific capacity is observed in the well-solvated $Zn(TFSI)_2$/MeCN electrolyte, whereas zero or less than 5 mAh/g specific capacity was retained in the $Zn(TFSI)_2$/G2 cells in over 100 cycles. The DMBQ-Zn with $Zn(TFSI)_2$/MeCN exhibited a close-to-theoretical discharge capacity of 302.6 mAh/g at the first cycle, a phenomenon originated from good solvation of $Zn(TFSI)_2$ and the well-behaved redox properties of DMBQ (Figure 5-3)**.** However, the discharge capacity dropped dramatically after the first cycle, and remained at ~ 25 mAh/g after the 15th cycle. The main reason for the diminishing cycling performance is the dissolution of the active material DMBQ. Once DMBQ accepts one or two electrons, the subsequent radical anions of $DMBQ^{-}$ and $DMBQ^{2-}$ have a higher solubility than the neutral compounds, and severe dissolution causes loss of active materials.[86,223] One way to mitigate dissolution is to covalently link the active unit of benzoquinones, which is discussed in the next paragraph. Another explanation for the cycling performance displayed is the reactivity of the $DMBQ^{-}$ and $DMBQ^{2-}$, which leads to the active materials having been consumed

rather than dissolved. These anions, especially the highly reactive radical anion, are known to participate in radical annihilations, chain propagations, and reactions with the solvent.[221,223,224] Further stabilization of DMBQ[-] can be achieved through the functionalization of the benzoquinone ring with electron-deficient groups to stabilize the half-filled or fully filled LUMO in radical anion. More research is underway and will be reported in future correspondences.
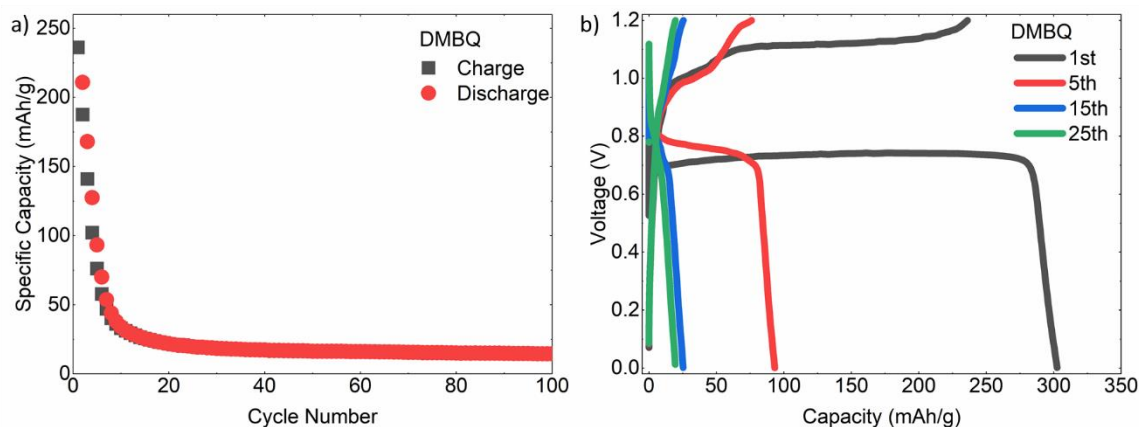


**Figure 5-3.** The cycling performance (a) and charge-discharge profile (b) of DMBQ-Zn batteries in 0.5 M Zn(TFSI)$_2$ in acetonitrile at 0.2 C.

Through the covalent bonding of the benzoquinone units, the solubility of the electron-rich radical anions can be reduced, and thus the active materials remain in contact with both the binder and the active carbon. This indeed is what we observed using polymeric PAQS and 14PAQ as active materials. (Figure 5-4) Compared to DMBQ whose capacity drops to the minimum within 15 cycles, the capacity drops gradually over the course of 100 cycles in the cases of PAQS and 14PAQ. The second cause of the DMBQ capacity fading may still be operating in PAQS and 14PAQ. An interesting observation is

that a small polarization was observed in PAQS compared with 14PAQ, which originates from the larger gap between its LUMO and HOMO in 14PAQ.
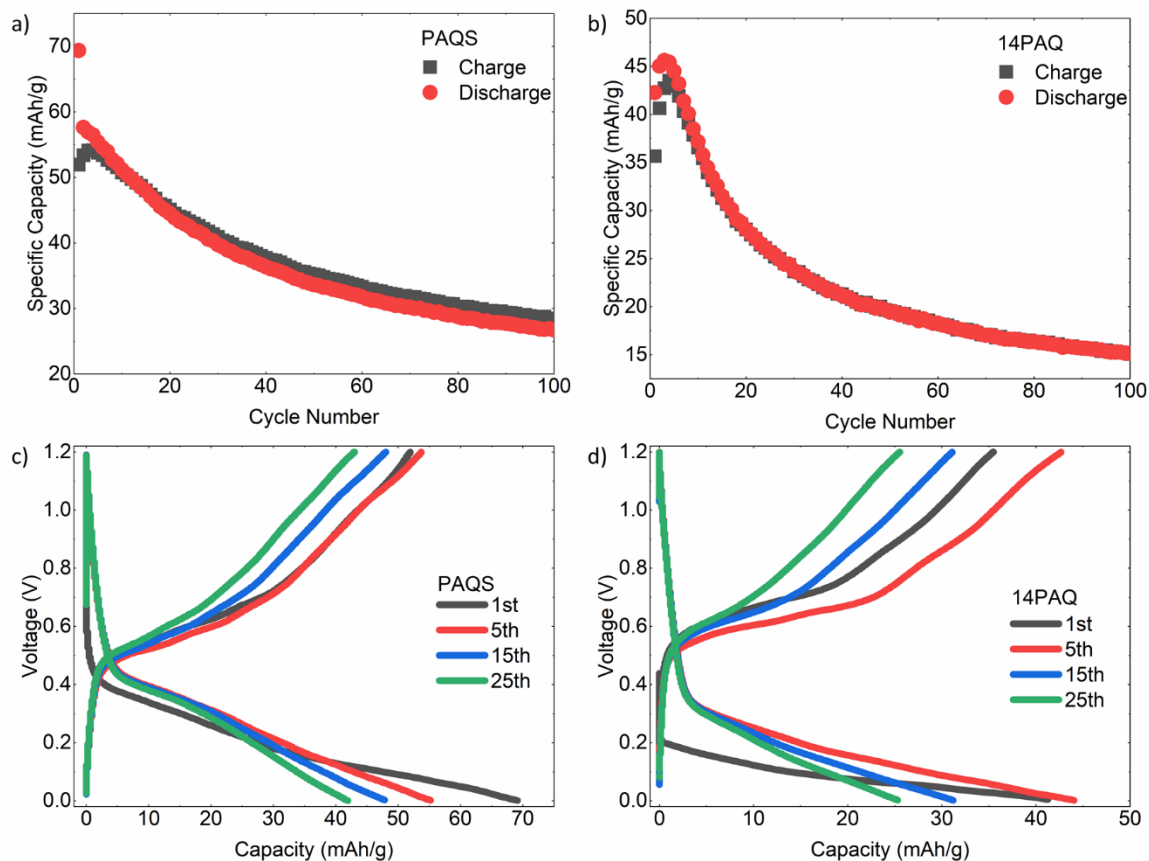


**Figure 5-4.** The cycling performance of Zn-organic electrode batteries in 0.5 M Zn(TFSI)$_2$ in acetonitrile using PAQS (a) and 14PAQ (b) as cathode at 0.2 C; The charge-discharge profile with PAQS (c) and 14PAQ(d).

To illustrate the electronic structures of these redox-active materials, we performed DFT calculations on DMBQ, PAQS, and 14PAQ. As PAQS and 14PAQ are polymeric molecules with hundreds of repeating units, the DFT calculation was simplified by calculating the repeat unit itself (PAQS_unit and 14PAQ_unit) and a selective segment with a chain length of 4 units (PAQS_4 and 14PAQ_4), respectively. The molecular

87

orbitals and the energetic levels of the LUMO and HOMO are shown in Figure 5-5. As expected, the calculated polymeric units possessed smaller band gaps than the monomeric units. The LUMO energies of the three species were very close, with PAQS (-3.2 eV) slightly higher than that of DMBQ (-3.1 eV) and 14 PAQ (-3.0 eV), suggesting similar reducing abilities of these compounds. Meanwhile, all three shared a similar shape of LUMO orbitals that were localized on the p* orbitals, consistent with their quinone-centered reduction mechanism. The experimental observation of similar discharge plateaus from the zinc batteries corroborated with these theoretical predictions.
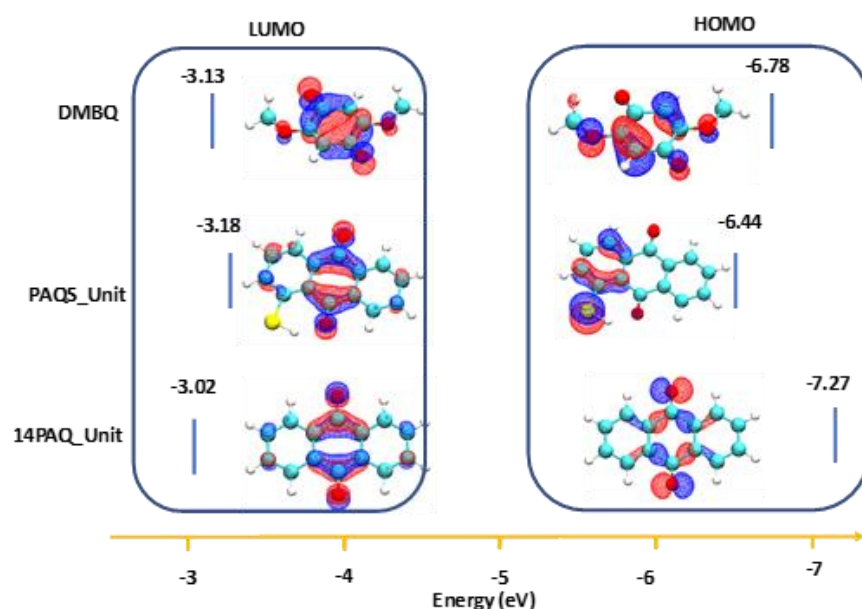


**Figure 5-5.** Frontier orbitals of DMBQ, PAQS, and 14PAQ. (Isovalue = 0.05.)

### 5.2.2 Effect of Anions and Additives

Anions exert a significant impact on the charge/discharge properties of the cathode, and numerous studies were carried out on various anion species in lithium salts before the community settled down to $LiPF_6$.[225] The performance of a certain salt in the battery environments is evaluated against various criteria. However, those criteria sometimes do not correlate. The criteria for the anion in multivalent ion batteries are typically derived from those of the lithium-ion batteries, which include solubility, ionic conductivity, interfaces with the anode, corrosion of cell components, transport properties, and electrochemical stability.[225] The two properties of most interest here are transport properties (*vide ante*) and electrochemical stability.

The TFSI$^-$ anion is known to facilitate anodic dissolution due to lack of passivation on aluminum current collector under high voltages, consequently causing a high solubility of Al decomposition products.[226] We envisioned better compatibility towards the current collector could be achieved when switching from TFSI$^-$ to $PF_6^-$. The $PF_6^-$ anion is also a weakly coordinating anion that dissociates from $Zn^{2+}$, resulting in a low tendency to form aggregates at 0.5 M concentration. The $Zn(PF_6)_2$ salt was synthesized in-house following a previous procedure reported by our group, and laborious drying and purification were performed to minimize the nuisance of impurities.[197] Unfortunately, the DMBQ-Zn performance with 0.5 M $Zn(PF_6)_2$ could not reach the upper cutoff voltage of 1.2 V, suggesting a severe side reaction with the electrolyte. We attributed the instability to the leftover impurities from the in-house synthesis.

In addition, we tested the introduction of chloride, a film-benign additive to facilitate Zn deposition/dissolution. For multivalent electrolyte research, the Cl$^-$ anion is reported to

be able to modify the surface of Mg metal and circumvent passivation when present in the Mg electrolyte.[187,227,228] Early accounts showed the addition of chloride to electrolytes based on Grignard reagents increased the anodic stability in rechargeable Mg batteries.[180,229] The Cl$^-$ anion was also reported to serve as a bridging ligand in the formation of the active dichloro Mg-depositing species, $[Mg_2\text{-}(\mu\text{-}Cl)_3]^+$.[230] Previous studies on Zn electrolytes with $ZnCl_2$ showed a similar effect of promoting the Zn deposition with a small addition of $ZnCl_2$.[231] With these precedencies in mind, a solution of $ZnTFSI_2/ZnCl_2$ in triglyme (G3) was examined as electrolytes for DMBQ-Zn batteries. Unfortunately, the inclusion of Cl$^-$ causes a detrimental effect on the cell cycling, and most of the cells could not reach the 1.2 V cutoff voltage, indicating the electrochemical instability of such an additive.

### 5.2.3   Post-mortem analyses and mechanistic insights

The reversibility of the cycling performance with organic electrodes was investigated using in-depth analytical tools, including XRD, SEM/EDS, and cyclic voltammetry (CV). Among all the electrodes, DMBQ had a distinctive charge and a discharge plateau. Advantages using DMBQ as a model system includes its crystalline lattice is with well-defined unique patterns of *hkl* layers. The *ex-situ* XRD measurement was carried out on the electrodes upon cycling. As shown in Figure 5-6a, several characteristic changes upon charging were detected compared to the pristine spectrum, including the disappearance of the strong signals at 27.1° along with a few smaller peaks at 21.1°, 15.5°, and 10.5°, and the appearance of one weak signal at 13.5° and one strong peak at 11.7°. (1$^{st}$ charge, Figure 5-6a) These changes were reversed to the same XRD

patterns as the pristine laminate in the subsequent charging process, suggesting the good reversibility of DMBQ cathode material upon cycling. (1st discharge, Figure 5-6a)
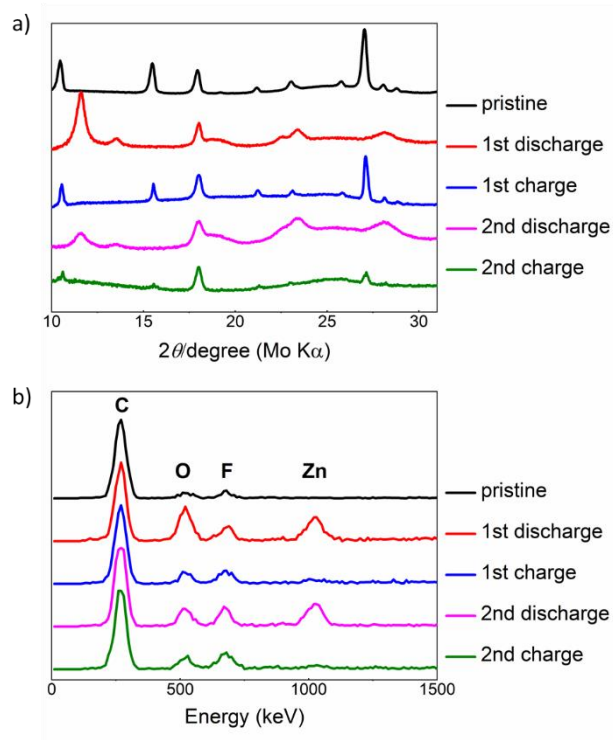


**Figure 5-6.** a) *Ex situ* XRD of the DMBQ cathode upon cycling. b) EDS spectroscopy of DMBQ cathode upon cycling, the peaks for characteristic binder energy of C, O, F and Zn were labeled.

The post-mortem surface analysis using EDS results upon cycling is shown in Figure 5-7b, and the trend upon charging and discharging was consistent with that observed by XRD. With the elements C, O, and F originating from the electrolytes of Zn(TFSI)$_2$, the amount of Zn peak reflected the intercalation of Zn$^{2+}$ into the cathode. Upon discharge, significantly more zinc content was observed at 1.0 KeV. The peak disappeared after 1st charge, indicating complete deintercalation. The process is quite reversible, as shown on the subsequent 2nd charge/discharge cycle.

91

The operating mechanism in Zn-organic batteries with nonaqueous electrolyte would shed light on its implementation for future applications. There are two mainstream mechanisms in the current energy storage systems, faradaic and capacitive.[220] One way to distinguish them is by cyclic voltammograms. A capacitor has the following distinctive features: 1) a characteristic rectangular current-voltage ($i \sim V$) curve, which indicates fast intrinsic kinetics, 2) a linear dependence of current on sweep rate ($i \alpha v^{1/2}$), and 3) the lack of distinct phase transformation in a supercapacitor. Batteries, on the other hand, typically display 1) a distinctive phase transformation indicated by a flat charge/discharge plateau, and 2) a classic semi-infinite diffusion ($i \alpha v^{1/2}$). [220] The phase transformation of the DMBQ system is evident with a discharge plateau at 0.7 V and a charge plateau at 1.12 V vs. Zn/Zn$^{2+}$. (Figure 5-7a) The CV curve also corroborated with the voltage profile with two well-separated redox peaks. (Figure 5-7b) A fitting of log($i$) versus log($v$) using the equation $i = av^{b}$ gave out the $b$ value of 0.48 at the oxidation peak of 1.13 V. In essence, the rechargeable DMBQ-Zn cell operated a faradaic mechanism with excellent rate capability.
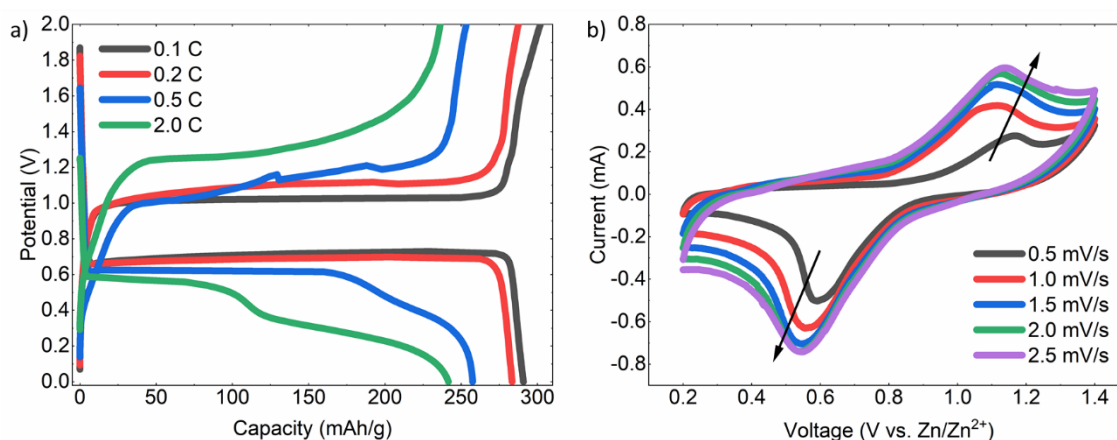


**Figure 5-7.** a) Typical charge/discharge curve for Zn-DMBQ under different rates of 0.1 C, 0.2 C, 0.5 C and 2.0 C. b) The cyclic voltammograms of Zn-DMBQ with a scan rate of 0.5, 1.0, 1.5, 2.0 and 2.5 mV/s.

The cyclic voltammograms of 14PAQ and PAQS were more complicated due to the slow charge transfer in a polymer medium and the large resistance during the galvanostatic charge. During the anodic scan, the small oxidation peak at 0.77 V indicated the onset of oxidation. Meanwhile, a hysteresis of oxidation appeared as a flat line from 0.84 to 1.4 V, which was attributed to a slow charge transfer from the current collector to infiltrate the bulk polymeric film. The same phenomenon was observed during the cathodic scan, with a small reduction peak first observed at 0.91 V, followed by a flat charge transfer plateau (0.9 to 0.2 V) due to the slow charge diffusion in polymers.

## 5.3   Conclusions

The mechanism of quinone-based organic cathodes such as DMBQ and its polymeric derivatives PAQS and 14PAQ in Zn batteries were investigated using electrochemical methods, XRD, and SEM/EDS. The intercalation of $Zn^{2+}$ into organic materials was relatively easy with fast intrinsic kinetics in nonaqueous electrolytes, which is in stark contrast to what was usually observed in transition metal oxide with $Zn^{2+}$ due to the strong electrostatic interaction between the crystal lattice of the inorganic host and the divalent $Zn^{2+}$ cation. By limiting the solubility of DMBQ through polymerization and switching to PAQS and 14PAQ cathodes, the dissolution of cathode material was mitigated. Further research on improving the specific capacity of the organic electrodes for Zn batteries is underway and will be reported in the future.

## 6 Experimental

Reproduced from:
(1) Mazzacano, T. J.; Leon, N. J.; Waldhart, G. W.; Mankad, N. P. Fundamental Organometallic Chemistry under Bimetallic Influence: Driving β-Hydride Elimination and Diverting Migratory Insertion at Cu and Ni. *Dalt. Trans.* **2017**, *46*, 5518–5521. **DOI:** 10.1039/C6DT04533B- Reproduced by permission of The Royal Society of Chemistry
(2) Reproduced from Leon, N. J.; Yu, H. C.; Mazzacano, T. J.; Mankad, N. P. Mixed Phosphine/Carbonyl Derivatives of Heterobimetallic Copper–Iron and Copper–Tungsten Catalysts. *Polyhedron* **2019**, *157*, 116–123. https://doi.org/10.1016/j.poly.2018.09.062
(3) Leon, N. J.: Mankad, N. P*.* Detection of a ligand redistribution process for hydrocarbon-soluble Mg{Al[OC(Ph)(CF$_3$)$_2$]$_4$}$_2$: evidence of a "hidden equilibrium" in polyfluorinated alkoxyaluminate chemistry. *Inorg. Chem. Submitted*
*(4)* Yang, M,; Leon, N. J.; Pan, B.; Yu, Z.; Cheng, Lei; Liao, C. 5.    Mechanistic Insights in Quinone-Based Zinc Batteries with Nonaqueous Electrolytes. *J. Electrochem. Submitted.*

## 6.1 General Considerations

All experiments were carried out in a nitrogen-filled glovebox. Reaction solvents (tetrahydrofuran, toluene, pentane, diethyl ether, acetonitrile, dimethoxyethane, and diglyme) were purchased packed under argon and stored over 3-Å molecular sieves before use or dried using a Glass Contour Solvent System built by Pure Process Technology, LLC. Deuterated solvents were purchased from Cambridge Isotope Laboratories and stored over 3-Å molecular sieves before use. Unless noted, all chemicals were purchased from commercial sources and used without further purification.

$^1$H, $^{11}$B, $^{19}$F, and $^{27}$Al NMR were all recorded using Bruker Avance 400-MHz or 500-MHz NMR spectrometers at room temperature unless otherwise indicated. Chemical shifts for $^1$H NMR were referenced to solvent residues. $^{27}$Al NMR was referenced externally to LiAlH$_4$ in THF-$d_8$, and $^{11}$B and $^{19}$F NMR were referenced externally to BF$_3$·OEt$_2$ in CDCl$_3$. $^{31}$P{$^1$H} NMR chemical shifts were referenced to an external standard of *o*-phosphoric acid in water. FT-IR spectra were recorded in a glovebox with concentrated viscous oils or solution samples using a Bruker ALPHA spectrometer fitted with a diamond-ATR detection unit. Single-crystal X-ray diffraction (XRD) studies were

performed using a Bruker D8 QUEST ECO X-ray diffractometer. Solution and refinement were performed using standard methods,[232,233] and supporting CIF files are available from the CCDC upon request.

## 6.2 Chapter 2: Synthesis and reactivity of next generation base metal heterobimetallic complexes

### 6.2.1 General considerations

Literature Methods were used to synthesize Na[WCp*(CO)$_2$($t$BuNC)][234,235], Na[Mn(CO)$_4$($t$BuNC)],[235,236] IPrCuO$t$Bu,[237] ($^{tBu}$POCOP)NiH,[238] ($^{iPr}$POCOP)NiH,[238] WCp(CO)$_3$H.[239]

### 6.2.2 Synthesis of ($^{tBu}$POCOP)NiWCp(CO)$_3$

In a nitrogen filled glovebox, ($^{tBu}$POCOP)NiH (250 mg, 0.547 mmol) and WCp(CO)$_3$H (182.6 mg, 0.547 mmol) were added to a 100-mL round bottom flask and dissolved in toluene (25 mL).  The reaction was stirred overnight for 12 h. The solution was dried in vacuo resulting in a dark orange powder.  The solid was washed with pentanes to remove unreacted starting material and dried in vacuo to obtain ($^{tBu}$POCOP)NiWCp(CO)$_3$ (389mg, 90% yield). An analytically pure sampled was prepared by vapor diffusion of pentane into a concentrated solution of toluene at    -35 °C to give orange crystals. $^1$H NMR (500 MHz, C$_6$D$_6$): δ 6.74 (t, 1H, J = 8.0, p-ArH), 6.36 (d, 2H, J = 8.0, m-ArH), 5.2 (s, 5H, Cp), 1.35 (vt, 36H, JH-P = 7.4 Hz, CH3). $^{13}$C{$^1$H} NMR (125.77 MHz, C$_6$D$_6$): δ 223.31, 170.17, 129.67, 105.83, 86.85, 38.76, 27.50. $^{31}$P{$^1$H} NMR (161.92 MHz, C$_6$D$_6$): δ 186.31. IR (solid, cm-1): 2962.67, 1910.44 (vCO), 1817.19 (vCO), 1654.02 (vCO), 1259.10, 1086.13,

1017.15, 990.94, 789.58. Anal. Calcd for C30H44O5P2NiW: C, 45.66; H, 5.62. Found: C, 44.86; H, 5.63.

### 6.2.3   Synthesis of ($^{iPr}$POCOP)NiWCp(CO)$_3$

In a nitrogen filled glovebox, ($^{iPr}$POCOP)NiH (50.0 mg, 0.125 mmol) and WCp(CO)$_3$H (41.6 mg, 0.125 mmol) were added to a 20-mL scintillation vial and dissolved in pentane (10 mL).  The reaction mixture was stirred overnight for 12 h. The solution was dried in vacuo resulting in a dark green powder to obtain 80 mg, 87% yield. An analytically pure sample was prepared by vapor diffusion of pentane into a concentrated solution of toluene at -35 °C to give black crystals. $^1$H NMR (400 MHz, C$_6$D$_6$): δ 6.96 (t, 1H, J = 7.8, p-ArH), 6.65 (d, 2H, J = 7.8, m-ArH), 4.88 (s, 5H, Cp), 2.41 (m, 4H, CH(CH3)2), 1.45 (vq, 12H, JH-P = 7.3 Hz, CH3) 1.26 (vq, 12H, JH-P = 6.9 Hz, CH3). $^{13}$C{$^1$H} NMR (125.77 MHz, C$_6$D$_6$): δ 224.14, 168.06, 130.26, 104.83, 88.15, 30.38, 17.80, 17.17. $^{31}$P{$^1$H} NMR (161.92 MHz, C$_6$D$_6$): δ 178.26. IR (solid, cm-1): 3107.66, 2962.17, 2930.37, 2873.58, 1891.33 (vCO), 1800.25 (vCO), 1774.43 (vCO), 1435.44, 995.61, 841.47,  656.37, 479.64. Anal. Calcd for C26H36O5P2NiW: C, 42.60; H, 4.95. Found: C, 42.39; H, 4.94.

### 6.2.4   Procedure for the Reaction of ($^{tBu}$POCOP)NiWCp(CO)$_3$ with H$_2$

In a nitrogen-filled glovebox, ($^{tBu}$POCOP)NiWCp(CO)$_3$ (5 mg, 0.00634 mmol) was dissolved C6D6 (600 μL). The mixture was pipette filtered through Celite into a J-young tube. The tube was fitted to a Schlenk line and exposed to three cycles of freeze-pump-thaw, followed by backfilling with H$_2$ (1 atm). The solution was mixed for five minutes and stored on its side for 24 h.

### 6.2.5   Procedure for the Reaction of ($^{iPr}$POCOP)NiWCp(CO)$_3$ with phenylacetylene

In a nitrogen-filled glovebox, ($^{iPr}$POCOP)NiWCp(CO)$_3$ (5mg, 0.00682 mmol) was dissolved in C6D6 (1 mL). To this solution, phenylacetylene (0.7uL, 0.00682 mmol) was syringed in. The mixture was stirred overnight for 12 h. An aliquot (0.5 mL) was transferred to a J-young tube to be monitored by NMR.

### 6.2.6   Procedure for the Reaction of ($^{iPr}$POCOP)NiH, WCp(CO)$_3$H and phenylacetylene

In a nitrogen-filled glovebox, ($^{iPr}$POCOP)NiH (12 mg, 0.030 mmol) and WCp(CO)$_3$H (10 mg, 0.030 mmol) were added to a scintillation vial and dissolved in C6D6 (1 mL). Immediately, phenylacetylene (3.2 uL, 0.030 mmol) was syringed in.  The reaction mixture was stirred overnight for 12 h. An aliquot (0.5 mL) was transferred to a J-young tube to be monitored by NMR.

### 6.2.7   General procedure for reaction of (POCOP)NiWp complexes and boranes

Equal equivalents of ($^{R}$POCOP)NiWp (R = tBu, iPr) and HB(OR)$_2$ (= HBcat, HBpin) in C$_6$D$_6$ and stirred overnight. Immediate reactivity was observed by orange/red to yellow color changes and analyzed by $^{31}$P NMR to reveal the Ni(II)-H.

### 6.2.8   General procedure for CO$_2$ insertion into ($^{iPr}$POCOP)Ni-CCPh (= - phenylacetylide)

Toluene solutions of ($^{iPr}$POCOP)Ni-CCPh were purged with CO$_2$ in a Parr reactor. The reactor was pressurized to 1-3 atm with CO$_2$ and left to stir overnight at 25 °C – 90 °C

overnight. Conversion to the corresponding Ni(II)-acetylenate (-O(O)C-CCPh) was observed by $^{31}$P NMR shift.

### 6.2.9  Synthesis of ($^{iPr}$POCOP)Ni-COOCCPh (Ni(II)-acetylenate)

Equal equivalents of phenylpropiolic acid (PhCC-C(O)OH) and sodium *t*-butoxide were reacted in THF overnight at gram scale. The mixture was pumped down and recrystallized in the freezer. At 1 mmol scale, sodium phenyl propiolate was reacted with ($^{iPr}$POCOP)NiCl and stirred overnight to afford a yellow solid when pumped down. The crude solid matched that of the $CO_2$ insertion experiments. $^1$H NMR (400 MHz, $C_6D_6$): δ 7.52, 7.09, 6.96, 6.72, 6.57, 2.19 (m, 4H, CH(CH3)2), 0.90(m, 12H, CH3), 0.73(m, 12H, CH3). $^{31}$P{$^1$H} NMR (161.92 MHz, $C_6D_6$): δ 183.10.

### 6.2.10 General procedure for attempted catalytic/stoichiometric C(sp)-H carboxylation of alkynes with (POCOP)NiWp

10 mol % (POCOP)NiWp, phenylacetylene, and additive (additive = HBcat, HBpin, triethoxysilane, methyl iodide, sodium *t*-butoxide, or none) in $C_6D_6$ were loaded into a pressure reactor. The reactor was purged of nitrogen atmosphere and heated to 70 °C and stirred overnight. The reactions were monitored by NMR, displaying no expected products.

### 6.2.11 General procedure for attempted C(sp2)-H thermal borylation of $C_6D_6$ with IPrCuW[M$_{CO}$] ([M$_{CO}$] = Cp*(CO)$_2$(*t*BuNC) or Mn(CO)$_5$(*t*BuNC))

10-20 mol % IPrCuWCp*(CO)$_2$(*t*BuNC) was dissolved in pentane and HBcat, or HBpin, was added and stirred to form a clear orange solution. The reaction was loaded into a J-

Young NMR tube and heated up to 90 °C for 8-24 hours. Relative yields were determined by $^{11}$B NMR.

### 6.2.12 General procedure for attempted photochemical C(sp$^3$)-H borylation of pentane with IPrCuWCp*(CO)$_2$(tBuNC)

10-20 mol % IPrCuWCp*(CO)$_2$(tBuNC) was dissolved in pentane and HBcat, or HBpin, was added and stirred to form a clear orange solution. The reaction was loaded into a J-Young NMR tube and irradiated 8-24 hours. Relative yields were determined by $^{11}$B NMR.

### 6.2.13 General procedure for reaction between NaWCp*(CO)$_2$(tBuNC) and ClB(OR)$_2$

Equal parts ClB(OR)$_2$ (-B(OR)$_2$ = Bcat or Bpin) and NaWCp*(CO)$_2$(tBuNC) were stirred in pentane. Immediate color change from yellow to orange formed. Resonance at approximately 24 ppm in $^{11}$B NMR spectrum matched that of the attempted catalysis experiments.

### 6.2.14 Synthesis of IPrCuWCp*(CO)$_2$(tBuNC)

IPrCuCl (1 eq) was added to a solution of Na[WCp*(CO)$_2$(tBuNC)] (1 eq) in toluene or pentane. The mixture was stirred overnight, filtered, and pumped down to a dry orange powder. $^1$H NMR (400 MHz, C$_6$D$_6$): δ 7.20-7.10 (m, 1H, Ar), 7.05 (m, 2H, Ar), 6.53 (s, 2H), 3.04 (m, 4H, CH(CH3)2), 2.06 (d, 12H, CH3), 2.05 (s, 15H, Cp*), 1.63 (d, 12h, CH3), 1.23 (s, 9H, tBu).

**6.2.15 Synthesis of IPrCuMn(CO)$_5$(*t*BuNC)**

IPrCuCl (1 eq) was added to a solution of Na[Mn(CO)$_5$(*t*BuNC)] (1 eq) in toluene or pentane. The mixture was stirred overnight, filtered, and pumped down to a dry orange powder. $^1$H NMR (400 MHz, C$_6$D$_6$): δ 7.25 (m, 2H, Ar), 7.12 (m, 1H, Ar), 6.28 (s, 2H, NHC), 2.68 (m, 4H, CH(CH3)2), 1.50 (d, 12H, CH3), 1.11 (d, 12H, CH3), 0.87 (s, 9H, tBu).

**6.3   Chapter 3: Mixed Phosphine/Carbonyl Derivatives of Heterobimetallic Copper-Iron and Copper-Tungsten Catalysts**

**6.3.1   General Remarks.**

Unless otherwise noted, all the syntheses were done in a glovebox filled with N$_2$ or using standard Schlenk line techniques. Glassware was oven-dried prior to use. All the chemicals purchased from commercial vendors were used without further purification. Solvents were dried using a Glass Contour solvent purification system built by Pure Process Technology, LLC. Deuterated solvents that were packed under Ar were stored over 3-Å molecular sieves and used without further manipulation. Photolysis was conducted using a 450-W Hanovia mercury arc lamp in an immersion well filled with circulating water. (IPr)CuO*t*Bu[237], [(IPr)CuH]$_2$[237], and (6Pr)CuH[240] were synthesized using previously published literature methods. CpFeCO(PR$_3$)I[241], CpFeCO(PR$_3$)H (R= PEt$_3$, P$^n$Bu$_3$, PMe$_2$Ph, PMePh$_2$, PPh$_3$)[165], and Cp*W(CO)$_2$(PR$_3$)H (R= PEt$_3$, PMe$_2$Ph, PMePh$_2$)[242], were all synthesized by adapted literature methods.

### 6.3.2 Instrumentation

All the NMR spectra were recorded at ambient temperature using either Bruker Avance DPX-400 or Bruker Avance DPX-500 MHz instruments. Mass analyses were performed with an Advion Expression$^L$ CMS mass spectrometer using atmospheric pressure chemical ionization (APCI) in selected ion monitoring (SIM) mode. FT-IR spectra were recorded in a glovebox on powder samples using a Bruker ALPHA spectrometer fitted with a diamond-ATR detection unit. Elemental analyses were performed by the Midwest Microlab, LLC, in Indianapolis, IN. Single-crystal X-ray diffraction experiments were performed using a Bruker PHOTON II diffractometer. Data reduction, solution, and refinement was performed by standard methods,[233] and CIF files are available as Supplementary Material.

### 6.3.3 Synthetic Procedure A: Preparation of (IPr)CuFeCp(CO)(PR3) (R= PEt3, PnBu3, PMe2Ph, PMePh2) (1a-d) and (IPr)Cu(μ-H)2FeCp(PPh3) (2)

In a nitrogen-filled glovebox, CpFe(CO)(PR$_3$)H (1 equiv.) was dissolved in C$_6$H$_6$ (1 mL) and kept the vial in freezer for 10 mins. In a separate vial, (IPr)CuOtBu (1 equiv.) was dissolved in C$_6$H$_6$. While stirring, (EtO)$_3$SiH (1.01 equiv.) was syringed in, turning the solution to a bright yellow color consistent with formation of [(IPr)CuH]$_2$. The [(IPr)CuH]$_2$ solution was pipette-filtered through Celite into the CpFe(CO)(PEt$_3$)H vial. The reaction turned orange-brown in 5 mins and then the solution was dried *in vacuo*, resulting in an orange-brown precipitate. The solution was extracted with pentane and pipette-filtered through Celite. Crystallization was accomplished by leaving a concentrated solution in pentane at −35 °C.

### 6.3.4 Preparation of (IPr)CuFeCp(CO)(PEt₃) (1a)

Following procedure A with CpFe(CO)(PEt₃)H (14.0 mg, 0.0522 mmol) in $C_6H_6$ (1 mL), (IPr)CuOtBu (27.4 mg, 0.0522 mmol) in $C_6H_6$ (1 mL), and (EtO)₃SiH (10.1 μL, 0.0530 mmol) Yield: 17.2 mg, 0.023 mmol, 44%. $^1$H NMR (400 MHz, $C_6D_6$): $\delta$ 7.25 (t, J = 8.0 Hz, 2H, *p*-H), 7.12-7.18 (m, 4H, *m*-H), 6.30 (s, 2H, NCH), 4.01 (s, 5H, Cp), 2.92 (sept., J = 8.0 Hz, 2H, C$\underline{H}$(CH₃)₂), 2.80 (sept., J = 8.0 Hz, 2H, C$\underline{H}$(CH₃)₂), 1.50 (d, J = 12.0 Hz, 6H, CH(C$\underline{H}$₃)₂), 1.49 (d, J = 12.0 Hz, 6H, CH(C$\underline{H}$₃)₂), 1.38-1.45 (m, 3H, PC$\underline{H}$₂CH₃), 1.09-1.16 (m, 3H, PC$\underline{H}$₂CH₃), 1.09 (d, J = 8.0 Hz, 6H, CH(C$\underline{H}$₃)₂), 1.08 (d, J = 8.0 Hz, 6H, CH(C$\underline{H}$₃)₂), 0.88-0.97 (m, 9H, PCH₂C$\underline{H}$₃). $^{31}$P{$^1$H} NMR (162 MHz, $C_6D_6$): $\delta$ 68.49. $^{13}$C{$^1$H} NMR (100 MHz, $C_6D_6$): $\delta$ 221.6 (CO), 179.6 (NCCu), 145.8, 136.0, 130.0, 124.0, 123.8, 121.2, 73.4 (Cp), 28.8, 28.7, 25.2, 25.0, 24.3, 24.2, 23.8, 23.6, 8.7. IR (solid, cm$^{-1}$): 2961, 2927, 2869, 1791 ($v_{CO}$), 1457, 1401, 1326, 1180, 1104, 1003, 943, 799, 758, 730, 680, 533. Satisfactory elemental analysis data was not obtained due to thermal instability of the complex.

### 6.3.5 Preparation of (IPr)CuFeCp(CO)(P$^n$Bu₃) (1b)

Following procedure A with CpFe(CO)(P$^n$Bu₃)H (25.0 mg, 0.0709 mmol) in $C_6H_6$ (1 mL), (IPr)CuOtBu (37.2 mg, 0.0709 mmol) in $C_6H_6$ (1 mL), and (EtO)₃SiH (13.9 μL, 0.0710 mmol). Yield: 23.9 mg, 0.0297 mmol, 42%. $^1$H NMR (400 MHz, $C_6D_6$): $\delta$ 7.27 (t, J = 8.0 Hz, 2H, *p*-H), 7.14-7.20 (m, 4H, *m*-H partial overlap with solvent peak), 6.27 (s, 2H, NCH), 4.00 (s, 5H, Cp), 2.95 (sept., J = 8.0 Hz, 2H, C$\underline{H}$(CH₃)₂), 2.79 (sept., J = 8.0 Hz, 2H, C$\underline{H}$(CH₃)₂), 1.53 (d, J = 8.0 Hz, 6H, CH(C$\underline{H}$₃)₂), 1.51 (d, J = 16.0 Hz, 6H, CH(C$\underline{H}$₃)₂), 1.19-1.46 (m, 18H, P(C$\underline{H}$₂)₃CH₃), 1.10 (d, J = 8.0 Hz, 6H, CH(C$\underline{H}$₃)₂), 1.10 (d, J = 8.0 Hz, 6H, CH(C$\underline{H}$₃)₂), 0.96 (t, J = 8.0 Hz, 9H, P(CH₂)₃C$\underline{H}$₃) . $^{31}$P{$^1$H} NMR (162 MHz,

$C_6D_6$): $\delta$ 61.53. $^{13}C\{^1H\}$ NMR (100 MHz, $C_6D_6$): $\delta$ 221.7 (CO), 179.6 (NCCu), 145.8, 136.1, 130.1, 124.1, 123.8, 121.2, 73.4 (Cp), 33.2, 33.0, 28.8, 28.7, 26.8, 24.8, 24.7, 24.2, 24.1, 24.0, 23.7, 14.0. IR (solid, $cm^{-1}$): 2960, 2925, 2866, 1795 ($v_{CO}$), 1458, 1406, 1325, 1172, 1109, 946, 936, 801, 757, 733, 708, 573, 535. Satisfactory elemental analysis data was not obtained due to thermal instability of the complex.

### 6.3.6  Preparation of (IPr)CuFeCp(CO)(PMe₂Ph) (1c)

Following procedure A with CpFe(CO)(P Me₂Ph)H (11.3 mg, 0.0392 mmol) in $C_6H_6$ (1 mL), (IPr)CuOtBu (20.5 mg, 0.0392 mmol) in $C_6H_6$ (1 mL), and (EtO)₃SiH (7.7 µL, 0.0400 mmol). Yield: 6.7 mg, 0.009 mmol, 23%. $^1H$ NMR (400 MHz, $C_6D_6$): $\delta$ 7.81-7.85 (m, 2H, PC₆$\underline{H}$₆), $\delta$ 7.22 (t, J = 8.0 Hz, 2H, *p*-H), 7.13-7.16 (m, 4H, *m*-H partial overlap with solvent peak), $\delta$ 7.11-7.13 (m, 2H, PC₆$\underline{H}$₆), $\delta$ 7.03-7.06 (m, 1H, PC₆$\underline{H}$₆), 6.31 (s, 2H, NCH), 3.93 (s, 5H, Cp), 2.87 (sept., J = 8.0 Hz, 2H, C$\underline{H}$(CH₃)₂), 2.80 (sept., J = 8.0 Hz, 2H, C$\underline{H}$(CH₃)₂), 1.53 (d, J = 8.0 Hz, 6H, CH(C$\underline{H}$₃)₂), 1.49 (d, J = 8.0 Hz, 6H, CH(C$\underline{H}$₃)₂), 1.41 (d, J = 8.0 Hz, 3H, PC$\underline{H}$₃), 1.18 (d, J = 8.0 Hz, 3H, PC$\underline{H}$₃), 1.10 (d, J = 8.0 Hz, 12H, CH(C$\underline{H}$₃)₂). $^{31}P\{^1H\}$ NMR (400 MHz, $C_6D_6$): $\delta$ 44.89. IR (solid, $cm^{-1}$): 2961, 2927, 2868, 1793 ($v_{CO}$), 1458, 1401, 1325, 1270, 1179, 1060, 1011, 932, 896, 799, 758, 741, 692, 599, 536. Satisfactory elemental analysis data was not obtained due to thermal instability of the complex.

### 6.3.7  Preparation of (IPr)CuFeCp(CO)(PMePh₂) (1d)

Following procedure A with CpFe(CO)(PMePh₂)H (66.6 mg, 0.1903 mmol) in $C_6H_6$ (1 mL), (IPr)CuOtBu (100.0 mg, 0.1903 mmol) in $C_6H_6$ (1 mL), and (EtO)₃SiH (38 µL, 0.1910 mmol). Yield: 32.1 mg, 0.039 mmol, 21%. $^1H$ NMR (400 MHz, $C_6D_6$): $\delta$ 7.75-7.79

(m, 2H, PC$_6$H$_6$), $\delta$ 7.54-7.58 (m, 2H, PC$_6$H$_6$), $\delta$ 7.22 (t, J = 8.0 Hz, 2H, $p$-H), 7.12-7.16

(m, 4H, $m$-H partial overlap with solvent peak), $\delta$ 7.07-7.10 (m, 6H, PC$_6$H$_6$), 6.31 (s, 2H,

NCH), 3.93 (s, 5H, Cp), 2.93 (sept., J = 8.0 Hz, 2H, CH(CH$_3$)$_2$), 2.75 (sept., J = 8.0 Hz,

2H, CH(CH$_3$)$_2$), 1.51 (d, J = 4.0 Hz, 6H, CH(CH$_3$)$_2$), 1.44 (d, J = 8.0 Hz, 3H, PCH$_3$), 1.35

(d, J = 8.0 Hz, 6H, CH(CH$_3$)$_2$), 1.09 (d, J = 4.0 Hz, 6H, CH(CH$_3$)$_2$), 1.08 (d, J = 4.0 Hz,

6H, CH(CH$_3$)$_2$). $^{31}$P{$^1$H} NMR (162 MHz, C$_6$D$_6$): $\delta$ 65.56. IR (solid, cm$^{-1}$): 2959, 2924,

2865, 1813 ($v_{CO}$), 1457, 1433, 1325, 1211, 1085, 1064, 1011, 945, 879, 802, 759, 744,

698, 596, 538, 506. Satisfactory elemental analysis data was not obtained due to

thermal instability of the complex.


### 6.3.8  Preparation of (IPr)Cu($\mu$-H)$_2$FeCp(PPh$_3$) (2)

Following procedure A with CpFe(CO)(PPh$_3$)H (24.3 mg, 0.0587 mmol) in C$_6$H$_6$ (1 mL),

(IPr)CuOtBu (31.0 mg, 0.0587 mmol) in C$_6$H$_6$ (1 mL), and (EtO)$_3$SiH (11.8 μL, 0.0600

mmol. During recrystallization it was found that the decomposition product **2** was

produced. Yield: 4.3 mg, 0.005 mmol, 9%. $^1$H NMR (400 MHz, C$_6$D$_6$): $\delta$ 7.70-7.75 (m,

6H, PC$_6$H$_6$), $\delta$ 7.22 (m, 2H, $o$-H partial overlap with solvent peak), 7.09 (d, J = 8.0 Hz,

4H, $m$-H), $\delta$ 6.93-7.01 (m, 9H, PC$_6$H$_6$), 6.19 (s, 2H, NCH), 3.66 (s, 5H, Cp), 2.77 (sept.,

J = 8.0 Hz, 4H, CH(CH$_3$)$_2$), CH(CH$_3$)$_2$), 1.42 (d, J = 8.0 Hz, 12H, CH(CH$_3$)$_2$), 1.09 (d, J =

8.0 Hz, 12H, CH(CH$_3$)$_2$), –17.77 (d, J = 40.0 Hz, 2H, $\mu$-H). $^{31}$P{$^1$H} NMR (162 MHz,

C$_6$D$_6$): $\delta$ 94.69. IR (solid, cm$^{-1}$): 2958, 2924, 2867, 1616, 1585, 1471, 1433, 1309, 1268,

1181, 1062, 1000, 988, 942, 803, 745, 694, 530, 516, 496, 474, 449, 422.

### 6.3.9  Procedure B: Preparation of (NHC)CuWCp*(CO)$_2$(PR$_3$) (3a-c)

Cp*W(CO)$_2$(PR$_3$)H was produced by the addition of phosphine (3 equiv.) to a solution of Cp*W(CO)$_3$H (1.5 equiv.) in toluene (10 mL) and heating at 110°C in a closed vial for three days. The crude product was pumped down *in vacuo* at room temperature until dry and then at 60°C for 3 h. The crude material was then dissolved in pentane (10 mL) and stored at -30°C overnight. The solution was pipet-filtered through Celite to remove white crystals and used without further purification. In a separate vial, (NHC)CuOtBu (1 equiv.) was dissolved in pentane (5 mL). While stirring, (EtO)$_3$SiH (1 equiv.) was syringed in, turning the solution to a bright yellow color consistent with formation of [(IPr)CuH]$_2$. The [(IPr)CuH]$_2$ solution was pipette-filtered through Celite into the solution of Cp*W(CO)$_2$(PR$_3$)H. The reaction was left to stir overnight with slow formation of a dark yellow-orange color. The crude product was recrystallized two times from slow evaporation of pentane solutions in the glovebox freezer at -30°C to obtain yellow to red crystals suitable for characterization.

### 6.3.10 Preparation of IPrCuWCp*(CO)$_2$(PEt$_3$) (3a)

Following procedure B, PEt$_3$, (37.6 mg, 0.495 mmol), Cp*W(CO)$_3$H (100mg, 0.247 mmol), (IPr)CuOtBu (89 mg, 0.17 mmol), and (EtO)$_3$SiH (25 µL, 0.17 mmol) were used. Yield: 105 mg, 0.11 mmol, 66%. $^1$H NMR (400 MHz, C$_6$D$_6$): $\delta$ 7.36-7.16 (m, 3H, ArH), 6.41 (s, 2H, NCH), 2.97 (sept., J = 6.5 Hz, 4H, CH(CH$_3$)$_2$), 1.96 (s, 15H, Cp*), 1.58 (d, J = 6.5 Hz, 12 H, CH(CH$_3$)$_2$), 1.36 (t, J = 8.0 Hz, 9H, PCH$_2$CH$_3$), 1.08 (d, J = 6.5 Hz, 12H, CH(CH$_3$)$_2$), 1.01-0.94(m, 6H, PCH$_2$CH$_3$) $^{31}$P{$^1$H} NMR (162 MHz, C$_6$D$_6$): $\delta$ 21.24. IR (solid, cm$^{-1}$): 2957, 2869, 1750($\nu_{CO}$), 1691($\nu_{CO}$), 1456, 1364, 1330, 1027, 802, 759, 700,

564, 483, 418. Elemental analysis calculated (%) for [$C_{45}H_{62}O_2CuWPN_2$] C 57.41, H 6.63, N 2.97; found C 57.39, H 6.88, N 2.92.

### 6.3.11 Preparation of IPrCuWCp*(CO)₂(PMe₂Ph) (3b)

Following procedure B, PMe₂Ph, (68.38 mg, 0.495 mmol), Cp*W(CO)₃H (100mg, 0.247 mmol), (IPr)CuOtBu (89 mg, 0.17 mmol), and (EtO)₃SiH (25 µL, 0.17 mmol) were used. Yield: 96 mg, 0.10 mmol, 60%. ¹H NMR (400 MHz, C₆D₆): δ 7.72 (t, J = 7.5 Hz, 2H, ArH), 7.26-7.22 (m, 3H, ArH), 7.16-7.13 (m, 2H, ArH-overlap with solvent) 7.03-6.96 (m, 4H, ArH), 6.45 (s, 2H, NCH), 2.97 (sept., J = 6.5 Hz, 4H, C$\underline{H}$(CH₃)₂), 1.80 (s, 15H, Cp*), 1.61 (d, J = 6.5 Hz, 12 H, CH(C$\underline{H_3}$)₂), 1.52 (s, 3H, PMe), 1.50 (s, 3H, PMe), 1.10 (d, J = 6.5 Hz, 12H, CH(C$\underline{H_3}$)₂), ³¹P{¹H} NMR (162 MHz, C₆D₆): δ 3.35. IR (solid, cm⁻¹): 3114, 2960, 2906, 2866, 1778($v_{CO}$), 1702($v_{CO}$), 902, 800, 743, 698, 677, 573, 483, 427. Repeated attempts at elemental analysis did not give satisfactory results. ¹H and ³¹P NMR spectroscopy was used to assess purity (see Supplementary Material).

### 6.3.12 Preparation of IPrCuWCp*(CO)₂(PMePh₂) (3c)

Following procedure B, PMePh₂, (99.1 mg, 0.495 mmol), Cp*W(CO)₃H (100mg, 0.247 mmol), (IPr)CuOtBu (89 mg, 0.17 mmol), and (EtO)₃SiH (25 µL, 0.17 mmol) were used. Yield: 75 mg, 0.073 mmol, 43%. ¹H NMR (400 MHz, C₆D₆): δ 7.72 (t, J = 7.5 Hz, 4H, ArH), 7.24-7.12 (m, 10H, ArH), 7.03 (t, J = 7.0 Hz, 2H, ArH) 6.42 (s, 2H, NCH), 2.94 (sept., J = 7.0 Hz, 4H, C$\underline{H}$(CH₃)₂), 1.78 (s, 15H, Cp*), 1.75 (d, J = 8.1 Hz, 3H, PMe) 1.53 (d, J = 7.0 Hz, CH(C$\underline{H_3}$)₂), 1.07 (d, J = 7.0 Hz, 12H, CH(C$\underline{H_3}$)₂), ³¹P{¹H} NMR (162 MHz, C₆D₆): δ 25.64. IR (solid, cm⁻¹): 2962, 2901, 2867, 1762($v_{CO}$), 1693($v_{CO}$), 1459, 887,

744, 695, 524, 490, 422.  Elemental analysis calculated (%) for [$C_{52}H_{60}O_2CuWPN_2$] C 61.03, H 5.91, N 2.74; found C 60.87, H 5.91, N 2.59.

### 6.3.13 Preparation of 6PrCuWCp*(CO)₂(PEt₃) (3d)

$PEt_3$, (32 mg, 0.420 mmol, 2 equiv.) was added to a solution of Cp*W(CO)₃H (85 mg, 0.210, 1.5 equiv.) in toluene (10 mL) and heated at 110°C for three days. The crude product was pumped down *in vacuo* at room temperature until dry and then at 60°C for 3 h to give 104 mg (0.210mmol. The crude product was dissolved pentane (10 mL), and 6PrCuH (98 mg, 0.21 mmol) was added. Recrystallization from slow evaporating pentane in the glovebox freezer at -30°C gave pure product. This product was further recrystallized in slow evaporating pentane to afford crystals for single crystal XRD analysis. Yield: 30 mg, 0.031 mmol, 15%. $^1$H NMR (400 MHz, $C_6D_6$): $δ$ 7.24-7.17 (m, 4H, Ar-H significant overlap with solvent), 3.41 (sept., J = 6.7 Hz, 4H, CH(CH₃)₂), 2.92 (t, J = 5.7 Hz, 4H, NCH₂CH₂CH₂N) 1.88 (s, 15H, Cp*), 1.74 (d, J = 6.5 Hz, 12 H, CH(CH₃)₂), 1.17 (d, J = 6.5 Hz, 12H, CH(CH₃)₂), 1.01-0.94 (m, 9H, PCH₂CH₃), 0.89-0.80(m, 6H, PCH₂CH₃) $^{31}$P{$^1$H} NMR (162 MHz, $C_6D_6$): $δ$ 20.75. IR (solid, cm−1): 2956, 2930, 2902, 2872, 1753($v_{CO}$), 1688, 1483, 1446, 1321, 1295, 1198, 1026, 803, 758, 700, 641, 604, 560, 410. *m/z* (APCI+ SIM mode): 118.1(PEt₃), 135.2(Cp*), 404.3(6Pr), 467.2(6PrCu), 493.1(Cp*W(CO)₂PEt₃), 960.4(6PrCuCp*W(CO)₂PEt₃)

### 6.3.14 General procedure in the synthesis of CpFeCO(PR₃)H

In a nitrogen filled glovebox, CpFeCO₂I (0.5 equiv.) and Phosphine ligand (0.6 equiv.) was dissolved in THF (2 mL) in the vial and the reaction was heated up at 85 °C from 3 h to 12 h[241]. The solution was dried in vacuo, resulting in a green precipitate. The

solution was extracted with pentane and pipette-filtered through Celite to get the starting materials, CpFeCO(PR$_3$)I. Then, CpFeCO(PR$_3$)I (0.5 equiv.) and NaBH$_4$ (2.5 equiv.) as proton source was dissolved in THF (2 mL) in the vial and the reaction was heated up at 60 °C from 3 h to 8 h[165]. The solution was dried in vacuo, resulting in a yellow-brown precipitate. The solution was extracted with pentane and pipette-filtered through Celite to get the precursors, CpFeCO(PR$_3$)H.

6.3.14.1    CpFeCO(P$^n$Bu$_3$)H - $^1$H NMR (400 MHz, C$_6$D$_6$): $\delta$ 4.35 (s, 5H, Cp), 1.13-
   1.45 (m, 18H, P(C<u>H$_2$</u>)$_3$CH$_3$), 0.87 (t, J = 8.0 Hz, 9H, P(CH$_2$)$_3$C<u>H$_3$</u>), −13.97 (d, J =
   72.0 Hz, 1H). $^{31}$P{$^1$H} NMR (162 MHz, C$_6$D$_6$): $\delta$ 67.89.

6.3.14.2    CpFeCO(PEt$_3$)H - $^1$H NMR (400 MHz, C$_6$D$_6$): $\delta$ 4.29 (s, 5H, Cp), 1.15-1.25
   (m, 6H, P(C<u>H$_2$</u>)CH$_3$), 0.78-0.87 (m, 9H, P(CH$_2$)C<u>H$_3$</u>), −14.00 (d, J = 76.0 Hz,
   1H). $^{31}$P{$^1$H} NMR (162 MHz, C$_6$D$_6$): $\delta$ 75.11.

6.3.14.3    CpFeCO(PMe$_2$Ph)H - $^1$H NMR (400 MHz, C$_6$D$_6$): δ 7.45-7.50 (m, 4H,
   PC$_6$H$_6$), 7.00-7.12 (m, 6H, PC$_6$H$_6$), 4.21 (s, 5H, Cp), 1.26-1.30 (m, 6H, PCH$_3$),
   _13.89 (d, J = 80.0 Hz, 1H) $^{31}$P{$^1$H} NMR (162 MHz, C$_6$D$_6$): δ 51.88

6.3.14.4    CpFeCO(PMePh$_2$)H - $^1$H NMR (400 MHz, C$_6$D$_6$): δ 7.42-7.54 (m, 4H,
   PC$_6$H$_6$), 6.97-7.06 (m, 6H, PC$_6$H$_6$), 4.22 (s, 5H, Cp), 1.64 (d, J = 8.0 Hz, 3H,
   PCH$_3$), _13.42 (d, J = 76.0 Hz, 1H) $^{31}$P{$^1$H} NMR (162 MHz, C$_6$D$_6$): δ 69.83

6.3.14.5    CpFeCO(PPh$_3$)H - $^1$H NMR (400 MHz, C$_6$D$_6$): δ 7.61-7.68 (m, 6H, PC$_6$H$_6$),
   6.95-7.22 (m, 9H, PC$_6$H$_6$), 4.27 (s, 5H, Cp), _13.79 (d, J = 76.0 Hz, 1H) $^{31}$P{$^1$H}
   NMR (162 MHz, C$_6$D$_6$): δ 88.26.

## 6.3.15 General procedure for synthesis of Cp*W(CO)$_2$(PR$_3$)H

Cp*W(CO)$_2$(PR$_3$)H was produced by the addition of phosphine (3 equiv.) to a
solution of Cp*W(CO)$_3$H (1.5 equiv.) in toluene (10 mL) and heating at 110°C in a
closed vial for three days. The crude product was pumped down *in vacuo* at room
temperature until dry and then at 60°C for 3 h[242].

### 6.3.16 Characterization of Cp*W(CO)$_2$PR$_3$H

6.3.16.1       Cp*W(CO)$_2$(PEt$_3$)H - - $^1$H NMR (400 MHz, C$_6$D$_6$): δ 1.94 (s, 15H, Cp*), 1.41 (m, 9H, PCH$_2$CH$_3$), 0.83 (s, 6H, PCH$_2$CH$_3$), -7.17, 7.34 (s, 1H, cis/trans-W-H) (-6.51 is remaining starting material). $^{31}$P{1H} NMR (162 MHz, C$_6$D$_6$): δ 17.3 ( -22.23 starting material)

6.3.16.2       Cp*W(CO)$_2$(PMe2Ph)H - $^1$H NMR (400 MHz, C$_6$D$_6$): δ 7.49 (t, J = 7.5 Hz, 2H, PC$_6$H$_6$), 7.11 (t, J = 7.5 Hz, 2H, PC$_6$H$_6$), 7.02 (t, J = 7.5 Hz, 1H, PC$_6$H$_6$), 1.78 (s, 15H, Cp*), 1.57 (s, 3H, PMe), 1.55 (s, 3H, PMe), _6.65,-6.80 (s, 1H, cis/trans W-H). $^{31}$P{1H} NMR (162 MHz, C$_6$D$_6$): δ -2.03, -47.98 (starting material)

6.3.16.3       Cp*W(CO)$_2$(PMePh$_2$)H - $^1$H NMR (400 MHz, C$_6$D$_6$): δ 7.59-7.49 (m, 5H, PC$_6$H$_6$), 7.39-7.23 (m, 5H, PC$_6$H$_6$), 1.77 (s, 15H, Cp*), 1.36 (s, 3H, PMe), _6.40,-6.58 (s, 1H, cis/trans W-H). $^{31}$P{1H} NMR (162 MHz, C$_6$D$_6$): δ 19.63, -20.82(starting material)

## 6.4 Chapter 4: Detection of a ligand redistribution process for hydrocarbon-soluble Mg{Al[OC(Ph)(CF$_3$)$_2$]$_4$}$_2$: evidence of a "hidden equilibrium" in polyfluorinated alkoxyaluminate chemistry

### 6.4.1 Instrumentation.

Conductivity was measured with a Mettler Toledo Seven Compact S213 conductivity probe. Cyclic voltammetry was measured using a Biologic SP200 potentiostat with a standard three-electrode setup. A 2-mm Pt disc working electrode from CH Instruments was polished with 1, 0.3, and 0.5 μm alumina powder. Counter and reference electrodes were mechanically abraded magnesium strips of foil (Gallium Source). $^1$H, $^{11}$B, $^{19}$F, and $^{27}$Al NMR were all recorded using Bruker Avance 400-MHz or 500-MHz NMR spectrometers at room temperature unless otherwise indicated. Chemical shifts for $^1$H NMR were referenced to solvent residues. $^{27}$Al NMR was referenced externally to LiAlH$_4$ in THF-d$_8$, and $^{11}$B and $^{19}$F NMR were referenced externally to BF$_3$·OEt$_2$ in CDCl$_3$. FT-IR spectra were recorded in a glovebox with concentrated viscous oils or solution samples using a Bruker ALPHA spectrometer fitted with a diamond-ATR detection unit. Single-crystal X-ray diffraction (XRD) studies were performed using a Bruker D8 QUEST ECO X-ray diffractometer. Solution and refinement were performed using standard methods,[232,233] and supporting CIF files are available from the CCDC upon request.

### 6.4.2 Ligand rearrangement synthesis

6.4.2.1 Mg(hPhip)$_2$ , 1:

Magnesium methoxide in methanol (approximately 12 g) was pumped down to a dry solid. Solid Mg(OMe)$_2$ (86 mg, 1.0 mmol , 1.0 eq) was dissolved in a scintillation vial in DME

(10 mL). To the cloudy mixture was added 1,1,1,3,3,3-hexafluoro-2-phenylisopropanol

(hPhip·H, 537mg, 2.20 mmol, 2.20 eq) and allowed to stir for 1 d, providing a clear

colorless solution. The mixture was pumped down under vacuum to a viscous colorless

oil. $^1$H NMR (400 MHz, $C_6D_6$): δ 8.11 (d, J = 7.3 Hz, 4H), 7.27 (d, J = 7.6 Hz, 9H), 7.20

(d, 6H, J = 7.6 Hz), 3.16 (s, 8H), 3.12 (s, 12H). $^{19}$F NMR (376 MHz, $C_6D_6$): δ -75.89.

### 6.4.2.2 Al(hPhip)3, 2:

To a freezer chilled solution (-20 °C) of 1,1,1,3,3,3-hexafluoro-2-phenylisopropanol (hPhip·H, 1560 mg, 6.40 mmol, 6.40 eq) in a scintillation vial in DME (10 mL) was slowly added AlMe$_3$ (25 wt.% in hexane, 1730 mg, 2.00 mmol, 2.00 eq). After vigorous gas evolution ceased, the vial was capped loosely and allowed to warm to room temperature. The reaction vial was slowly opened to allow any excess gas evolution to proceed. The mixture was then stirred for 1 day. The reaction mixture was pumped down under vacuum to a viscous colorless cloudy oil. $^1$H NMR (400 MHz, acetone-d6): δ 7.82 (m, 6H), 7.54-7.49 (m, 9H). $^{19}$F NMR (376 MHz, C$_6$D$_6$): δ -75.54. $^{27}$Al NMR (104 MHz, C$_6$D$_6$): δ 31.31.

### 6.4.2.3 Mg[Al(hPhip)4]2, 3:

Viscous oils of 1 and 2 (at a molar ratio of 1:2 respectively) were dissolved in DME (0.2 M) in scintillation vials. 1 was added to 2 and the mixture was stirred at room temperature for 4 days. The reaction was pumped down under vacuum to a yellow viscous oil for characterization. Analogous oils could also be obtained by using THF in place of DME. To prepare samples for analysis in other solvents, the desired analysis solvent (diglyme, C$_6$D$_6$, toluene) was added to the oil, and the mixture pumped down slowly under vacuum to the desired volume. $^1$H NMR (400 MHz, C$_6$D$_6$): δ 8.50-7.80 (m), 7.43-7.11 (m). $^{19}$F NMR (376 MHz, C$_6$D$_6$): δ -74.43, -75.41, -75.57. $^{27}$Al NMR (104 MHz, C$_6$D$_6$): δ 45.27, 31.49 (Al(hPhip)3).

### 6.4.3 Orthogonal synthesis

#### 6.4.3.1 LiAl(hPhip)$_4$, 4:

To a freezer cooled (-20 °C) cloudy solution of LiAlH$_4$ (76 mg, 1 mmol, 1 eq) in THF (10 mL) in a scintillation vial was added slowly 1,1,1,3,3,3-hexafluoro-2-phenylisopropanol (1.0 g, 4.1 mmol, 4.1 eq). The stirred solution bubbled vigorously and was allowed to warm to room temperature and then capped loosely. The reaction mixture was allowed to stir at room temperature overnight. The cap was removed slowly to let any remaining gas bubble off, and then the solution pumped down under vacuum to a sticky white semi-solid and used without further purification. $^1$H NMR (400 MHz, CD$_3$CN): δ 8.06-7.78 (m, 8H), 7.49-7.11 (m, 12H), $^{27}$Al NMR (104 MHz, THF in-situ): δ 48.67.

### 6.4.3.2 H(OEt$_2$)$_2$Al(hPhip)$_4$ 5:

Crude 4 was suspended in DCM (25 mL) in a round bottom flask. To the solution was syringed hydrogen chloride (1.0 M in diethyl ether, 1.0 mL, 1.0 mmol, 1.0 eq). The reaction was stirred overnight. The precipitated LiCl was filtered off over Celite and the solution was reduced under vacuum to a viscous colorless oil and used without further purification. $^{27}$Al NMR (104 MHz, toluene in-situ): δ 80.83, 59.43.

### 6.4.3.3 Mg[Al(hPhip)$_4$]$_2$, 3:

In a scintillation vial, crude 4 was dissolved in toluene (10 mL) and n-butyl-sec-butylmagnesium (0.7M in hexane, 715 μL, 0.500 mmol, 0.500 eq) was added slowly at room temperature. The reaction was capped very loosely and allowed to evolve gas slowly for several hours. Each hour for three hours, the reaction was opened to allow gas to be released. The reaction was then stirred for 18 h and pumped down to a viscous yellow oil. $^{1}$H NMR (400 MHz, C$_6$D$_6$): δ 8.38 (m), 8.19 (m), 8.15-8.00 (m), 8.00-7.90 (m), 7.34-7.15 (m), 4.16 (m), 1.26 (m). $^{27}$Al NMR (104 MHz, C$_6$D$_6$): δ 41.02, 33.80. $^{19}$F NMR (376 MHz, C$_6$D$_6$): δ -74.52.

### 6.4.4 Experimental spectra
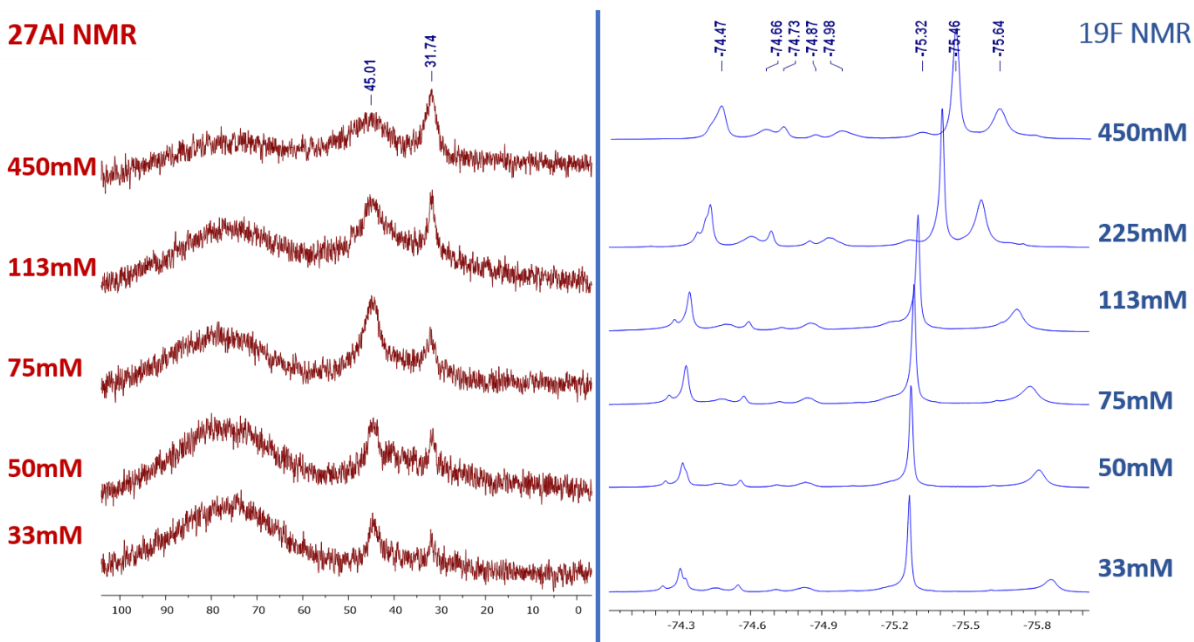


**Figure 6-1.** $^{27}$Al NMR (left, red) and $^{19}$F NMR (right, blue) spectra of Mg[Al(hPhip)$_4$]$_2$ in C$_6$D$_6$ at different concentrations



$^{27}$Al NMR (G2)
Ratio of Peak 3 : Peak 2 Integration

|       | Ratio |
|-------|-------|
| 45 C  | 12.2  |
| 65 C  | 11.3  |
| 85 C  | 12.3  |
| 105 C | 10.9  |
| 125 C | 8.4   |
| 145 C | 7.8   |
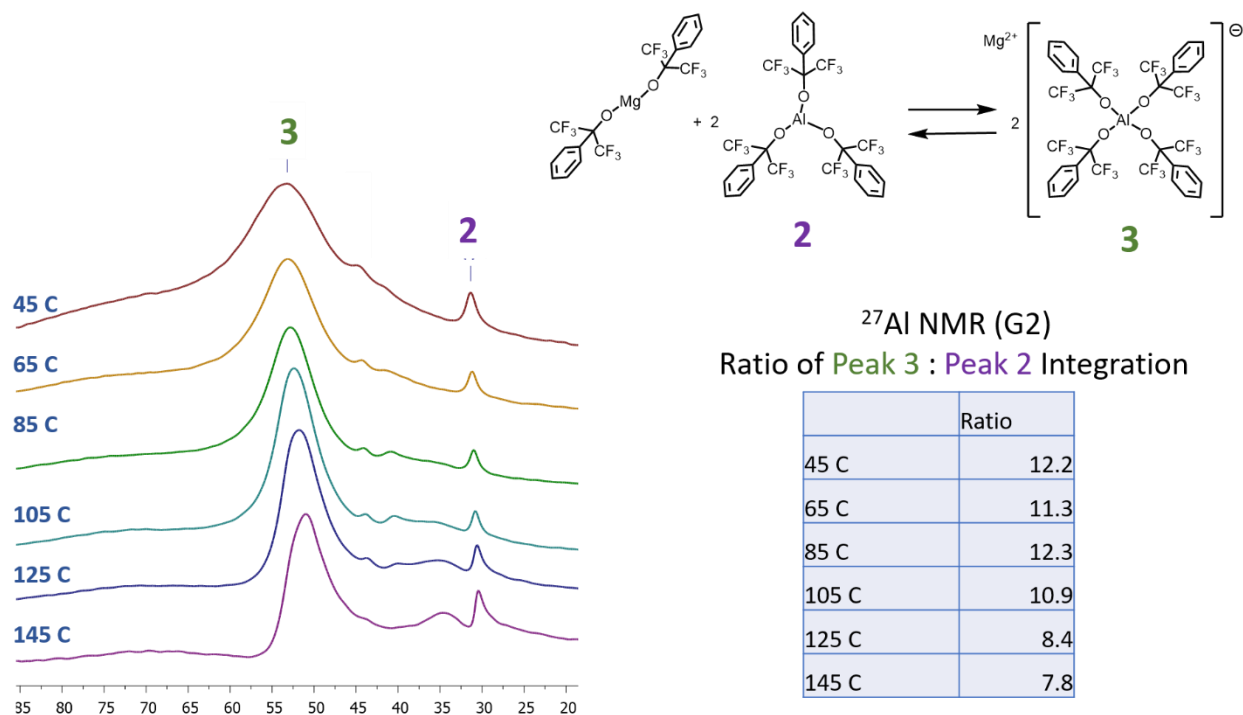
**Figure 6-2.** $^{27}$Al VT-NMR of 0.2M Mg[Al(hPhip)$_4$]$_2$ in G2 at different temperatures and the ratio of their peak integrations
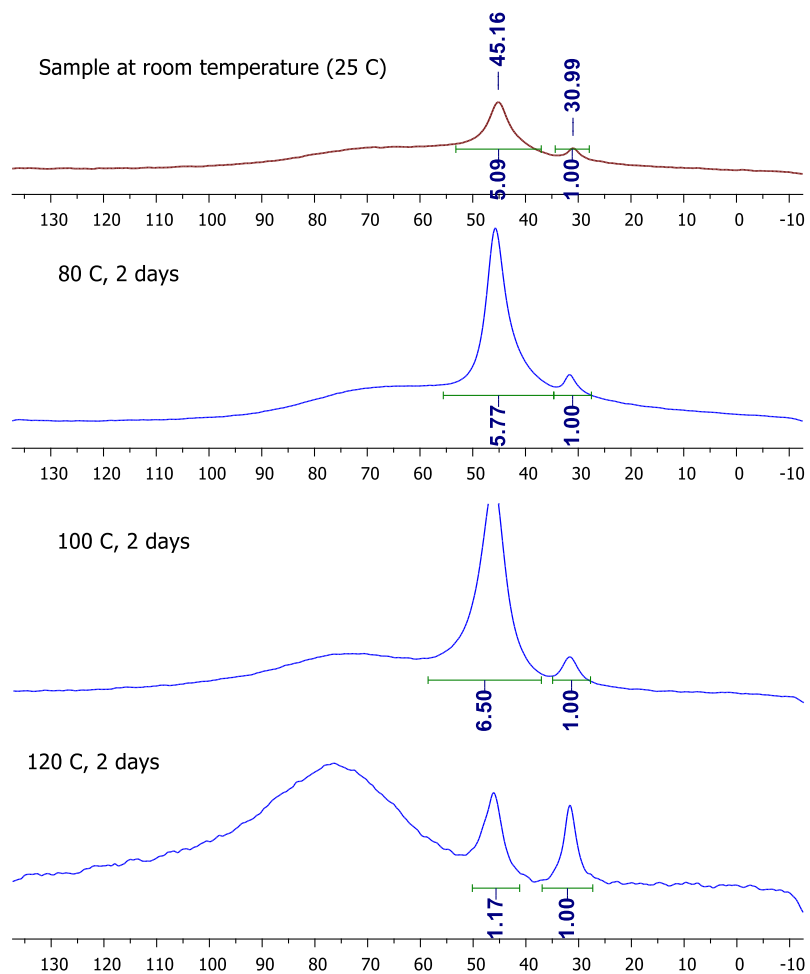
**Figure 6-3.** $^{25}$Al NMR: Mg[Al(hPhip)$_4$]$_2$ in G2 at held at different temperatures for 2 days
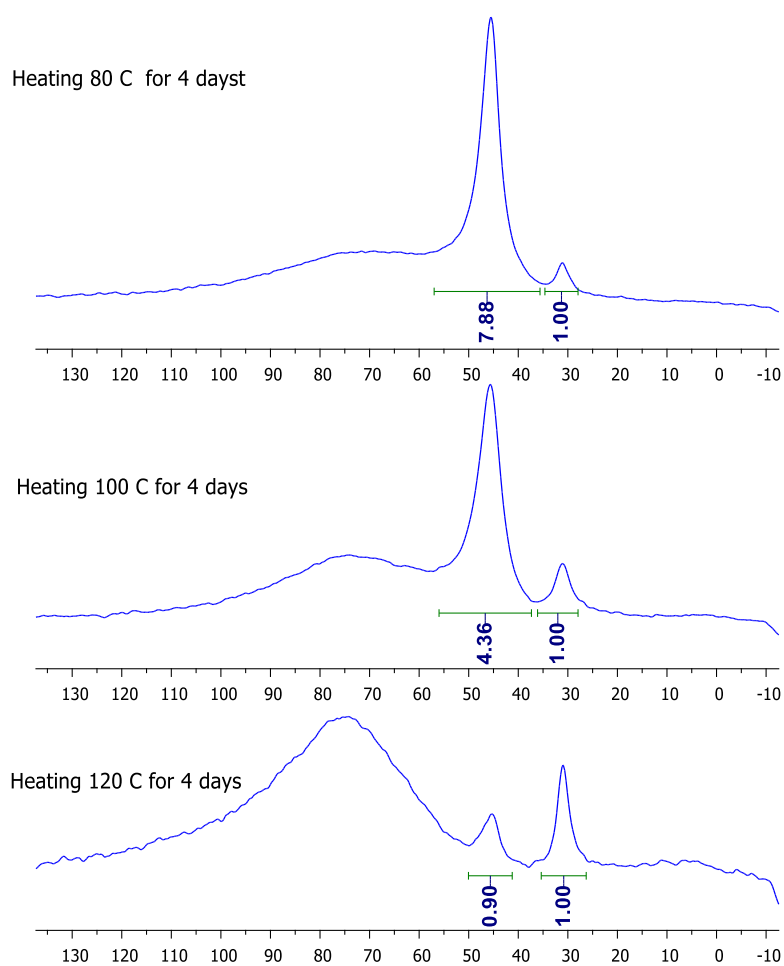
**Figure 6-4.** $^{25}$Al NMR: Mg[Al(hPhip)$_4$]$_2$ in G2 at held at different temperatures for 4 days
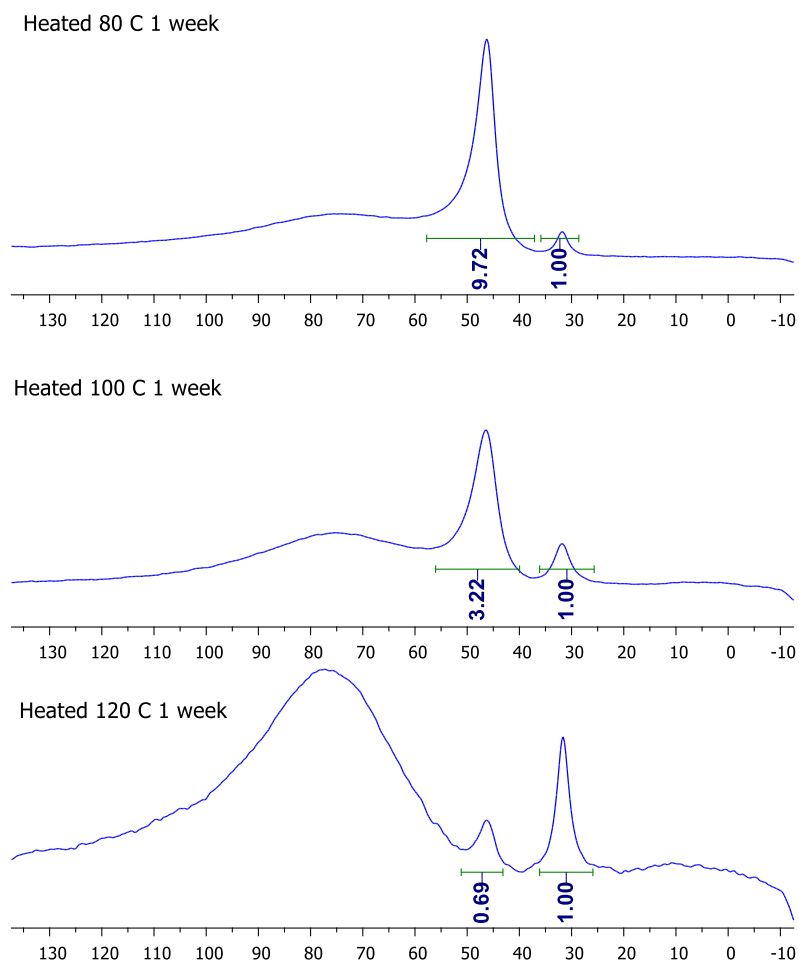
**Figure 6-5.** $^{25}$Al NMR: Mg[Al(hPhip)$_4$]$_2$ in G2 at held at different temperatures for 1 week
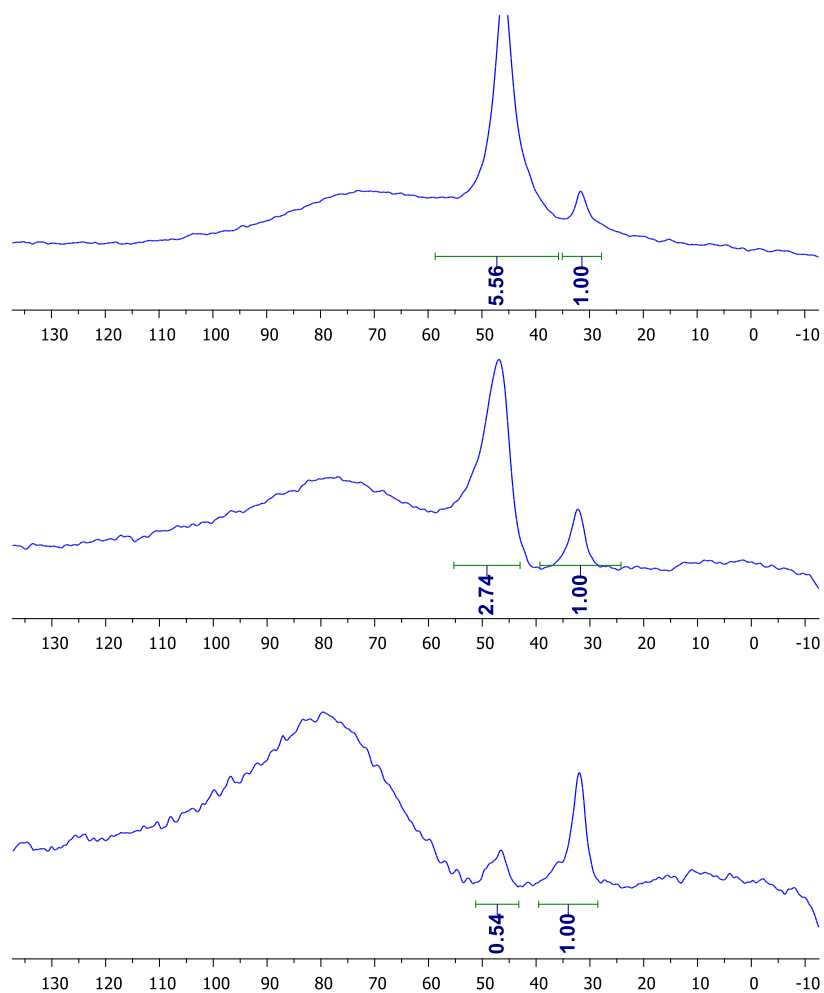
**Figure 6-6.** $^{25}$Al NMR: Mg[Al(hPhip)$_4$]$_2$ in G2 at held at different temperatures for 1 week, then cooled to room temperature for 1 week

## 6.5 Chapter 5: Mechanistic Insights in Quinone-Based Zinc Batteries with Nonaqueous Electrolytes

### 6.5.1 Materials preparations and characterizations.

All chemicals used in the synthesis were purchased from commercial suppliers in their highest pure form and used without further purification. 2,5-dimethoxy-1,4-benzoquinone (DMBQ) was purchased from TCI America and used without further purification. To make the slurry, DMBQ and carbon black were milled at 1:1 ratio for one hour using an 8000D Mixer/Mill machine from Spex SamplePrep company. The laminate slurry was then prepared by mixing 80 wt% of the above-milled DMBQ/carbon black powder, 10 wt% carbon black, and 10 wt% PVDF binder with NMP. The slurry was coated onto graphite foil, and the resulting laminates were dried in a 75 °C oven for two hours. The laminates were cut into electrodes with a diameter of 7/16 inches. The electrode laminates were dried in vacuum at 80 °C for more than 12 hours before use. Each laminate contains around 1 mg of active DMBQ material. The PAQS and 14PAQ electrode laminates were made in the same fashion. Whatman glass fiber filters were cut with the 5/8 inch punch and dried at 150 °C under vacuum in the glovebox before use. The polymeric materials PAQS and 14PAQ were synthesized according to the previously reported methods.[223,243]

The NMR spectra were recorded on a 300 MHz Bruker Avance spectrometer at ambient temperature (282.2 MHz for ^{19}F). The *Ex-situ* X-ray diffraction measurement (XRD) measurement was carried out using a MiniFlex 600 diffractometer using Cu ka radiation (Rigaku). Scanning electron microscopy (SEM) images were obtained using a Hitachi S4700 II scanning electron microscope with a field emission electron source. Energy-dispersive X-ray spectroscopy (EDX) was performed using Bruker Quantax. The

samples were very briefly exposed to air before insertion into the analysis chamber. Cyclic voltammetry (CV) was measured with a three-electrode configuration. The working electrode was a 2 mm platinum disk electrode purchased from CH instruments. The counter and reference electrodes were zinc rods purchased from ESPI metal and were polished with sandpaper before use.

### 6.5.2  Cell assembling and characterizations.

The 2032-coin cells were assembled with the electrode laminate described above as the cathode, the freshly polished Zinc foil (0.25 mm thickness) as the anode, a few drops of the electrolyte solutions, and Whatman glass fiber filter as the separator. The cycling performance was carried out using Maccor series 4000 cycler at room temperature with the discharge-charge cutoffs at 0 V and 1.2 V for the DMBQ-Zn, PAQS-Zn, and 14PAQ-Zn cells using 0.5M $Zn(TFSI)_2$ in MeCN, 0.5 M $Zn(TFSI)_2$ in G2, 0.5 M $Zn(PF_6)_2$ in MeCN, and 0.5 M $Zn(TFSI)_2/ZnCl_2$ in MeCN solutions as the electrolyte.

### 6.5.3  DFT calculations.

The molecular geometries were generated from scratch and then experienced two-stage optimization. First, the initial coordinates were optimized with the universal force field[244] using the Avogadro program.[245] Then, the structures were further optimized at the DFT level with the B3LYP/6-311G** method using the Gaussian program.[246] The energies of the highest occupied molecular orbital (HOMO) and lowest unoccupied molecular orbital (LUMO) were obtained from the optimized geometry. The molecular orbitals were visualized using the VMD software.[247]

## 6.6 Crystal structure and refinement data.

### 6.6.1 Crystal data and structure refinement for ($^{tBu}$POCOP)NiWCp(CO)$_3$

| Empirical formula | C$_{30}$H$_{44}$NiO$_5$P$_2$W | |
|---|---|---|
| Formula weight | 789.15 | |
| Temperature | 200(2) K | |
| Wavelength | 0.71073 Å | |
| Crystal system | Triclinic | |
| Space group | P -1 | |
| Unit cell dimensions | a = 8.0617 (8) Å | α = 103.562 (3) |
| | b = 11.4269 (11) Å | β = 95.996 (3) |
| | c = 18.1147 (15) Å | γ = 94.204 (3) |
| Volume | 1605.0 (3) Å$^3$ | |
| Z | 2 | |
| Density (calculated) | 1.633 Mg/m$^3$ | |
| Absorption coefficient | 4.302 mm$^{-1}$ | |
| F (000) | 792.0 | |
| Crystal size | 0.6 x 0.5 x 0.2 mm$^3$ | |
| Theta range for data collection | 1.17 to 27.10° | |
| Index ranges | -10<=h<=10, -14<=k<=14, -22<=l<=22 | |
| Reflections collected | 35657 | |
| Independent reflections | 6986 | |
| Completeness to theta = 27.10° | 98.4% | |
| Absorption correction | multi-scan | |
| Refinement method | Full-matrix least-squares on F2 | |
| Data / restraints / parameters | 6986 / 0 / 364 | |
| Goodness-of-fit on F$^2$ | 0.796 | |
| Final R indices [I>2sigma(I)] | R1 = 0.0380, wR2 = 0.1170 | |
| R indices (all data) | R1 = 0.0529, wR2 = 0.0958 | |
| Largest diff. peak and hole | 1.537 and -0.810 e.Å-3 | |

## 6.6.2  Crystal data and structure refinement for (IPr)CuCpFe(CO)(PEt₃) (1b)

| | |
|---|---|
| Empirical formula | $C_{171}H_{248}Cu4Fe4N_8O4P4$ |
| Formula weight | 3081.20 |
| Temperature | 100(2) K |
| Wavelength | 0.71073 Å |
| Crystal system | Triclinic |
| Space group | P -1 |
| Unit cell dimensions | a = 13.4331(14) Å  α = 106.434(2) |
| | b = 16.1161(17) Å  β = 105.217(2) |
| | c = 21.156(2) Å  γ = 95.793(2) |
| Volume | 4162.3(8) Å³ |
| Z | 1 |
| Density (calculated) | 1.229 Mg/m³ |
| Absorption coefficient | 0.930 mm⁻¹ |
| F (000) | 1692 |
| Crystal size | 0.5 x 0.5 x 0.5 mm³ |
| Theta range for data collection | 1.62 to 23.02° |
| Index ranges | -14<=h<=14, -17<=k<=17, -23<=l<=23 |
| Reflections collected | 77842 |
| Independent reflections | 7595 |
| Completeness to theta = 23.02° | 95.4% |
| Absorption correction | multi-scan |
| Refinement method | Full-matrix least-squares on F2 |
| Data / restraints / parameters | 11089 / 123 / 926 |
| Goodness-of-fit on $F^2$ | 1.004 |
| Final R indices [I>2sigma(I)] | R1 = 0.0529, wR2 = 0.0863 |
| R indices (all data) | R1 = 0.0985, wR2 = 0.0992 |
| Largest diff. peak and hole | 0.656 and – 0.514 e.Å-3 |

## 6.6.3 Crystal data and structure refinement for (IPr)CuCpFe(CO)(PPh$_2$Me) (1d)

| | | |
|---|---|---|
| Empirical formula | C$_{46}$H$_{54}$CuFeN$_2$OP | |
| Formula weight | 801.27 | |
| Temperature | 100(2) K | |
| Wavelength | 0.71073 Å | |
| Crystal system | Triclinic | |
| Space group | P -1 | |
| Unit cell dimensions | a = 10.485(4) Å | α = 73.890(7) |
| | b = 11.740(4) Å | β = 83.872(8) |
| | c = 17.380(6) Å | γ = 81.678(9) |
| Volume | 2028.7(12) Å$^3$ | |
| Z | 2 | |
| Density (calculated) | 1.312 Mg/m$^3$ | |
| Absorption coefficient | 0.958 mm$^{-1}$ | |
| F (000) | 844 | |
| Crystal size | 0.4 x 0.2 x 0.1 mm$^3$ | |
| Theta range for data collection | 1.82 to 25.68° | |
| Index ranges | -12<=h<=12, -14<=k<=14, -21<=l<=21 | |
| Reflections collected | 16775 | |
| Independent reflections | 7578 | |
| Completeness to theta = 25.68° | 98.3% | |
| Absorption correction | multi-scan | |
| Refinement method | Full-matrix least-squares on F2 | |
| Data / restraints / parameters | 7578 / 873 / 510 | |
| Goodness-of-fit on F$^2$ | 1.214 | |
| Final R indices [I>2sigma(I)] | R1 = 0.1460, wR2 = 0.2816 | |
| R indices (all data) | R1 = 0.3411, wR2 = 0.3335 | |
| Largest diff. peak and hole | 1.308 and - 0.717 e.Å-3 | |

### 6.6.4 Crystal data and structure refinement for (IPr)Cu($\mu$-H)$_2$FeCp(PPh$_3$) (2)

| | |
|---|---|
| Empirical formula | C$_{50}$H$_{58}$CuFeN$_2$P |
| Formula weight | 853.34 |
| Temperature | 100(2) K |
| Wavelength | 0.71073 Å |
| Crystal system | Orthorhombic |
| Space group | Pna2$_1$ |
| Unit cell dimensions | a = 15.7720(19) Å    $\alpha$ = 90 |
| | b = 14.4369(18) Å    $\beta$ = 90 |
| | c = 19.239(2) Å    $\gamma$ = 90 |
| Volume | 4380.7(9) Å$^3$ |
| Z | 4 |
| Density (calculated) | 1.294 Mg/m$^3$ |
| Absorption coefficient | 0.891 mm$^{-1}$ |
| F (000) | 1800 |
| Crystal size | 0.5 x 0.3 x 0.1 mm$^3$ |
| Theta range for data collection | 2.12 to 24.56° |
| Index ranges | -18<=h<=18, -13<=k<=14, -21<=l<=17 |
| Reflections collected | 41617 |
| Independent reflections | 5038 |
| Completeness to theta = 24.56° | 76.0% |
| Absorption correction | multi-scan |
| Refinement method | Full-matrix least-squares on F2 |
| Data / restraints / parameters | 5038 /26 / 511 |
| Goodness-of-fit on F$^2$ | 1.085 |
| Final R indices [I>2sigma(I)] | R1 = 0.0550, wR2 = 0.0766 |
| R indices (all data) | R1 = 0.0932, wR2 = 0.0860 |
| Largest diff. peak and hole | 0.332 and - 0.322e.Å-3 |

## 6.6.5 Crystal data and structure refinement for (IPr)CuWCp*(CO)$_2$(PMe$_2$Ph) (3b)

| | |
|---|---|
| Empirical formula | C$_{55}$H$_{82}$CuN$_2$O$_{1.5}$P$_2$W |
| Formula weight | 1104.55 |
| Temperature | 100(2) K |
| Wavelength | 0.71073 Å |
| Crystal system | Monoclinic |
| Space group | C12/c |
| Unit cell dimensions | a = 44.624(8) Å    α = 90 |
| | b = 14.338(3) Å    β = 107.920(5) |
| | c = 16.622(3) Å    γ = 90 |
| Volume | 10119.(3) Å$^3$ |
| Z | 8 |
| Density (calculated) | 1.450 Mg/m$^3$ |
| Absorption coefficient | 2.796 mm$^{-1}$ |
| F (000) | 4568 |
| Crystal size | 0.5 x 0.5 x 0.3 mm$^3$ |
| Theta range for data collection | 1.88 to 26.37° |
| Index ranges | -55<=h<=55, -17<=k<=17, -19<=l<=19 |
| Reflections collected | 9952 |
| Independent reflections | 9639 |
| Completeness to theta = 26.37° | 96.1% |
| Absorption correction | multi-scan |
| Refinement method | Full-matrix least-squares on F2 |
| Data / restraints / parameters | 9952 /0 / 502 |
| Goodness-of-fit on F$^2$ | 0.750 |
| Final R indices [I>2sigma(I)] | R1 = 0.0135, wR2 = 0.0766 |
| R indices (all data) | R1 = 0.0138, wR2 = 0.0772 |
| Largest diff. peak and hole | 0.914 and - 0.335e.Å-3 |

### 6.6.6  Crystal data and structure refinement for (IPr)CuWCp*(CO)$_2$(PMePh$_2$) (3c)

| | |
|---|---|
| Empirical formula | C$_{106.5}$H$_{129}$Cu2N4O$_4$P$_2$W2 |
| Formula weight | 2085.85 |
| Temperature | 100(2) K |
| Wavelength | 0.71073 Å |
| Crystal system | Monoclinic |
| Space group | P1 21/n 1 |
| Unit cell dimensions | a = 19.101(3) Å — α = 90 |
| | b = 12.915(2) Å — β = 101.580(4) |
| | c = 42.512(2) Å — γ = 90 |
| Volume | 10274(3) Å$^3$ |
| Z | 4 |
| Density (calculated) | 1.349 Mg/m$^3$ |
| Absorption coefficient | 2.721 mm$^{-1}$ |
| F (000) | 4256 |
| Crystal size | 0.4 x 0.3 x 0.1 mm$^3$ |
| Theta range for data collection | 1.65 to 23.53° |
| Index ranges | -21<=h<=21, -14<=k<=14, -47<=l<=47 |
| Reflections collected | 14800 |
| Independent reflections | 11286 |
| Completeness to theta = 23.53° | 97.0% |
| Absorption correction | multi-scan |
| Refinement method | Full-matrix least-squares on F2 |
| Data / restraints / parameters | 14800 /1820 /1091 |
| Goodness-of-fit on F$^2$ | 1.348 |
| Final R indices [I>2sigma(I)] | R1 = 0.0760, wR2 = 0.1849 |
| R indices (all data) | R1 = 0.1074, wR2 = 0.1945 |
| Largest diff. peak and hole | 3.674 and -3.933e.Å-3 |

### 6.6.7 Crystal data and structure refinement for (6Pr)CuWCp*(CO)₂(PEt₃) (3d)

| Empirical formula | $C_{46}H_{70}CuN_2O_2PW$ | |
|---|---|---|
| Formula weight | 961.40 | |
| Temperature | 100(2) K | |
| Wavelength | 0.71073 Å | |
| Crystal system | Monoclinic | |
| Space group | P1 21/n 1 | |
| Unit cell dimensions | a = 14.014(2) Å | α = 90 |
| | b = 15.018(2) Å | β = 102.854(4) |
| | c = 22.037(3) Å | γ = 90 |
| Volume | 4521.7(12) Å³ | |
| Z | 4 | |
| Density (calculated) | 1.412 Mg/m³ | |
| Absorption coefficient | 3.085 mm⁻¹ | |
| F (000) | 1976 | |
| Crystal size | 0.5 x 0.5 x 0.35 mm³ | |
| Theta range for data collection | 1.90 to 29.57° | |
| Index ranges | -18<=h<=19, -20<=k<=20, -30<=l<=30 | |
| Reflections collected | 230383 | |
| Independent reflections | 12491 | |
| Completeness to theta = 29.57° | 98.4% | |
| Absorption correction | multi-scan | |
| Refinement method | Full-matrix least-squares on F2 | |
| Data / restraints / parameters | 12491/151 /557 | |
| Goodness-of-fit on F² | 1.663 | |
| Final R indices [I>2sigma(I)] | R1 = 0.0561, wR2 = 0.1969 | |
| R indices (all data) | R1 = 0.0661, wR2 = 0.2011 | |
| Largest diff. peak and hole | 2.815 and -4.876 e.Å-3 | |

### 6.6.8 Crystal data and structure refinement for Mg(hPhip)$_2$(DME)$_2$ (1)

| | | |
|---|---|---|
| Empirical formula | C$_{26}$H$_{30}$F$_{12}$MgO$_6$ | |
| Formula weight | 690.81 | |
| Temperature | 100(2) K | |
| Wavelength | 0.71073 Å | |
| Crystal system | orthorhombic | |
| Space group | P 21 21 21 | |
| Unit cell dimensions | a = 12.5238(11) Å | α = 90 |
| | b = 13.2358(12) Å | β = 90 |
| | c = 17.5681(15) Å | γ = 90 |
| Volume | 2912.1(4) Å$^3$ | |
| Z | 4 | |
| Density (calculated) | 1.576 Mg/m$^3$ | |
| Absorption coefficient | 0.178 mm$^{-1}$ | |
| F (000) | 1416.0 | |
| Crystal size | 0.400 x 0.210 x 0.150 mm$^3$ | |
| Theta range for data collection | 2.24 to 30.55° | |
| Index ranges | -17<=h<=15, -18<=k<=17, -25<=l<=24 | |
| Reflections collected | 46667 | |
| Independent reflections | 7203 | |
| Completeness to theta = 30.55° | 99.7% | |
| Absorption correction | multi-scan | |
| Refinement method | Full-matrix least-squares on F2 | |
| Data / restraints / parameters | 8874 / 0 / 411 | |
| Goodness-of-fit on F$^2$ | 1.523 | |
| Final R indices [I>2sigma(I)] | R1 = 0.0423, wR2 = 0.0524 | |
| R indices (all data) | R1 = 0.0613, wR2 = 0.0546 | |
| Largest diff. peak and hole | 0.294 and – 0.277 e.Å-3 | |

### 6.6.9 Crystal data and structure refinement for Al(hPhip)₃(THF) (2)

| | |
|---|---|
| Empirical formula | $C_{37}H_{29}AlF_{18}O_4$ |
| Formula weight | 906.58 |
| Temperature | 100(2) K |
| Wavelength | 0.71073 Å |
| Crystal system | monoclinic |
| Space group | P 1 21/n 1 |
| Unit cell dimensions | a = 12.066(4) Å   α = 90 |
| | b = 15.828(5) Å   β = 93.544(9) |
| | c = 20.008(6) Å   γ = 90 |
| Volume | 3814.(2) Å³ |
| Z | 4 |
| Density (calculated) | 1.579 Mg/m³ |
| Absorption coefficient | 0.181 mm⁻¹ |
| F (000) | 1832 |
| Crystal size | 0.3 x 0.1 x 0.1 mm³ |
| Theta range for data collection | 2.31 to 28.70° |
| Index ranges | -16<=h<=16, -21<=k<=21, -27<=l<=24 |
| Reflections collected | 82321 |
| Independent reflections | 5185 |
| Completeness to theta = 28.70° | 99.7% |
| Absorption correction | multi-scan |
| Refinement method | Full-matrix least-squares on F2 |
| Data / restraints / parameters | 9837 / 0 / 541 |
| Goodness-of-fit on F² | 1.015 |
| Final R indices [I>2sigma(I)] | R1 = 0.0543, wR2 = 0.1328 |
| R indices (all data) | R1 = 0.1334, wR2 = 0.1737 |
| Largest diff. peak and hole | 0.685 and – 0.398 e.Å-3 |

## 7 References

(1)     paraffin | Origin and meaning of paraffin by Online Etymology Dictionary https://www.etymonline.com/word/paraffin (accessed Apr 16, 2020).

(2)     Buchanan, Robert, A. History of technology - Electricity | Britannica https://www.britannica.com/technology/history-of-technology/Electricity#ref10451 (accessed Apr 18, 2020).

(3)     Labinger, J. A.; Bercaw, J. E. Understanding and Exploiting C-H Bond Activation. *Nature*. Nature Publishing Group May 30, 2002, pp 507–514.

(4)     King, A. O.; Yasuda, N. Palladium-Catalyzed Cross-Coupling Reactions in the Synthesis of Pharmaceuticals; Springer, Berlin, Heidelberg, 2017; pp 205–245.

(5)     Torborg, C.; Beller, M. Recent Applications of Palladium-Catalyzed Coupling Reactions in the Pharmaceutical, Agrochemical, and Fine Chemical Industries. *Adv. Synth. &amp; Catal.* **2009**, *351*, 3027–3043.

(6)     *Organometallics in Process Chemistry*; Topics in Organometallic Chemistry; Springer Berlin Heidelberg: Berlin, Heidelberg, 2004; Vol. 6.

(7)     Hooshmand, S. E.; Heidari, B.; Sedghi, R.; Varma, R. S. Recent Advances in the Suzuki-Miyaura Cross-Coupling Reaction Using Efficient Catalysts in Eco-Friendly Media. *Green Chemistry*. Royal Society of Chemistry February 4, 2019, pp 381–405.

(8)     Biffis, A.; Centomo, P.; Del Zotto, A.; Zecca, M. Pd Metal Catalysts for Cross-Couplings and Related Reactions in the 21st Century: A Critical Review. *Chemical Reviews*. American Chemical Society February 28, 2018, pp 2249–2295.

(9)     Forero-Cortés, P. A.; Haydl, A. M. The 25th Anniversary of the Buchwald-Hartwig Amination: Development, Applications, and Outlook. *Organic Process Research and Development*. American Chemical Society August 16, 2019, pp 1478–1483.

(10)   Bucur, C. B.; Gregory, T.; Oliver, A. G.; Muldoon, J. Confession of a Magnesium Battery. *J. Phys. Chem. Lett.* **2015**, *6*, 3578–3591.

(11)   Egorova, K. S.; Ananikov, V. P. Which Metals Are Green for Catalysis? Comparison of the Toxicities of Ni, Cu, Fe, Pd, Pt, Rh, and Au Salts. *Angewandte Chemie - International Edition*. Wiley-VCH Verlag 2016, pp 12150–12162.

(12)   Jacks, T. E.; Belmont, D. T.; Briggs, C. A.; Horne, N. M.; Kanter, G. D.; Karrick, G. L.; Krikke, J. J.; McCabe, R. J.; Mustakis, J. G.; Nanninga, T. N.; Risedorph, G. S.; Seamans, R. E.; Skeean, R.; Winkle, D. D.; Zennie, T. M. Development of a Scalable Process for CI-1034, an Endothelin Antagonist. *Org. Process Res. Dev.* **2004**, *8*, 201–212.

(13)   Shaabani, A.; Hooshmand, S. E. Diversity-Oriented Catalyst-Free Synthesis of Pseudopeptides Containing Rhodanine Scaffolds via a One-Pot Sequential Isocyanide-Based Six-Component Reactions in Water Using Ultrasound Irradiation. *Ultrason. Sonochem.* **2018**, *40*, 84–90.

(14)   Sancheti, S. V.; Gogate, P. R. Intensification of Heterogeneously Catalyzed Suzuki-Miyaura Cross-Coupling Reaction Using Ultrasound: Understanding Effect of Operating Parameters. *Ultrason. Sonochem.* **2018**, *40*, 30–39.

(15)   Tasker, S. Z.; Standley, E. A.; Jamison, T. F. Recent Advances in Homogeneous Nickel Catalysis. *Nature*. Nature Publishing Group 2014, pp 299–309.

(16)   Mesganaw, T.; Garg, N. K. Ni- and Fe-Catalyzed Cross-Coupling Reactions of

Phenol Derivatives. *Organic Process Research and Development*. January 18, 2013, pp 29–39.

(17) Rosen, B. M.; Quasdorf, K. W.; Wilson, D. A.; Zhang, N.; Resmerita, A. M.; Garg, N. K.; Percec, V. Nickel-Catalyzed Cross-Couplings Involving Carbon-Oxygen Bonds. *Chemical Reviews*. March 9, 2011, pp 1346–1416.

(18) Shterenberg, I.; Salama, M.; Yoo, H. D.; Gofer, Y.; Park, J.-B.; Sun, Y.-K.; Aurbach, D. Evaluation of (CF 3 SO 2 ) 2 N − (TFSI) Based Electrolyte Solutions for Mg Batteries . *J. Electrochem. Soc.* **2015**, *162*, A7118–A7128.

(19) Olsen, B. A.; Sreedhara, A.; Baertschi, S. W. Impurity Investigations by Phases of Drug and Product Development. *TrAC - Trends in Analytical Chemistry*. Elsevier B.V. April 1, 2018, pp 17–23.

(20) Egorova, K. S.; Ananikov, V. P. Toxicity of Metal Compounds: Knowledge and Myths. *Organometallics* **2017**, *36*, 4071–4090.

(21) Hosseini, M. J.; Jafarian, I.; Farahani, S.; Khodadadi, R.; Tagavi, S. H.; Naserzadeh, P.; Mohammadi-Bardbori, A.; Arghavanifard, N. New Mechanistic Approach of Inorganic Palladium Toxicity: Impairment in Mitochondrial Electron Transfer. *Metallomics* **2016**, *8*, 252–259.

(22) Gildner, P. G.; Colacot, T. J. Reactions of the 21st Century: Two Decades of Innovative Catalyst Design for Palladium-Catalyzed Cross-Couplings. *Organometallics*. American Chemical Society October 16, 2015, pp 5497–5508.

(23) Mankad, N. Non-Precious Metal Catalysts for C–H Borylation Enabled by Metal–Metal Cooperativity. *Synlett* **2014**, *25*, 1197–1201.

(24) Mankad, N. P. Diverse Bimetallic Mechanisms Emerging from Transition Metal Lewis Acid/Base Pairs: Development of Co-Catalysis with Metal Carbenes and Metal Carbonyl Anions. *Chem. Commun.* **2018**, *54*, 1291–1302.

(25) Jupp, A. R.; Stephan, D. W. New Directions for Frustrated Lewis Pair Chemistry. *Trends in Chemistry*. Cell Press April 1, 2019, pp 35–48.

(26) Haneline, M. R.; Heyduk, A. F. C-C Bond-Forming Reductive Elimination from a Zirconium(IV) Redox-Active Ligand Complex. *J. Am. Chem. Soc.* **2006**, *128*, 8410–8411.

(27) Mankad, N. P. Selectivity Effects in Bimetallic Catalysis. *Chem. - A Eur. J.* **2016**, *22*, 5822–5829.

(28) Welch, G. C.; Juan, R. R. S.; Masuda, J. D.; Stephan, D. W. Reversible, Metal-Free Hydrogen Activation. *Science (80-. ).* **2006**, *314*, 1124–1126.

(29) Liu, L. L.; Cao, L. L.; Shao, Y.; Stephan, D. W. Single Electron Delivery to Lewis Pairs: An Avenue to Anions by Small Molecule Activation. *J. Am. Chem. Soc.* **2017**, *139*, 10062–10071.

(30) Liu, L. (Leo); Cao, L. L.; Shao, Y.; Ménard, G.; Stephan, D. W. A Radical Mechanism for Frustrated Lewis Pair Reactivity. *Chem* **2017**, *3*, 259–267.

(31) Sylvester, K. T.; Chirik, P. J. Iron-Catalyzed, Hydrogen-Mediated Reductive Cyclization of 1,6-Enynes and Diynes: Evidence for Bis(Imino)Pyridine Ligand Participation. *J. Am. Chem. Soc.* **2009**, *131*, 8772–8774.

(32) Obligacion, J. V.; Semproni, S. P.; Pappas, I.; Chirik, P. J. Cobalt-Catalyzed C(Sp2)-H Borylation: Mechanistic Insights Inspire Catalyst Design. *J. Am. Chem. Soc.* **2016**, *138*, 10645–10653.

(33) de Bruin, B.; Gualco, P.; Paul, N. D. Redox Non-Innocent Ligands. In *Ligand*

*Design in Metal Chemistry*; John Wiley & Sons, Ltd: Chichester, UK, 2016; pp 176–204.

(34) Luca, O. R.; Crabtree, R. H. Redox-Active Ligands in Catalysis. *Chemical Society Reviews*. Royal Society of Chemistry February 21, 2013, pp 1440–1459.

(35) Stradiotto, M.; Lundgren, R. J. *Ligand Design in Metal Chemistry: Reactivity and Catalysis*; wiley, 2016.

(36) Arevalo, R.; Chirik, P. J. Enabling Two-Electron Pathways with Iron and Cobalt: From Ligand Design to Catalytic Applications. *J. Am. Chem. Soc.* **2019**, *141*, 9106–9123.

(37) Joannou, M. V.; Hoyt, J. M.; Chirik, P. J. Investigations into the Mechanism of Inter- and Intramolecular Iron-Catalyzed [2 + 2] Cycloaddition of Alkenes. *J. Am. Chem. Soc.* **2020**, *142*, 5314–5330.

(38) Bouwkamp, M. W.; Bowman, A. C.; Lobkovsky, E.; Chirik, P. J. Iron-Catalyzed [2π + 2π] Cycloaddition of α,ω-Dienes: The Importance of Redox-Active Supporting Ligands. *J. Am. Chem. Soc.* **2006**, *128*, 13340–13341.

(39) Incarvito, C.; Rheingold, A. L.; Gavrilova, A. L.; Qin, C. J.; Bosnich, B. Bimetallic Reactivity. One-Site Addition Two-Metal Oxidation Reactions Using a Di-Co(II) Complex of a Binucleating Ligand with 5- and 6-Coordinate Sites. *Inorg. Chem.* **2001**, *40*, 4101–4108.

(40) Lewis, N. S.; Mann, K. R.; Gordon, J. G.; Gray, H. B. Oligomerization and Two-Center Oxidative Addition Reactions of a Dimeric Rhodium(I) Complex. *Journal of the American Chemical Society*. American Chemical Society October 1, 1976, pp 7461–7463.

(41) Chisholm, M. H. The ?2?4 Triple Bond between Molybdenum and Tungsten Atoms: Developing the Chemistry of an Inorganic Functional Group. *Angew. Chemie Int. Ed. English* **1986**, *25*, 21–30.

(42) Fackler, J. P.; Basil, J. D. Oxidative Addition of Methyl Iodide to a Dinuclear Gold(I) Complex. The X-Ray Crystal Structure of Bis[μ-(Dimethyldimethylenephosphoranyl-C,C)]-Iodomethyldigold(II)(Au-Au), Au2[(CH2)2P(CH3)2]2(CH3)I. *Organometallics* **1982**, *1*, 871–873.

(43) Powers, D. C.; Ritter, T. Bimetallic Redox Synergy in Oxidative Palladium Catalysis. *Acc. Chem. Res.* **2012**, *45*, 840–850.

(44) Wolf, W. J.; Winston, M. S.; Toste, F. D. Exceptionally Fast Carbon-Carbon Bond Reductive Elimination from Gold(III). *Nat. Chem.* **2014**, *6*, 159–164.

(45) Uyeda, C.; Steiman, T. J.; Pal, S. Catalytically Active Nickel-Nickel Bonds Using Redox-Active Ligands. *Synlett* **2016**, *27*, 814–820.

(46) Powers, I. G.; Kiattisewee, C.; Mullane, K. C.; Schelter, E. J.; Uyeda, C. A 1,2-Addition Pathway for C(Sp$^2$)−H Activation at a Dinickel Imide. *Chem. - A Eur. J.* **2017**, *23*, 7694–7697.

(47) Steiman, T. J.; Uyeda, C. Reversible Substrate Activation and Catalysis at an Intact Metal-Metal Bond Using a Redox-Active Supporting Ligand. *J. Am. Chem. Soc.* **2015**, *137*, 6104–6110.

(48) Schmidt, J. A. R.; Lobkovsky, E. B.; Coates, G. W. Chromium(III) Octaethylporphyrinato Tetracarbonylcobaltate: A Highly Active, Selective, and Versatile Catalyst for Epoxide Carbonylation. *J. Am. Chem. Soc.* **2005**, *127*, 11426–11435.

(49)  Tsutsumi, H.; Sunada, Y.; Shiota, Y.; Yoshizawa, K.; Nagashima, H. Nickel(II), Palladium(II), and Platinum(II) H3-Allyl Complexes Bearing a Bidentate Titanium(IV) Phosphinoamide Ligand: A Ti←M2 Dative Bond Enhances the Electrophilieity of the π-Allyl. *Organometallics* **2009**, *28*, 1988–1991.

(50)  Walker, W. K.; Kay, B. M.; Michaelis, S. A.; Anderson, D. L.; Smith, S. J.; Ess, D. H.; Michaelis, D. J. Origin of Fast Catalysis in Allylic Amination Reactions Catalyzed by Pd-Ti Heterobimetallic Complexes. *J. Am. Chem. Soc.* **2015**, *137*, 7371–7378.

(51)  Ye, J.; Cammarota, R. C.; Xie, J.; Vollmer, M. V.; Truhlar, D. G.; Cramer, C. J.; Lu, C. C.; Gagliardi, L. Rationalizing the Reactivity of Bimetallic Molecular Catalysts for CO2 Hydrogenation. *ACS Catal.* **2018**, *8*, 4955–4968.

(52)  Banerjee, S.; Karunananda, M. K.; Bagherzadeh, S.; Jayarathne, U.; Parmelee, S. R.; Waldhart, G. W.; Mankad, N. P. Synthesis and Characterization of Heterobimetallic Complexes with Direct Cu–M Bonds (M = Cr, Mn, Co, Mo, Ru, W) Supported by *N*-Heterocyclic Carbene Ligands: A Toolkit for Catalytic Reaction Discovery. *Inorg. Chem.* **2014**, *53*, 11307–11315.

(53)  Stephan, D. W. The Broadening Reach of Frustrated Lewis Pair Chemistry. *Science (80-. ).* **2016**, *354*.

(54)  Jordan, A. J.; Lalic, G.; Sadighi, J. P. Coinage Metal Hydrides: Synthesis, Characterization, and Reactivity. *Chemical Reviews*. American Chemical Society August 10, 2016, pp 8318–8372.

(55)  Karunananda, M. K.; Mankad, N. P. E-Selective Semi-Hydrogenation of Alkynes by Heterobimetallic Catalysis. *J. Am. Chem. Soc.* **2015**, *137*, 14598–14601.

(56)  Karunananda, M. K.; Mankad, N. P. Cooperative Strategies for Catalytic Hydrogenation of Unsaturated Hydrocarbons. *ACS Catal.* **2017**, *7*, 6110–6119.

(57)  Mazzacano, T. J.; Mankad, N. P. Base Metal Catalysts for Photochemical C-H Borylation That Utilize Metal-Metal Cooperativity. *J. Am. Chem. Soc.* **2013**, *135*, 17258–17261.

(58)  Waltz, K. M.; Muhoro, C. N.; Hartwig, J. F. C−H Activation and Functionalization of Unsaturated Hydrocarbons by Transition-Metal Boryl Complexes. *Organometallics* **1999**, *18*, 3383–3393.

(59)  Waltz, K. M. Selective Functionalization of Alkanes by Transition-Metal Boryl Complexes. *Science (80-. ).* **1997**, *277*, 211–213.

(60)  Waltz, K. M.; Hartwig, J. F. Functionalization of Alkanes by Isolated Transition Metal Boryl Complexes. *J. Am. Chem. Soc.* **2000**, *122*, 11358–11369.

(61)  Muldoon, J.; Bucur, C. B.; Gregory, T. Fervent Hype behind Magnesium Batteries: An Open Call to Synthetic Chemists—Electrolytes and Cathodes Needed. *Angewandte Chemie - International Edition*. Wiley-VCH Verlag 2017, pp 12064–12084.

(62)  Where the Energy Goes: Electric Cars https://www.fueleconomy.gov/feg/atv-ev.shtml (accessed Apr 30, 2020).

(63)  Denholm, P.; O'connell, M.; Brinkman, G.; Jorgenson, J. *Overgeneration from Solar Energy in California: A Field Guide to the Duck Chart*; 2013.

(64)  Thackeray, M. M.; Wolverton, C.; Isaacs, E. D. Electrical Energy Storage for Transportation - Approaching the Limits of, and Going beyond, Lithium-Ion Batteries. *Energy and Environmental Science*. Royal Society of Chemistry June

20, 2012, pp 7854–7863.

(65) Ponrouch, A.; Bitenc, J.; Dominko, R.; Lindahl, N.; Johansson, P.; Palacin, M. R. Multivalent Rechargeable Batteries. *Energy Storage Materials*. Elsevier B.V. July 1, 2019, pp 253–262.

(66) Riddlestone, I. M.; Kraft, A.; Schaefer, J.; Krossing, I. Taming the Cationic Beast: Novel Developments in the Synthesis and Application of Weakly Coordinating Anions. *Angewandte Chemie - International Edition*. Wiley-VCH Verlag October 22, 2018, pp 13982–14024.

(67) El Kharbachi, A.; Zavorotynska, O.; Latroche, M.; Cuevas, F.; Yartys, V.; Fichtner, M. Exploits, Advances and Challenges Benefiting beyond Li-Ion Battery Technologies. *J. Alloys Compd.* **2020**, *817*.

(68) Smidt, S. P.; Zimmermann, N.; Studer, M.; Pfaltz, A. Enantioselective Hydrogenation of Alkenes with Iridium–PHOX Catalysts: A Kinetic Study of Anion Effects. *Chem. - A Eur. J.* **2004**, *10*, 4685–4693.

(69) Xue, L.; Padgett, C. W.; DesMarteau, D. D.; Pennington, W. T. Synthesis and Structures of Alkali Metal Salts of Bis[(Trifluoromethyl)Sulfonyl]Imide. *Solid State Sci.* **2002**, *4*, 1535–1545.

(70) Krossing, I.; Raabe, I. Noncoordinating Anions - Fact or Fiction? A Survey of Likely Candidates. *Angewandte Chemie - International Edition*. April 13, 2004, pp 2066–2090.

(71) Chen, E. Y. X.; Lancaster, S. J. Weakly Coordinating Anions: Highly Fluorinated Borates. In *Comprehensive Inorganic Chemistry II (Second Edition): From Elements to Applications*; Elsevier Ltd, 2013; Vol. 1, pp 707–754.

(72) Van Den Broeke, J.; Deelman, B. J.; Van Koten, G. Tetrakis{3,5-Bis(Perfluorohexyl)Phenyl}borate: A Highly Fluorous Anion. *Tetrahedron Lett.* **2001**, *42*, 8085–8087.

(73) Reed, C. A. Carboranes: A New Class of Weakly Coordinating Anions for Strong Electrophiles, Oxidants, and Superacids. *Acc. Chem. Res.* **1998**, *31*, 133–139.

(74) Fisher, S. P.; Tomich, A. W.; Lovera, S. O.; Kleinsasser, J. F.; Guo, J.; Asay, M. J.; Nelson, H. M.; Lavallo, V. Nonclassical Applications of Closo-Carborane Anions: From Main Group Chemistry and Catalysis to Energy Storage. *Chemical Reviews*. American Chemical Society July 24, 2019, pp 8262–8290.

(75) Kirlikovali, K. O.; Axtell, J. C.; Anderson, K.; Djurovich, P. I.; Rheingold, A. L.; Spokoyny, A. M. Fine-Tuning Electronic Properties of Luminescent Pt(II) Complexes via Vertex-Differentiated Coordination of Sterically Invariant Carborane-Based Ligands. *Organometallics* **2018**, *37*, 3122–3131.

(76) Barth, R. F.; Mi, P.; Yang, W. Boron Delivery Agents for Neutron Capture Therapy of Cancer. *Cancer Commun.* **2018**, *38*, 1–15.

(77) Jung, D.; Raffan-Montoya, F.; Ramachandran, R.; Zhang, Y.; Islamoglu, T.; Marin, G.; Qian, E. A.; Dziedzic, R. M.; Farha, O. K.; Stoliarov, S. I.; Spokoyny, A. M. Cross-Linked Porous Polyurethane Materials Featuring Dodecaborate Clusters as Inorganic Polyol Equivalents. *Chem. Commun.* **2019**, *55*, 8852–8855.

(78) Martin, T. P. Compound Clusters. *Zeitschrift für Phys. D Atoms, Mol. Clust.* **1986**, *3*, 211–217.

(79) Köchner, T.; Engesser, T. A.; Scherer, H.; Plattner, D. A.; Steffani, A.; Krossing, I. [P9]+[Al(ORF)4]−, the Salt of a Homopolyatomic Phosphorus Cation. *Angew.*

*Chemie Int. Ed.* **2012**, *51*, 6529–6531.

(80)  Lau, K.-C.; Seguin, T. J.; Carino, E. V.; Hahn, N. T.; Connell, J. G.; Ingram, B. J.; Persson, K. A.; Zavadil, K. R.; Liao, C. Widening Electrochemical Window of Mg Salt by Weakly Coordinating Perfluoroalkoxyaluminate Anion for Mg Battery Electrolyte. *J. Electrochem. Soc.* **2019**, *166*, A1510–A1519.

(81)  Herb, J. T.; Nist-Lund, C.; Schwartz, J.; Arnoldb, C. B. Structural Effects of Magnesium Dialkoxides as Precursors for Magnesium-Ion Electrolytes. *ECS Electrochem. Lett.* **2015**, *4*, A49–A52.

(82)  Nist-Lund, C. A.; Herb, J. T.; Arnold, C. B. Improving Halide-Containing Magnesium-Ion Electrolyte Performance via Sterically Hindered Alkoxide Ligands. *J. Power Sources* **2017**, *362*, 308–314.

(83)  Herb, J. T.; Nist-Lund, C. A.; Arnold, C. B. A Fluorinated Alkoxyaluminate Electrolyte for Magnesium-Ion Batteries. *ACS Energy Lett.* **2016**, *1*, 1227–1232.

(84)  Zhao-Karger, Z.; Fichtner, M. Beyond Intercalation Chemistry for Rechargeable Mg Batteries: A Short Review and Perspective. *Frontiers in Chemistry*. Frontiers Media S.A. January 1, 2019.

(85)  Jing, Y.; Liang, Y.; Gheytani, S.; Yao, Y. A Quinone Anode for Lithium-Ion Batteries in Mild Aqueous Electrolytes. *ChemSusChem* **2020**, cssc.202000094.

(86)  Pan, B.; Zhou, D.; Huang, J.; Zhang, L.; Burrell, A. K.; Vaughey, J. T.; Zhang, Z.; Liao, C. 2,5-Dimethoxy-1,4-Benzoquinone (DMBQ) as Organic Cathode for Rechargeable Magnesium-Ion Batteries. *J. Electrochem. Soc.* **2016**, *163*, A580–A583.

(87)  Senoh, H.; Sakaebe, H.; Sano, H.; Yao, M.; Kuratani, K.; Takeichi, N.; Kiyobayashi, T. Sulfone-Based Electrolyte Solutions for Rechargeable Magnesium Batteries Using 2,5-Dimethoxy-1,4-Benzoquinone Positive Electrode. *J. Electrochem. Soc.* **2014**, *161*, A1315–A1320.

(88)  Schon, T. B.; McAllister, B. T.; Li, P. F.; Seferos, D. S. The Rise of Organic Electrode Materials for Energy Storage. *Chemical Society Reviews*. Royal Society of Chemistry November 21, 2016, pp 6345–6404.

(89)  Mankad, N. P. Diverse Bimetallic Mechanisms Emerging from Transition Metal Lewis Acid/Base Pairs: Development of Co-Catalysis with Metal Carbenes and Metal Carbonyl Anions. *Chem Commun* **2018**, *34*, 5497.

(90)  Busacca, C. A.; Fandrick, D. R.; Song, J. J.; Senanayake, C. H. The Growing Impact of Catalysis in the Pharmaceutical Industry. *Adv. Synth. Catal.* **2011**, *353*, 1825–1864.

(91)  Campos, K. R.; Coleman, P. J.; Alvarez, J. C.; Dreher, S. D.; Garbaccio, R. M.; Terrett, N. K.; Tillyer, R. D.; Truppo, M. D.; Parmee, E. R. The Importance of Synthetic Chemistry in the Pharmaceutical Industry. *Science (80-. ).* **2019**, *363*, eaat0805.

(92)  Hayler, J. D.; Leahy, D. K.; Simmons, E. M. A Pharmaceutical Industry Perspective on Sustainable Metal Catalysis. *Organometallics* **2018**, *38*, acs.organomet.8b00566.

(93)  Stephan, D. W.; Erker, G. Frustrated Lewis Pairs: Metal-Free Hydrogen Activation and More. *Angew. Chemie Int. Ed.* **2009**, *49*, 46–76.

(94)  Allen, A. E.; MacMillan, D. W. C. Synergistic Catalysis: A Powerful Synthetic Strategy for New Reaction Development. *Chem Sci* **2012**, *3*, 633.

(95)    Gade, L. H. Highly Polar Metal–Metal Bonds in "Early–Late" Heterodimetallic Complexes. *Angew. Chemie-International Ed. English* **2000**, *39*, 2658–2678.

(96)    Baranger, A. M.; Bergman, R. G. Cooperative Reactivity in the Interactions of XH Bonds with a Zirconium-Iridium Bridging Imido Complex. *J. Am. Chem. …* **1994**, *116*, 3822–3835.

(97)    Casey, C. P.; Morris Bullock, R. Search for Heterobimetallic Dihydrides from the Reaction of H2 with Metal--Metal Bonds. *J. Mol. Catal.* **1982**, *14*, 283–292.

(98)    Cooper, B. G.; Napoline, J. W.; Thomas, C. M. Catalytic Applications of Early/Late Heterobimetallic Complexes. *Catal. Rev.* **2012**, *54*, 1–40.

(99)    Pinkes, J. R.; Steffey, B. D.; Vites, J. C.; Cutler, A. R. Carbon Dioxide Insertion into the Fe-Zr and Ru-Zr Bonds of the Heterobimetallic Complexes Cp (CO) 2M-Zr (Cl) Cp2: Direct Production of the μ-H1 (C): H2 (O, O&apos;)-CO2 Compounds Cp (CO) 2M-CO2-Zr (Cl) Cp2. *Organometallics* **1994**, *13*, 21–23.

(100)   Stephan, D. W. Early-Late Heterobimetallics. *Coord. Chem. Rev.* **1989**, *95*, 41–107.

(101)   Chapman, A. M.; Haddow, M. F.; Wass, D. F. Frustrated Lewis Pairs beyond the Main Group: Synthesis, Reactivity, and Small Molecule Activation with Cationic Zirconocene–Phosphinoaryloxide Complexes. *J. Am. Chem. Soc.* **2011**, *133*, 18463–18478.

(102)   Bauer, J.; Braunschweig, H.; Dewhurst, R. D. Metal-Only Lewis Pairs with Transition Metal Lewis Bases. *Chem. Rev.* **2012**, *112*, 4329–4346.

(103)   Pannell, K. H.; Sharma, H. K. (Cyclopentadienyl)Dicarbonylmethyliron ((η 5-C 5H 5)Fe(CO) 2CH 3, FpMe), a Seminal Transition-Metal Alkyl Complex: Mobility of the Methyl Group †. *Organometallics* **2010**, *29*, 4741–4745.

(104)   THEYS, R.; DUDLEY, M.; HOSSAIN, M. Recent Chemistry of the H5-Cyclopentadienyl Dicarbonyl Iron Anion. *Coord. Chem. Rev.* **2009**, *253*, 180–234.

(105)   Whitesides, G. M.; Boschetto, D. J. Reaction of Threo-Dicarbonyl-. Pi.-Cyclopentadienyl (3, 3-Dimethylbutyl-1, 2-D2) Iron with Triphenylphosphine. *J. Am. Chem. Soc.* **1969**, *91*, 4313–4314.

(106)   Díez-González, S.; Nolan, S. N-Heterocyclic Carbene-Copper(I) Complexes in Homogeneous Catalysis. *Synlett* **2007**, *2007*, 2158–2167.

(107)   Jayarathne, U.; Mazzacano, T. J.; Bagherzadeh, S.; Mankad, N. P. Heterobimetallic Complexes with Polar, Unsupported Cu–Fe and Zn–Fe Bonds Stabilized by N-Heterocyclic Carbenes. *Organometallics* **2013**, *32*, 3986–3992.

(108)   Mazzacano, T. J.; Mankad, N. P. Base Metal Catalysts for Photochemical C–H Borylation That Utilize Metal–Metal Cooperativity. *J. Am. Chem. Soc.* **2013**, *135*, 17258–17261.

(109)   King, R. B. Applications of Metal Carbonyl Anions in the Synthesis of Ususual Organometallic Compounds. *Acc. Chem. Res.* **1970**, *3*, 417–427.

(110)   Morris, R. H. Brønsted–Lowry Acid Strength of Metal Hydride and Dihydrogen Complexes. *Chem. Rev.* **2016**, *116*, 8588–8654.

(111)   Jayarathne, U.; Parmelee, S. R.; Mankad, N. P. Small Molecule Activation Chemistry of Cu–Fe Heterobimetallic Complexes Toward CS 2and N 2O. *Inorg. Chem.* **2014**, *53*, 7730–7737.

(112)   Mixed phosphine/carbonyl derivatives of heterobimetallic copper–iron and copper–tungsten catalysts - ScienceDirect

https://www.sciencedirect.com/science/article/pii/S0277538718306156 (accessed Apr 23, 2020).

(113) Parmelee, S. R.; Mazzacano, T. J.; Zhu, Y.; Mankad, N. P.; Keith, J. A. A Heterobimetallic Mechanism for C–H Borylation Elucidated from Experimental and Computational Data. *ACS Catal.* **2015**, 3689–3699.

(114) Waltz, K. M.; He, X.; Muhoro, C.; Hartwig, J. F. Hydrocarbon Functionalization by Transition Metal Boryls. *J. Am. Chem. Soc.* **1995**, *117*, 11357–11358.

(115) Wang, Y.; Xie, Y.; Abraham, M. Y.; Wei, P.; Schaefer, H. F.; Schleyer, P. v. R.; Robinson, G. H. A Viable Anionic N-Heterocyclic Dicarbene. *J. Am. Chem. Soc.* **2010**, *132*, 14370–14372.

(116) Chen, H.; Hartwig, J. F. Catalytic, Regiospecific End-Functionalization of Alkanes: Rhenium-Catalyzed Borylation under Photochemical Conditions. *Angew. Chemie Int. Ed.* **1999**, *38*, 3391–3393.

(117) Iverson, C. N.; Smith, M. R. Stoichiometric and Catalytic B−C Bond Formation from Unactivated Hydrocarbons and Boranes. *J. Am. Chem. Soc.* **1999**, *121*, 7696–7697.

(118) Cho, J.-Y.; Iverson, C. N.; Smith, M. R. Steric and Chelate Directing Effects in Aromatic Borylation. *J. Am. Chem. Soc.* **2000**, *122*, 12868–12869.

(119) Chen, H.; Schlecht, S.; Semple, T. C.; Hartwig, J. F. Thermal, Catalytic, Regiospecific Functionalization of Alkanes. *Science (80-. ).* **2000**, *287*, 1995–1997.

(120) Mazzacano, T. J.; Mankad, N. P. Thermal C&#x2013;H Borylation Using a CO-Free Iron Boryl Complex. *Chem Commun* **2015**, *51*, 5379–5382.

(121) Karunananda, M. K.; Mankad, N. P. E-Selective Semi-Hydrogenation of Alkynes by Heterobimetallic Catalysis. *J. Am. Chem. Soc.* **2015**, *137*, 14598–14601.

(122) Karunananda, M. K.; Mankad, N. P. Heterobimetallic H 2Addition and Alkene/Alkane Elimination Reactions Related to the Mechanism of E-Selective Alkyne Semihydrogenation. *Organometallics* **2017**, *36*, 220–227.

(123) Mazzacano, T. J.; Leon, N. J.; Waldhart, G. W.; Mankad, N. P. Fundamental Organometallic Chemistry under Bimetallic Influence: Driving β-Hydride Elimination and Diverting Migratory Insertion at Cu and Ni. *Dalt. Trans.* **2017**, *46*, 5518–5521.

(124) Cheng, L. J.; Mankad, N. P. Heterobimetallic Control of Regioselectivity in Alkyne Hydrostannylation: Divergent Syntheses of α-A Nd (E)-β-Vinylstannanes via Cooperative Sn-H Bond Activation. *J. Am. Chem. Soc.* **2019**, *141*, 3710–3716.

(125) Zhang, Y.; Karunananda, M. K.; Yu, H.-C.; Clark, K. J.; Williams, W.; Mankad, N. P.; Ess, D. H. Dynamically Bifurcating Hydride Transfer Mechanism and Origin of Inverse Isotope Effect for Heterodinuclear AgRu-Catalyzed Alkyne Semihydrogenation. *ACS Catal.* **2019**, *9*, 2657–2663.

(126) Karunananda, M. K.; Parmelee, S. R.; Waldhart, G. W.; Mankad, N. P. Experimental and Computational Characterization of the Transition State for C–X Bimetallic Oxidative Addition at a Cu–Fe Reaction Center. *Organometallics* **2015**, *34*, 150721134336002–150721134336008.

(127) Mazzacano, T. J.; Leon, N. J.; Waldhart, G. W.; Mankad, N. P. Fundamental Organometallic Chemistry under Bimetallic Influence: Driving β-Hydride Elimination and Diverting Migratory Insertion at Cu and Ni. *Dalt. Trans.* **2017**, *46*,

5518–5521.

(128) Schmeier, T. J.; Nova, A.; Hazari, N.; Maseras, F. Synthesis of PCP-Supported Nickel Complexes and Their Reactivity with Carbon Dioxide. *Chem. - A Eur. J.* **2012**, *18*, 6915–6927.

(129) Hao, J.; Vabre, B.; Mougang-Soumé, B.; Zargarian, D. Small Molecule Activation by POC Sp 3OP-Nickel Complexes. *Chem. - A Eur. J.* **2014**, *20*, 12544–12552.

(130) Venkanna, G. T.; Tammineni, S.; Arman, H. D.; Tonzetich, Z. J. Synthesis, Characterization, and Catalytic Activity of Nickel(II) Alkyl Complexes Supported by Pyrrole-Diphosphine Ligands. *Organometallics* **2013**.

(131) Chierotti, M. R.; Rossin, A.; Gobetto, R.; Peruzzini, M. Interaction between a Transition-Metal Fluoride and a Transition-Metal Hydride: Water-Mediated Hydrofluoric Acid Evolution Following Fluoride Solvation. *Inorg. Chem.* **2013**, *52*, 12616–12623.

(132) Leon, N. J.; Yu, H. C.; Mazzacano, T. J.; Mankad, N. P. Pursuit of C-H Borylation Reactions with Non-Precious Heterobimetallic Catalysts: Hypothesis-Driven Variations on a Design Theme. *Synlett* **2020**, *31*, 125–132.

(133) Levina, V. A.; Rossin, A.; Belkova, N. V.; Chierotti, M. R.; Epstein, L. M.; Filippov, O. A.; Gobetto, R.; Gonsalvi, L.; Lledõs, A.; Shubina, E. S.; Zanobini, F.; Peruzzini, M. Acid-Base Interaction between Transition-Metal Hydrides: Dihydrogen Bonding and Dihydrogen Evolution. *Angew. Chemie - Int. Ed.* **2011**, *50*, 1367–1370.

(134) Parmelee, S. R.; Mazzacano, T. J.; Zhu, Y.; Mankad, N. P.; Keith, J. A. A Heterobimetallic Mechanism for C-h Borylation Elucidated from Experimental and Computational Data. *ACS Catal.* **2015**, *5*, 3689–3699.

(135) Bagherzadeh, S.; Mankad, N. P. Catalyst Control of Selectivity in CO 2Reduction Using a Tunable Heterobimetallic Effect. *J. Am. Chem. Soc.* **2015**, *137*, 10898–10901.

(136) Wilson, G. L. O.; Abraha, M.; Krause, J. A.; Guan, H. Reactions of Phenylacetylene with Nickel POCOP-Pincer Hydride Complexes Resulting in Different Outcomes from Their Palladium Analogues. *Dalt. Trans.* **2015**, *44*, 12128–12136.

(137) Pell, C. J.; Ozerov, O. V. Catalytic Dehydrogenative Borylation of Terminal Alkynes by POCOP-Supported Palladium Complexes. *Inorg. Chem. Front.* **2015**, *2*, 720–724.

(138) Press, L. P.; Kosanovich, A. J.; McCulloch, B. J.; Ozerov, O. V. High-Turnover Aromatic C–H Borylation Catalyzed by POCOP-Type Pincer Complexes of Iridium. *J. Am. Chem. Soc.* **2016**, *138*, 9487–9497.

(139) Jonasson, K. J.; Wendt, O. F. Synthesis and Characterization of a Family of POCOP Pincer Complexes with Nickel: Reactivity Towards CO 2 and Phenylacetylene. *Chem. - A Eur. J.* **2014**, *20*, 11894–11902.

(140) Xu, X.; Feng, H.; Huang, L.; Liu, X. Direct Amidation of Carboxylic Acids through an Active α-Acyl Enol Ester Intermediate. *J. Org. Chem.* **2018**, *83*, 7962–7969.

(141) Valeur, E.; Bradley, M. Amide Bond Formation: Beyond the Myth of Coupling Reagents. *Chemical Society Reviews*. 2009, pp 606–631.

(142) Dunetz, J. R.; Magano, J.; Weisenburger, G. A. Large-Scale Applications of Amide Coupling Reagents for the Synthesis of Pharmaceuticals. *Organic Process*

*Research and Development*. American Chemical Society February 19, 2016, pp 140–177.

(143) Chakraborty, S.; Zhang, J.; Krause, J. A.; Guan, H. An Efficient Nickel Catalyst for the Reduction of Carbon Dioxide with a Borane. *J. Am. Chem. Soc.* **2010**, *132*, 8872–8873.

(144) Mazzacano, T. J.; Mankad, N. P. Thermal C–H Borylation Using a CO-Free Iron Boryl Complex. *Chem. Commun.* **2015**, *51*, 5379–5382.

(145) Barnett, B. R.; Moore, C. E.; Rheingold, A. L.; Figueroa, J. S. Frustrated Lewis Pair Behavior of Monomeric (Boryl)Iminomethanes Accessed from Isocyanide 1,1-Hydroboration. *Chem. Commun.* **2015**, *51*, 541–544.

(146) Hartwig, J. F. Evolution of C-H Bond Functionalization from Methane to Methodology. *J. Am. Chem. Soc.* **2016**, *138*, 2–24.

(147) Davies, H. M. L.; Du Bois, J.; Yu, J.-Q. C–H Functionalization in Organic Synthesis. *Chem. Soc. Rev.* **2011**, *40*, 1855.

(148) Engle, K. M.; Mei, T.-S.; Wasa, M.; Yu, J.-Q. Weak Coordination as a Powerful Means for Developing Broadly Useful C–H Functionalization Reactions. *Acc. Chem. Res.* **2012**, *45*, 788–802.

(149) Gutekunst, W. R.; Baran, P. S. C–H Functionalization Logic in Total Synthesis. *Chem. Soc. Rev.* **2011**, *40*, 1976.

(150) Jones, W. D.; Feher, F. J. Comparative Reactivities of Hydrocarbon Carbon-Hydrogen Bonds with a Transition-Metal Complex. *Acc. Chem. Res.* **1989**, *22*, 91–100.

(151) Jones, W. D. HYDROCARBON CHEMISTRY:Enhanced: Conquering the Carbon-Hydrogen Bond. *Science (80-. ).* **2000**, *287*, 1942–1943.

(152) Mkhalid, I. A. I.; Barnard, J. H.; Marder, T. B.; Murphy, J. M.; Hartwig, J. F. C−H Activation for the Construction of C−B Bonds. *Chem. Rev.* **2010**, *110*, 890–931.

(153) Cho, J.-Y.; Tse, M. K.; Holmes, D.; Maleczka, R. E.; Smith, M. R. Remarkably Selective Iridium Catalysts for the Elaboration of Aromatic C-H Bonds. *Science (80-. ).* **2002**, *295*, 305–308.

(154) Hartwig, J. F. Borylation and Silylation of C–H Bonds: A Platform for Diverse C–H Bond Functionalizations. *Acc. Chem. Res.* **2012**, *45*, 864–873.

(155) Ohki, Y.; Hatanaka, T.; Tatsumi, K. C−H Bond Activation of Heteroarenes Mediated by a Half-Sandwich Iron Complex of N-Heterocyclic Carbene. *J. Am. Chem. Soc.* **2008**, *130*, 17174–17186.

(156) Hatanaka, T.; Ohki, Y.; Tatsumi, K. CH Bond Activation/Borylation of Furans and Thiophenes Catalyzed by a Half-Sandwich Iron N-Heterocyclic Carbene Complex. *Chem. - An Asian J.* **2010**, *5*, 1657–1666.

(157) Yoshigoe, Y.; Kuninobu, Y. Iron-Catalyzed *Ortho* -Selective C–H Borylation of 2-Phenylpyridines and Their Analogs. *Org. Lett.* **2017**, *19*, 3450–3453.

(158) Furukawa, T.; Tobisu, M.; Chatani, N. Nickel-Catalyzed Borylation of Arenes and Indoles via C-H Bond Cleavage. *Chem Commun* **2015**, *51*, 6508–6511.

(159) Obligacion, J. V; Semproni, S. P.; Chirik, P. J. Cobalt-Catalyzed C–H Borylation. *J. Am. Chem. Soc.* **2014**, *136*, 4133–4136.

(160) Obligacion, J. V; Semproni, S. P.; Pappas, I.; Chirik, P. J. Cobalt-Catalyzed C(Sp 2)-H Borylation: Mechanistic Insights Inspire Catalyst Design. *J. Am. Chem. Soc.* **2016**, *138*, 10645–10653.

(161) Obligacion, J. V.; Chirik, P. J. Mechanistic Studies of Cobalt-Catalyzed C(Sp$^2$)–H Borylation of Five-Membered Heteroarenes with Pinacolborane. *ACS Catal.* **2017**, *7*, 4366–4371.

(162) Jayasundara, C. R. K.; Sabasovs, D.; Staples, R. J.; Oppenheimer, J.; Smith, M. R.; Maleczka, R. E. Cobalt-Catalyzed C–H Borylation of Alkyl Arenes and Heteroarenes Including the First Selective Borylations of Secondary Benzylic C–H Bonds. *Organometallics* **2018**, *37*, 1567–1574.

(163) Obligacion, J. V.; Zhong, H.; Chirik, P. J. Insights into Activation of Cobalt Pre-Catalysts for C(*Sp*$^2$)−H Functionalization. *Isr. J. Chem.* **2017**, *57*, 1032–1036.

(164) Légaré, M.-A.; Courtemanche, M.-A.; Rochette, É.; Fontaine, F.-G. BORON CATALYSIS. Metal-Free Catalytic C-H Bond Activation and Borylation of Heteroarenes. *Science (80-. ).* **2015**, *349*, 513–516.

(165) Mazzacano, T. J. New Developments in Base Metal-Catalyzed C-H Borylation, University of Illinois at Chicago, 2017.

(166) Sawyer, K. R.; Cahoon, J. F.; Shanoski, J. E.; Glascoe, E. A.; Kling, M. F.; Schlegel, J. P.; Zoerb, M. C.; Hapke, M.; Hartwig, J. F.; Webster, C. E.; Harris, C. B. Time-Resolved IR Studies on the Mechanism for the Functionalization of Primary C−H Bonds by Photoactivated Cp*W(CO) 3(Bpin). *J. Am. Chem. Soc.* **2010**, *132*, 1848–1859.

(167) Cotton, F. A.; Daniels, L. M.; Murillo, C. A.; Zhou, H. C. The Effect of Divergent-Bite Ligands on Metal–Metal Bond Distances in Some Paddlewheel Complexes. *Inorganica Chim. Acta* **2000**, *300–302*, 319–327.

(168) Parmelee, S. R.; Mankad, N. P. A Data-Intensive Re-Evaluation of Semibridging Carbonyl Ligands. *Dalt. Trans.* **2015**, *44*, 17007–17014.

(169) Curtis, M. D.; Han, K. R.; Butler, W. M. Metal-Metal Multiple Bonds. 5. Molecular Structure and Fluxional Behavior of Tetraethylammonium μ-Cyano-Bis(Cyclopentadienyldicarbonylmolybdate)(Mo-Mo) and the Question of Semibridging Carbonyls. *Inorg. Chem.* **1980**, *19*, 2096–2101.

(170) Karunananda, M. K.; Vázquez, F. X.; Alp, E. E.; Bi, W.; Chattopadhyay, S.; Shibata, T.; Mankad, N. P. Experimental Determination of Redox Cooperativity and Electronic Structures in Catalytically Active Cu–Fe and Zn–Fe Heterobimetallic Complexes. *Dalt. Trans.* **2014**, *43*, 13661.

(171) Hicken, A.; White, A. J. P.; Crimmin, M. R. Preparation and Characterisation of Heterobimetallic Copper–Tungsten Hydride Complexes. *Dalt. Trans.* **2018**.

(172) Kubas, G. J. Dihydrogen Complexes as Prototypes for the Coordination Chemistry of Saturated Molecules. *Proc. Natl. Acad. Sci. U. S. A.* **2007**, *104*, 6901–6907.

(173) Azwana R. Sadique; Elizabeth A. Gregory; William W. Brennessel, and; Holland*, P. L. Mechanistic Insight into NN Cleavage by a Low-Coordinate Iron(II) Hydride Complex. **2007**.

(174) Morris, R. H. Estimating the Acidity of Transition Metal Hydride and Dihydrogen Complexes by Adding Ligand Acidity Constants. *J. Am. Chem. Soc.* **2014**, *136*, 1948–1959.

(175) Olivetti, E. A.; Ceder, G.; Gaustad, G. G.; Fu, X. Lithium-Ion Battery Supply Chain Considerations: Analysis of Potential Bottlenecks in Critical Metals. *Joule.* Cell Press October 11, 2017, pp 229–243.

(176) Electric cars have made the once obscure metal cobalt the hottest commodity of 2017 — Quartz https://qz.com/1159341/electric-cars-have-made-the-once-obscure-metal-cobalt-the-hottest-commodity-of-2017/ (accessed Apr 13, 2020).

(177) Banza Lubaba Nkulu, C.; Casas, L.; Haufroid, V.; De Putter, T.; Saenen, N. D.; Kayembe-Kitenge, T.; Musa Obadia, P.; Kyanika Wa Mukoma, D.; Lunda Ilunga, J. M.; Nawrot, T. S.; Luboya Numbi, O.; Smolders, E.; Nemery, B. Sustainability of Artisanal Mining of Cobalt in DR Congo. *Nat. Sustain.* **2018**, *1*, 495–504.

(178) Jäckle, M.; Groß, A. Microscopic Properties of Lithium, Sodium, and Magnesium Battery Anode Materials Related to Possible Dendrite Growth. *J. Chem. Phys.* **2014**, *141*, 174710.

(179) Gregory, T. D. Nonaqueous Electrochemistry of Magnesium. *J. Electrochem. Soc.* **1990**, *137*, 775.

(180) Aurbach, D.; Lu, Z.; Schechter, A.; Gofer, Y.; Gizbar, H.; Turgeman, R.; Cohen, Y.; Moshkovich, M.; Levi, E. Prototype Systems for Rechargeable Magnesium Batteries. *Nature* **2000**, *407*, 724–727.

(181) Fichtner, M. Chapter 1: Motivation for a Magnesium Battery. In *RSC Energy and Environment Series*; Royal Society of Chemistry, 2020; Vol. 2020-January, pp 1–16.

(182) Davidson, R.; Verma, A.; Santos, D.; Hao, F.; Fincher, C.; Xiang, S.; Buskirk, J. Van; Xie, K.; Pharr, M.; Mukherjee, P. P.; Banerjee, S. Formation of Magnesium Dendrites during Electrodeposition. *ACS Energy Lett.* **2019**, 375–376.

(183) Forero-Saboya, J. D.; Marchante, E.; Araujo, R. B.; Monti, D.; Johansson, P.; Ponrouch, A. Cation Solvation and Physicochemical Properties of Ca Battery Electrolytes. *J. Phys. Chem. C* **2019**, *123*, 29524–29532.

(184) Muldoon, J.; Bucur, C. B.; Oliver, A. G.; Sugimoto, T.; Matsui, M.; Kim, H. S.; Allred, G. D.; Zajicek, J.; Kotani, Y. Electrolyte Roadblocks to a Magnesium Rechargeable Battery. *Energy and Environmental Science*. The Royal Society of Chemistry March 1, 2012, pp 5941–5950.

(185) Lu, Z.; Schechter, A.; Moshkovich, M.; Aurbach, D. On the Electrochemical Behavior of Magnesium Electrodes in Polar Aprotic Electrolyte Solutions. *J. Electroanal. Chem.* **1999**, *466*, 203–217.

(186) Zhao-Karger, Z.; Fichtner, M. Beyond Intercalation Chemistry for Rechargeable Mg Batteries: A Short Review and Perspective. *Front. Chem.* **2019**, *6*.

(187) Dong, H.; Liang, Y.; Tutusaus, O.; Mohtadi, R.; Zhang, Y.; Hao, F.; Yao, Y. Directing Mg-Storage Chemistry in Organic Polymers toward High-Energy Mg Batteries. *Joule* **2019**, *3*, 782–793.

(188) He, S.; Luo, J.; Liu, T. L. MgCl2/AlCl3 Electrolytes for Reversible Mg Deposition/Stripping: Electrochemical Conditioning or Not? *J. Mater. Chem. A* **2017**, *5*, 12718–12722.

(189) Zhao-Karger, Z.; Gil Bardaji, M. E.; Fuhr, O.; Fichtner, M. A New Class of Non-Corrosive, Highly Efficient Electrolytes for Rechargeable Magnesium Batteries. *J. Mater. Chem. A* **2017**, *5*, 10815–10820.

(190) Zhao-Karger, Z.; Gil Bardaji, M. E.; Fuhr, O.; Fichtner, M. A New Class of Non-Corrosive, Highly Efficient Electrolytes for Rechargeable Magnesium Batteries. *J. Mater. Chem. A* **2017**, *5*, 10815–10820.

(191) Tutusaus, O.; Mohtadi, R.; Arthur, T. S.; Mizuno, F.; Nelson, E. G.; Sevryugina, Y.

V. An Efficient Halogen-Free Electrolyte for Use in Rechargeable Magnesium Batteries. *Angew. Chemie Int. Ed.* **2015**, *54*, 7900–7904.

(192) Hebié, S.; Alloin, F.; Iojoiu, C.; Berthelot, R.; Leprêtre, J.-C. Magnesium Anthracene System-Based Electrolyte as a Promoter of High Electrochemical Performance Rechargeable Magnesium Batteries. **2018**.

(193) Krossing, I.; Brands, H.; Feuerhake, R.; Koenig, S. New Reagents to Introduce Weakly Coordinating Anions of Type Al(ORF)4-: Synthesis, Structure and Characterization of Cs and Trityl Salts. In *Journal of Fluorine Chemistry*; Elsevier, 2001; Vol. 112, pp 83–90.

(194) Krossing, I.; Reisinger, A. Perfluorinated Alkoxyaluminate Salts of Cationic Brønsted Acids: Synthesis, Structure, and Characterization of [H(OEt2)2][Al{OC(CF3)3}4] and[H(THF)2][Al{OC(CF3)3}4]. *Eur. J. Inorg. Chem.* **2005**, *2005*, 1979–1989.

(195) Tanaka, D.; Kadonaga, Y.; Manabe, Y.; Fukase, K.; Sasaya, S.; Maruyama, H.; Nishimura, S.; Yanagihara, M.; Konishi, A.; Yasuda, M. Synthesis of Cage-Shaped Aluminum Aryloxides: Efficient Lewis Acid Catalyst for Stereoselective Glycosylation Driven by Flexible Shift of Four-to Five-Coordination. *J. Am. Chem. Soc.* **2019**, *141*, 17466–17471.

(196) Barile, C. J.; Barile, E. C.; Zavadil, K. R.; Nuzzo, R. G.; Gewirth, A. A. Electrolytic Conditioning of a Magnesium Aluminum Chloride Complex for Reversible Magnesium Deposition. *J. Phys. Chem. C* **2014**, *118*, 27623–27630.

(197) Han, S. D.; Rajput, N. N.; Qu, X.; Pan, B.; He, M.; Ferrandon, M. S.; Liao, C.; Persson, K. A.; Burrell, A. K. Origin of Electrochemical, Structural, and Transport Properties in Nonaqueous Zinc Electrolytes. *ACS Appl. Mater. Interfaces* **2016**, *8*, 3021–3031.

(198) Merrill, L. C.; Schaefer, J. L. The Influence of Interfacial Chemistry on Magnesium Electrodeposition in Non-Nucleophilic Electrolytes Using Sulfone-Ether Mixtures. *Front. Chem.* **2019**, *7*.

(199) Zheng, J.; Zhao, Q.; Tang, T.; Yin, J.; Quilty, C. D.; Renderos, G. D.; Liu, X.; Deng, Y.; Wang, L.; Bock, D. C.; Jaye, C.; Zhang, D.; Takeuchi, E. S.; Takeuchi, K. J.; Marschilok, A. C.; Archer, L. A. Reversible Epitaxial Electrodeposition of Metals in Battery Anodes. *Science (80-. ).* **2019**, *366*, 645–648.

(200) Liang, H.; Cao, Z.; Ming, F.; Zhang, W.; Anjum, D. H.; Cui, Y.; Cavallo, L.; Alshareef, H. N. Aqueous Zinc-Ion Storage in MoS 2 by Tuning the Intercalation Energy. *Nano Lett.* **2019**, *19*, 3199–3206.

(201) Bredland, A. M. Leclanché Electrolyte Compositional Studies for Thin Film Batteries. *J. Electrochem. Soc.* **1976**, *123*, 311.

(202) Lee, J. S.; Kim, S. T.; Cao, R.; Choi, N. S.; Liu, M.; Lee, K. T.; Cho, J. Metal-Air Batteries with High Energy Density: Li-Air versus Zn-Air. *Advanced Energy Materials*. January 1, 2011, pp 34–50.

(203) Xu, M.; Ivey, D. G.; Xie, Z.; Qu, W. Rechargeable Zn-Air Batteries: Progress in Electrolyte Development and Cell Configuration Advancement. *Journal of Power Sources*. Elsevier B.V. June 1, 2015, pp 358–371.

(204) Li, Y.; Lu, J. Metal-Air Batteries: Will They Be the Future Electrochemical Energy Storage Device of Choice? *ACS Energy Letters*. American Chemical Society June 9, 2017, pp 1370–1377.

(205) Kar, M.; Simons, T. J.; Forsyth, M.; MacFarlane, D. R. Ionic Liquid Electrolytes as a Platform for Rechargeable Metal-Air Batteries: A Perspective. *Phys. Chem. Chem. Phys.* **2014**, *16*, 18658–18674.

(206) Jung, K. N.; Hwang, S. M.; Park, M. S.; Kim, K. J.; Kim, J. G.; Dou, S. X.; Kim, J. H.; Lee, J. W. One-Dimensional Manganese-Cobalt Oxide Nanofibres as Bi-Functional Cathode Catalysts for Rechargeable Metal-Air Batteries. *Sci. Rep.* **2015**, *5*, 1–10.

(207) Liu, S.; Wang, M.; Qian, T.; Liu, J.; Yan, C. Selenium-Doped Carbon Nanosheets with Strong Electron Cloud Delocalization for Nondeposition of Metal Oxides on Air Cathode of Zinc-Air Battery. *ACS Appl. Mater. Interfaces* **2019**, *11*, 20056–20063.

(208) Liu, W.; Yin, R.; Shi, W.; Xu, X.; Shen, X.; Yin, Q.; Xu, L.; Cao, X. Gram-Scale Preparation of 2d Transition Metal Hydroxide/Oxide Assembled Structures for Oxygen Evolution and Zn-Air Battery. *ACS Appl. Energy Mater.* **2019**, *2*, 579–586.

(209) Tomon, C.; Sarawutanukul, S.; Duangdangchote, S.; Krittayavathananon, A.; Sawangphruk, M. Photoactive Zn-Air Batteries Using Spinel-Type Cobalt Oxide as a Bifunctional Photocatalyst at the Air Cathode. *Chem. Commun.* **2019**, *55*, 5855–5858.

(210) Chen, X.; Yan, Z.; Yu, M.; Sun, H.; Liu, F.; Zhang, Q.; Cheng, F.; Chen, J. Spinel Oxide Nanoparticles Embedded in Nitrogen-Doped Carbon Nanofibers as a Robust and Self-Standing Bifunctional Oxygen Cathode for Zn-Air Batteries. *J. Mater. Chem. A* **2019**, *7*, 24868–24876.

(211) Kundu, D.; Adams, B. D.; Duffort, V.; Vajargah, S. H.; Nazar, L. F. A High-Capacity and Long-Life Aqueous Rechargeable Zinc Battery Using a Metal Oxide Intercalation Cathode. *Nat. Energy* **2016**, *1*, 16119.

(212) Kundu, D.; Hosseini Vajargah, S.; Wan, L.; Adams, B.; Prendergast, D.; Nazar, L. F. Aqueous: Vs. Nonaqueous Zn-Ion Batteries: Consequences of the Desolvation Penalty at the Interface. *Energy Environ. Sci.* **2018**, *11*, 881–892.

(213) Yang, Y.; Tang, Y.; Liang, S.; Wu, Z.; Fang, G.; Cao, X.; Wang, C.; Lin, T.; Pan, A.; Zhou, J. Transition Metal Ion-Preintercalated V2O5 as High-Performance Aqueous Zinc-Ion Battery Cathode with Broad Temperature Adaptability. *Nano Energy* **2019**, *61*, 617–625.

(214) Liu, W.; Hao, J.; Xu, C.; Mou, J.; Dong, L.; Jiang, F.; Kang, Z.; Wu, J.; Jiang, B.; Kang, F. Investigation of Zinc Ion Storage of Transition Metal Oxides, Sulfides, and Borides in Zinc Ion Battery Systems. *Chem. Commun.* **2017**, *53*, 6872–6874.

(215) Zhao, J.; Ren, H.; Liang, Q.; Yuan, D.; Xi, S.; Wu, C.; Manalastas, W.; Ma, J.; Fang, W.; Zheng, Y.; Du, C. F.; Srinivasan, M.; Yan, Q. High-Performance Flexible Quasi-Solid-State Zinc-Ion Batteries with Layer-Expanded Vanadium Oxide Cathode and Zinc/Stainless Steel Mesh Composite Anode. *Nano Energy* **2019**, *62*, 94–102.

(216) Chen, Z.; Liu, T.; Zhao, Z.; Zhang, Z.; Han, X.; Han, P.; Li, J.; Wang, J.; Li, J.; Huang, S.; Zhou, X.; Zhao, J.; Cui, G. Fast Anion Intercalation into Graphite Cathode Enabling High-Rate Rechargeable Zinc Batteries. *J. Power Sources* **2020**, *457*, 227994.

(217) Heo, J. W.; Chae, M. S.; Hyoung, J.; Hong, S. T. Rhombohedral Potassium-Zinc Hexacyanoferrate as a Cathode Material for Nonaqueous Potassium-Ion

Batteries. *Inorg. Chem.* **2019**, *58*, 3065–3072.

(218) Cheng, Y.; Luo, L.; Zhong, L.; Chen, J.; Li, B.; Wang, W.; Mao, S. X.; Wang, C.; Sprenkle, V. L.; Li, G.; Liu, J. Highly Reversible Zinc-Ion Intercalation into Chevrel Phase Mo6S8 Nanocubes and Applications for Advanced Zinc-Ion Batteries. *ACS Appl. Mater. Interfaces* **2016**, *8*, 13673–13677.

(219) Li, C.; Zhang, X.; He, W.; Xu, G.; Sun, R. Cathode Materials for Rechargeable Zinc-Ion Batteries: From Synthesis to Mechanism and Applications. *Journal of Power Sources*. Elsevier B.V. February 15, 2020, p 227596.

(220) Pan, B.; Huang, J.; Feng, Z.; Zeng, L.; He, M.; Zhang, L.; Vaughey, J. T.; Bedzyk, M. J.; Fenter, P.; Zhang, Z.; Burrell, A. K.; Liao, C. Polyanthraquinone-Based Organic Cathode for High-Performance Rechargeable Magnesium-Ion Batteries. *Adv. Energy Mater.* **2016**, *6*, 1600140.

(221) Yang, M.; Liu, K.; Shkrob, I. A.; Liao, C. Redox-Active Polymers (Redoxmers) for Electrochemical Energy Storage. *MRS Communications*. Cambridge University Press 2019, pp 1151–1167.

(222) Lipson, A. L.; Proffit, D. L.; Pan, B.; Fister, T. T.; Liao, C.; Burrell, A. K.; Vaughey, J. T.; Ingram, B. J. Current Collector Corrosion in Ca-Ion Batteries. *J. Electrochem. Soc.* **2015**, *162*, A1574–A1578.

(223) Song, Z.; Zhan, H.; Zhou, Y. Anthraquinone Based Polymer as High Performance Cathode Material for Rechargeable Lithium Batteries. *Chem. Commun.* **2009**, No. 4, 448–450.

(224) Song, Z.; Qian, Y.; Gordin, M. L.; Tang, D.; Xu, T.; Otani, M.; Zhan, H.; Zhou, H.; Wang, D. Polyanthraquinone as a Reliable Organic Electrode for Stable and Fast Lithium Storage. *Angew. Chemie Int. Ed.* **2015**, *54*, 13947–13951.

(225) Xu, K. Nonaqueous Liquid Electrolytes for Lithium-Based Rechargeable Batteries. *Chem. Rev.* **2004**, *104*, 4303–4417.

(226) Krämer, E.; Schedlbauer, T.; Hoffmann, B.; Terborg, L.; Nowak, S.; Gores, H. J.; Passerini, S.; Winter, M. Mechanism of Anodic Dissolution of the Aluminum Current Collector in 1 M LiTFSI EC:DEC 3:7 in Rechargeable Lithium Batteries. *J. Electrochem. Soc.* **2013**, *160*, A356–A360.

(227) See, K. A.; Chapman, K. W.; Zhu, L.; Wiaderek, K. M.; Borkiewicz, O. J.; Barile, C. J.; Chupas, P. J.; Gewirth, A. A. The Interplay of Al and Mg Speciation in Advanced Mg Battery Electrolyte Solutions. *J. Am. Chem. Soc.* **2016**, *138*, 328–337.

(228) Sa, N.; Pan, B.; Saha-Shah, A.; Hubaud, A. A.; Vaughey, J. T.; Baker, L. A.; Liao, C.; Burrell, A. K. Role of Chloride for a Simple, Non-Grignard Mg Electrolyte in Ether-Based Solvents. *ACS Appl. Mater. Interfaces* **2016**, *8*, 16002–16008.

(229) Mizrahi, O.; Amir, N.; Pollak, E.; Chusid, O.; Marks, V.; Gottlieb, H.; Larush, L.; Zinigrad, E.; Aurbach, D. Electrolyte Solutions with a Wide Electrochemical Window for Rechargeable Magnesium Batteries. *J. Electrochem. Soc.* **2008**, *155*, A103.

(230) Pan, B.; Huang, J.; Sa, N.; Brombosz, S. M.; Vaughey, J. T.; Zhang, L.; Burrell, A. K.; Zhang, Z.; Liao, C. MgCl 2 : The Key Ingredient to Improve Chloride Containing Electrolytes for Rechargeable Magnesium-Ion Batteries . *J. Electrochem. Soc.* **2016**, *163*, A1672–A1677.

(231) Ta, K.; See, K. A.; Gewirth, A. A. Elucidating Zn and Mg Electrodeposition

Mechanisms in Nonaqueous Electrolytes for Next-Generation Metal Batteries. *J. Phys. Chem. C* **2018**, *122*, 13790–13796.

(232) Sheldrick, G. M. A Short History of SHELX. *Acta Crystallogr. Sect. A Found. Crystallogr.* **2008**, *64*, 112–122.

(233) Müller, P. Practical Suggestions for Better Crystal Structures. *Crystallogr. Rev.* **2009**, *15*, 57–83.

(234) Ein neuer weg zu polyisonitril-substituierten halbsandwhich-komplexen des zweiwertigen molybdäns und wolframs - ScienceDirect https://www.sciencedirect.com/science/article/abs/pii/0022328X89853653 (accessed May 1, 2020).

(235) Filippou, A. C.; Grünleitner, W. Ein Neuer Weg Zu Polyisonitril-Substituierten Halbsandwhich-Komplexen Des Zweiwertigen Molybdäns Und Wolframs. *J. Organomet. Chem.* **1989**, *378*, 387–399.

(236) Banerjee, S.; Karunananda, M. K.; Bagherzadeh, S.; Jayarathne, U.; Parmelee, S. R.; Waldhart, G. W.; Mankad, N. P. Synthesis and Characterization of Heterobimetallic Complexes with Direct Cu-M Bonds (M = Cr, Mn, Co, Mo, Ru, W) Supported by N-Heterocyclic Carbene Ligands: A Toolkit for Catalytic Reaction Discovery. *Inorg. Chem.* **2014**, *53*, 11307–11315.

(237) Mankad, N. P.; Laitar, D. S.; Sadighi, J. P. Synthesis, Structure, and Alkyne Reactivity of a Dimeric (Carbene)Copper(I) Hydride. *Organometallics* **2004**, *23*, 3369–3371.

(238) Chakraborty, S.; Krause, J. A.; Guan, H. Hydrosilylation of Aldehydes and Ketones Catalyzed by Nickel PCP-Pincer Hydride Complexes. *Organometallics* **2009**, *28*, 582–586.

(239) Gibson, D. H.; Owens, K.; Mandal, S. K.; Sattich, W. E.; Franco, J. O. Synthesis and Thermolysis of Neutral Metal Formyl Complexes of Molybdenum, Tungsten, Manganese, and Rhenium. *Organometallics* **1989**, *8*, 498–505.

(240) Jordan, A. J.; Wyss, C. M.; Bacsa, J.; Sadighi, J. P. Synthesis and Reactivity of New Copper(I) Hydride Dimers. *Organometallics* **2016**, *35*, 613–616.

(241) A. Brown, D.; Lyons, H. J.; Manning, A. R. A New Type of Isomerism in Some Phosphine and Phosphite Derivatives of the Metal Carbonyls. *Inorganica Chim. Acta* **1970**, *4*, 428–430.

(242) Alt, H. G.; Engelhardt, H. E.; Kläui, W.; Müller, A. Trimethylphosphan- Und Carbonyl-Hydrid-Halbsandwichkomplexe Des Chroms, Molybdäns Und Wolframs: C5Hf5−, C5Me5− Und Ein Isoelektronischer 6e−-Sauerstof-Tripodligand Im Vergleich. *J. Organomet. Chem.* **1987**, *331*, 317–327.

(243) Song, Z.; Qian, Y.; Gordin, M. L.; Tang, D.; Xu, T.; Otani, M.; Zhan, H.; Zhou, H.; Wang, D. Polyanthraquinone as a Reliable Organic Electrode for Stable and Fast Lithium Storage. *Angew. Chemie Int. Ed.* **2015**, *54*, 13947–13951.

(244) Rappé, A. K.; Casewit, C. J.; Colwell, K. S.; Goddard, W. A.; Skiff, W. M. UFF, a Full Periodic Table Force Field for Molecular Mechanics and Molecular Dynamics Simulations. *J. Am. Chem. Soc.* **1992**, *114*, 10024–10035.

(245) Hanwell, M. D.; Curtis, D. E.; Lonie, D. C.; Vandermeerschd, T.; Zurek, E.; Hutchison, G. R. Avogadro: An Advanced Semantic Chemical Editor, Visualization, and Analysis Platform. *J. Cheminform.* **2012**, *4*, 17.

(246) Frisch, M. J.; Trucks, G.; Schlegel, H.; Scuseria, G.; Robb, M.; Cheeseman, J.;

Scalmani, G.; Barone, V.; Mennucci, B.; Persson, G. Gaussian 09. Gaussian Inc.: Wallingford, CT 2009.

(247) Humphrey, W.; Dalke, A.; Schulten, K. VMD: Visual Molecular Dynamics. *J. Mol. Graph.* **1996**, *14*, 33–38.

# Noel J. Leon

**Education:**

Ph.D. Candidate, Department of Chemistry
University of Illinois at Chicago, Chicago, IL 2014-present
Faculty Advisor: Neal Mankad

BA in Chemistry, Weinberg College of Arts and Sciences
Northwestern University, Evanston, IL, 2013

**Work Experience:**

**Graduate Research Assistant ( Fall 2014 – Present)**

Synthesizing new earth-abundant (Fe, Cu, Ni, W) heterobimetallic complexes to study bond activation toward more sustainable transition metal catalysis

Developed a variety of new, earth-abundant bimetallic complexes using phosphines and isocyanides to study the activation of boranes, borylation of C-H bonds, and bimetallic $H_2$ elimination reactions

Applying synthetic organometallic skills toward manipulating Mg-alkoxyaluminate electrolytes for Mg-ion batteries.

**Publications**

Mazzacano, T. J.; Leon, N. J.; Waldhart, G. W.; Mankad, N. P. Fundamental Organometallic Chemistry under Bimetallic Influence: Driving β-Hydride Elimination and Diverting Migratory Insertion at Cu and Ni. *Dalt. Trans.* **2017**, *46*, 5518–5521

Leon, N. J.; Yu, H. C.; Mazzacano, T. J.; Mankad, N. P. Mixed Phosphine/Carbonyl Derivatives of Heterobimetallic Copper–Iron and Copper–Tungsten Catalysts. *Polyhedron.* **2019**, *157*, 116–123.

Leon, N. J.; Yu, H. C.; Mazzacano, T. J.; Mankad, N. P. Pursuit of C-H Borylation Reactions with Non-Precious Heterobimetallic Catalysts: Hypothesis-Driven Variations on a Design Theme. *Synlett.* **2020**, *31*, 125–132.

Yang, M.; Leon, N. J.; Pan, B.; Yu, Z.; Cheng, Lei; Liao, C. 5.      Mechanistic Insights in Quinone-Based Zinc Batteries with Nonaqueous Electrolytes. *J. Electrochem.* **2020**, *Submitted.*

*Leon, N. J.: Mankad, N. P.* Detection of a ligand redistribution process for hydrocarbon-soluble Mg{Al[OC(Ph)(CF$_3$)$_2$]$_4$}$_2$: evidence of a "hidden equilibrium" in polyfluorinated alkoxyaluminate chemistry. *Inorg. Chem.* **2020**, *Submitted*

**Presentations**

2017 UIC Chemistry Research Day (Symposium) – Poster presentation

2018 Next Generation Electrochemistry Program – Poster/PowerPoint presentations

**Activities**

Helped donate equipment from retired professors' labs to schools in Haiti, 2010

UIC Chemistry Demo Day – chemistry demonstrations for Chicagoland grade school children, 2017, 2018

NU HerStory – tours educating young Chicago schoolgirls about contributions from women in science, 2017

UIC Chemistry Graduate Association – Vice President – organized outreach, career resources, symposiums, and activities to promote department pride and comradery among graduate students, 2017, 2018

Helped organize UIC Chemistry's 1st/2nd annual research symposium

## 9   Copywrite permissions

Leon, N. J.; Yu, H. C.; Mazzacano, T. J.; Mankad, N. P. Pursuit of C-H Borylation Reactions with Non-Precious Heterobimetallic Catalysts: Hypothesis-Driven Variations on a Design Theme. *Synlett* **2020**, *31*, 125–132.

**Thieme**

Thieme Sharing Guide

> Thieme Sharing Guide (PDF, 578 KB)

## Article Sharing

> **DOI Link**   > **Accepted Manuscript**   > **Published Journal Article**

Thieme endorses the STM Voluntary article > sharing principles  to enable collaboration, professional relationships and advances in science and discovery. You can find detailed information, also on individual publishers' sharing policies and in different languages, on > www.howcanishareit.com.

We want you to share your research with colleagues and maximize its visibility and impact, at every stage of publication. The below guidelines will help you to understand how you can share your articles, depending on the article version you wish to re-use.

### DOI Link to the published article on Thieme-connect

One easy way to maximize the impact of your research is to share the DOI linking to your article on > Thieme-connect with your colleagues, friends, business contacts, and on your institutional profile page. You can also increase awareness posting the link on social media or professional and academic networking sites.

### Accepted Manuscript

You can share the peer-reviewed, accepted version of your article (Accepted Manuscript, AM) without any alterations or enhancements:

**Immediately**

- As part of a grant application or submission of thesis or doctorate
- In invitation-only research collaboration groups via sites entered into an agreement with Thieme.

**After an embargo period of 12 months**

- On Scholarly Collaboration Networks (SCNs) which have signed up to the STM Voluntary article sharing principles
- On not-for-profit hosting platforms such as your institutional repository, for example at your affiliated institution or non-commercial subject-based repositories, such as PMC, Europe PMC.

- For reproduction of material from PPS:
  [Original citation] - Reproduced by permission of The Royal Society of Chemistry (RSC) on behalf of the European Society for Photobiology, the European Photochemistry Association, and RSC

Leon, N. J.; Yu, H. C.; Mazzacano, T. J.; Mankad, N. P. Mixed Phosphine/Carbonyl Derivatives of Heterobimetallic Copper–Iron and Copper–Tungsten Catalysts. *Polyhedron* **2019**, *157*, 116–123.